Light Ion Beam Fusion Target Development Facility Studies: Progress Report for the Period October 1, 1984 to September 30, 1985

B. Badger, R.L. Engelstad, D.L. Henderson, G.L. Kulcinski, E.G. Lovell, G.A. Moses, R.R. Peterson, I.N. Sviatoslavsky, and J.J. Watrous

September 30, 1985

UWFDM-652

FUSION TECHNOLOGY INSTITUTE

UNIVERSITY OF WISCONSIN

MADISON WISCONSIN

Light Ion Beam Fusion Target Development Facility Studies: Progress Report for the Period October 1, 1984 to September 30, 1985

B. Badger, R.L. Engelstad, D.L. Henderson, G.L. Kulcinski, E.G. Lovell, G.A. Moses, R.R. Peterson, I.N. Sviatoslavsky, and J.J. Watrous

Fusion Technology Institute
University of Wisconsin
1500 Engineering Drive
Madison, WI 53706

http://fti.neep.wisc.edu

September 30, 1985

UWFDM-652

LIGHT ION BEAM FUSION TARGET DEVELOPMENT FACILITY STUDIES: PROGRESS REPORT FOR THE PERIOD OCTOBER 1, 1984 TO SEPTEMBER 30, 1985

B. Badger, R.L. Engelstad, D.L. Henderson,

G.L. Kulcinski, E.G. Lovell, G.A. Moses,

R.R. Peterson, I.N. Sviatoslavsky, J.J. Watrous

Fusion Technology Institute
1500 Johnson Drive
University of Wisconsin-Madison
Madison, Wisconsin 53706

September 30, 1985

UWFDM-652

TABLE OF CONTENTS

1. Introduction

1.1 Statement of Work and Summary of Results

During the period from October 1984 to September 1985 we have addressed three general technical areas associated with the design of the Light Ion Fusion Target Development Facility (TDF). These are: (1) mechanical design of the target chamber, (2) activation analysis of the target chamber and shield, and (3) plasma channel formation and ion propagation. The specific statement of work is given in Table 1.1. During this time we also completed two-dimensional hydrodynamic studies of nonspherical blast waves that were part of a previous contract. These results will be summarized in this annual report as well. The remainder of Chapter 1 introduces the results that follow and discusses the publications and graduating students that were supported as part of this research.

Chapter 2 is devoted to activation analysis of the fusion target and the target chamber and shield. Activation calculations were done for representative unclassified light ion beam target configurations. The activated condensable target materials were assumed to be deposited on the inner surface of the target chamber and were included in the dose calculations for the facility. Design studies were done to reduce the target chamber activation by introducing low activation material, graphite, into the target chamber to soften the neutron spectrum. This was motivated by the fact that most of the offending transmutations in the first wall were due to high energy neutrons. The energy thresholds for these reactions were in the range of 3-10 MeV. Thus a softening of the spectrum could reduce the number of these reactions.

A careful study of short-lived radioactive isotopes was made to determine their effect on the dose received immediately after shutdown of the facility.

Table 1.1. Statement of Work

Provide a calculational study for the Target Development Facility (TDF) as per the following specifications:

1. Work Related to the Design and Activation of a Target Development Facility (TDF) Reaction Chamber:

   a. Perform calculations of neutron fluxes, induced radioactivity, and biological hazards for a TDF reaction vessel which is surrounded by a borated water shield and is coated with a thermal neutron absorbing material (such as Boral or Borasil). These calculations should be performed for reaction vessels constructed of both aluminum and steel based alloys. Other concepts for reducing first wall radioactivity due to refluxing neutrons may also be considered.

   b. Develop alternatives to code-designed target chamber vessels that will have lower residual radioactivity properties. Such designs might include spherical vessels or first walls with larger strength-to-mass ratios (e.g., via corrugated walls or a jacketed design). Provide calculations of the residual radioactivity associated with such designs and estimates of the additional costs involved in their fabrication.

   c. Provide suggestions as to how maintenance might be carried out in the presence of the calculated radiological dose rates with the water shield in place and with the water removed.

   d. Provide calculations for low-cycle strain-based (as opposed to stress-based) fatigue of a 3 m radius aluminum alloy code-designed vessel under the influence of 300 MJ target yields.

   e. Investigate the coupling of the transmission line housings in the TDF to the wall of the target chamber vessel. Suggest possible designs that might be employed to allow flexure of the first wall without transmitting the shock loading to the pulsed power equipment.

   f. Analyze the impact of the results of tasks 1.a-e on the choice of a TDF target chamber design.

2. Theoretical Support for Plasma Channel Work:

   a. Utilize the University of Wisconsin computer code "ZPINCH" to provide time-dependent, one-dimensional computational simulations of the behavior of laser-induced plasma channels in the presence of a magnetically insulated beam port.

Table 1.1 (continued)

b. Provide estimates of the plasma channel circuit parameters that take into account the effects of MHD and kinetic stability limits, beam ion energy losses, plasma radiation, and channel overlap.

c. Perform a preliminary examination of the time-dependent (MHD time scale) motion of plasma channels due to mutual fields near the point of overlap. Provide a description of a quasistatic multichannel configuration for the TDF.

d. Analyze the impact of the results of tasks 2a-c on the design of the TDF channel formation equipment.

This was important to determine the validity of our steady state neutronics approximation to a pulsed source of neutrons.

An estimate was made for the production of radioisotopes in the water shield. The most important isotope was N-16 with a 7 second half-life. Work continues on the evaluation of N-16 as an occupational problem.

Using the dose rates computed from these studies, maintenance schedules that satisfy federal exposure regulations were devised.

Chapter 3 is devoted to the mechanical design aspects of the TDF. A computer program to estimate low-cycle strain-based fatigue lifetime was written to evaluate both aluminum and steel. Alternative designs of the pressure vessel in the form of spherical shells were investigated to determine the increase in strength that one could achieve by using such an idealized structure. Stress levels in this spherical structure are considerably less than the more conventional cylindrical vessel under consideration as the primary design. Coupling of the transmission lines to the target chamber using a bellows component was investigated. There appears to be no coupling problem for the range of wall deflections computed for the TDF.

Chapter 4 covers the work done on plasma channel design. A set of three computer programs, ZPINCH, WINDOW, and ION have been used to evaluate channel formation, ion propagation stability, and ion propagation efficiency. Estimates of stable transport regimes have been made for ion beam parameters relevant to TDF. Channel formation in nitrogen gas using realistic external circuit parameters has been investigated for four meter long channels. Channel inductance for long channels limits the current rise time to values that significantly change our concept of the ideal plasma channel. Work continues on this problem.Simple estimates have been made for the effect of B_z fields on

the channel dynamics. Such fields might be used to insulate the ion beam from the wall of the target chamber.

Chapter 5 reports on the results of two-dimensional radiation hydrodynamics calculations of microfireball propagation in stratified gas atmospheres. This arrangement is proposed to reduce the shock overpressure on diodes placed near the target by "venting" the explosion energy in a direction transverse to the diode plane. Results indicate that for 200 MJ targets, this is not a promising approach.

Chapter 6 is a discussion of the results and their implications on the TDF design.

1.2 Publications

Publications are one method of measuring the productivity of research projects such as this one. Table 1.2 lists our publications during the contract period covered by this report. Four reviewed papers were published and four reviewed talks were given at technical conferences. One unreviewed talk was given at the APS Plasma Physics Division Meeting. University of Wisconsin Fusion Technology Institute Reports are used to document our research in detail. Eight such reports were written, including this report.

1.3 Graduating Students

In addition to the research performed during the contract period we had two students graduate with Ph.D. degrees. These students were supported in part by this contract. Their names, theses, and employment are given in Table 1.3.

Table 1.2. Publications

Reviewed Papers

1. R.R. Peterson, G.A. Moses, R.L. Engelstad, D.L. Henderson, G.L. Kulcinski, E.G. Lovell, M.E. Sawan, I.N. Sviatoslavsky, J.J. Watrous, R.E. Olson, and D.L. Cook, "The Light Ion Fusion Target Development Facility Preliminary Design," Fusion Technology 8, 1895 (1985).

2. D.L. Henderson, G.A. Moses, and R.R. Peterson, "Radioactivity in the Light Ion Fusion Target Development Facility," Fusion Technology 8, 1396 (1985).

3. R.L. Engelstad, E.G. Lovell, and G.A. Moses, "Fatigue Strength Analysis of the Sandia Target Development Facility," Fusion Technology 8, 1890 (1985).

4. G.A. Moses, R.R. Peterson, and T.J. McCarville, "MFFIRE - A Multifrequency Radiative Heat Transfer Hydrodynamics Code," Comp. Phys. Comm. 36, 249 (1985).

Reviewed Talks

1. R.R. Peterson, G.A. Moses, R.L. Engelstad, D.L. Henderson, G.L. Kulcinski, E.G. Lovell, M.E. Sawan, I.N. Sviatoslavsky, J.J. Watrous, R.E. Olson, and D.L. Cook, "The Light Ion Fusion Target Development Facility Preliminary Design," presented at 6th Topical Conference on Fusion Technology, San Francisco, CA, March 1985.

2. D.L. Henderson, G.A. Moses, and R.R. Peterson, "Radioactivity in the Light Ion Fusion Target Development Facility," presented at 6th Topical Conference on Fusion Technology, San Francisco, CA, March 1985.

3. R.L. Engelstad, E.G. Lovell, and G.A. Moses, "Fatigue Strength Analysis of the Sandia Target Development Facility," presented at 6th Topical Conference on Fusion Technology, San Francisco, CA, March 1985.

4. R.R. Peterson, G.A. Moses, and J.J. Watrous, "Z-Discharge Plasma Channels in the Light Ion Fusion Target Development Facility," 1985 IEEE International Conference on Plasma Science, Pittsburgh, PA, June 1985.

5. R.R. Peterson, J.J. Watrous, and G.A. Moses, "Microfireball Propagation in Z-Pinch Plasma Channels," Bull. APS 29, 1350 (1984).

Fusion Technology Institute Reports

1. R.R. Peterson, J.J. Watrous, "Microfireball Propagation in Z-Pinch Plasma Channels in the Light Ion Fusion Target Development Facility," University of Wisconsin Fusion Technology Institute Report UWFDM-613 (Jan. 1985).

Table 1.2 (continued)

2. R.L. Engelstad, E.G. Lovell and G.A. Moses, "Fatigue Strength Analysis of the Sandia Target Development Facility Reaction Chamber," University of Wisconsin Fusion Technology Institute Report UWFDM-618 (Feb. 1985); presented at the Sixth Topical Meeting on the Technology of Fusion Energy, San Francisco, CA, 3-7 March 1985.

3. R.R. Peterson, G.A. Moses, R.L. Engelstad, D.L. Henderson, G.L. Kulcinski, E.G. Lovell, M.E. Sawan, I.N. Sviatoslavsky, J.J. Watrous, R.E. Olson, D.L. Cook, "Light Ion Fusion Target Development Facility Preliminary Design," University of Wisconsin Fusion Technology Institute Report UWFDM-627 (Feb. 1985); presented at the Sixth Topical Meeting on the Technology of Fusion Energy, San Francisco, CA, 3-7 March 1985.

4. D.L. Henderson, R.R. Peterson and G.A. Moses, "Radioactivity Induced in the First Wall of the Light Ion Fusion Target Development Facility," University of Wisconsin Fusion Technology Institute Report UWFDM-628 (Feb. 1985); presented at the Sixth Topical Meeting on the Technology of Fusion Energy, San Francisco, CA, 3-7 March 1985.

5. D.L. Henderson and G.A. Moses, "Activation and Radiological Dose Calculations for the Light Ion Fusion Target Development Facility," University of Wisconsin Fusion Technology Institute Report UWFDM-636 (April 1985).

6. R.L. Engelstad and E.G. Lovell, "Dynamic Response of Target Development Facility Spherical Chambers," University of Wisconsin Fusion Technology Institute Report UWFDM-655 (Oct. 1985).

7. R.L. Engelstad and E.G. Lovell, "Parametric Lifetime Analysis of Cylindrical Chambers for the Target Development Facility," University of Wisconsin Fusion Technology Institute Report UWFDM-656 (Oct. 1985).

8. B. Badger et al., "Light Ion Beam Fusion Target Development Facility Studies: Progress Report for the Period October 1, 1984 to September 30, 1985," University of Wisconsin Fusion Technology Institute Report UWFDM-651 (Sept. 1985).

Table 1.3. Graduating Students Supported in Part by Sandia National Laboratory

Name	Thesis Title	Destination
Lichung Pong	Vapor Condensation in the Presence of a Noncondensable Gas	Postdoctoral - Fusion Reactor Safety Research - Univ. of Wisconsin
Kevin O'Brien	The Adiabatic Theory of the Linear Hose Instability in a Relativistic Electron Beam Propagating in Resistive Plasma	Scientist - Sandia National Laboratory

2. Neutronics and Activation Analysis

The light ion beam fusion target development facility (TDF) is intended to test approximately ten to twelve 50-800 MJ fusion targets per day over a period of five years (~ 15,000 shots over its lifetime). This large number of high yield shots makes the TDF one of the first inertial confinement fusion experiments where radioactivity induced by fusion neutrons could represent a significant biological hazard which would require some form of radiation shield. Therefore, the preliminary design of the facility has the target explosion chamber submerged in a borated water pool below the operating floor as shown in Fig. 2.1. Because the water shield might be lowered for periodic maintenance either in the chamber's interior or exterior and because workers performing this maintenance may be required to come in close contact with the first wall, it is important to determine the biological doses the workers would be receiving near the target chamber.

As an alternative to the borated water pool shield, a design where the target chamber has been enclosed within concrete has also been investigated. As an extension of these designs, the use of an ISSEC (Internal Spectral Shifter and Energy Convertor) structure placed in the interior of the target chamber for the moderation of the high energy neutrons has been examined. This is shown in Fig. 2.2. Two ISSEC materials, graphite and titanium hydride, were considered. Calculations of radioactivity induced in Al-6061-T6 and 2-1/4 Cr-1 Mo steel walls and in fusion targets, one made from BeO and W and the other from CH_2 and Au, have been done. The resultant biological dose of the accumulated radioactive target debris and first wall structure has been computed. These results represent improvements on early calculations[1] which

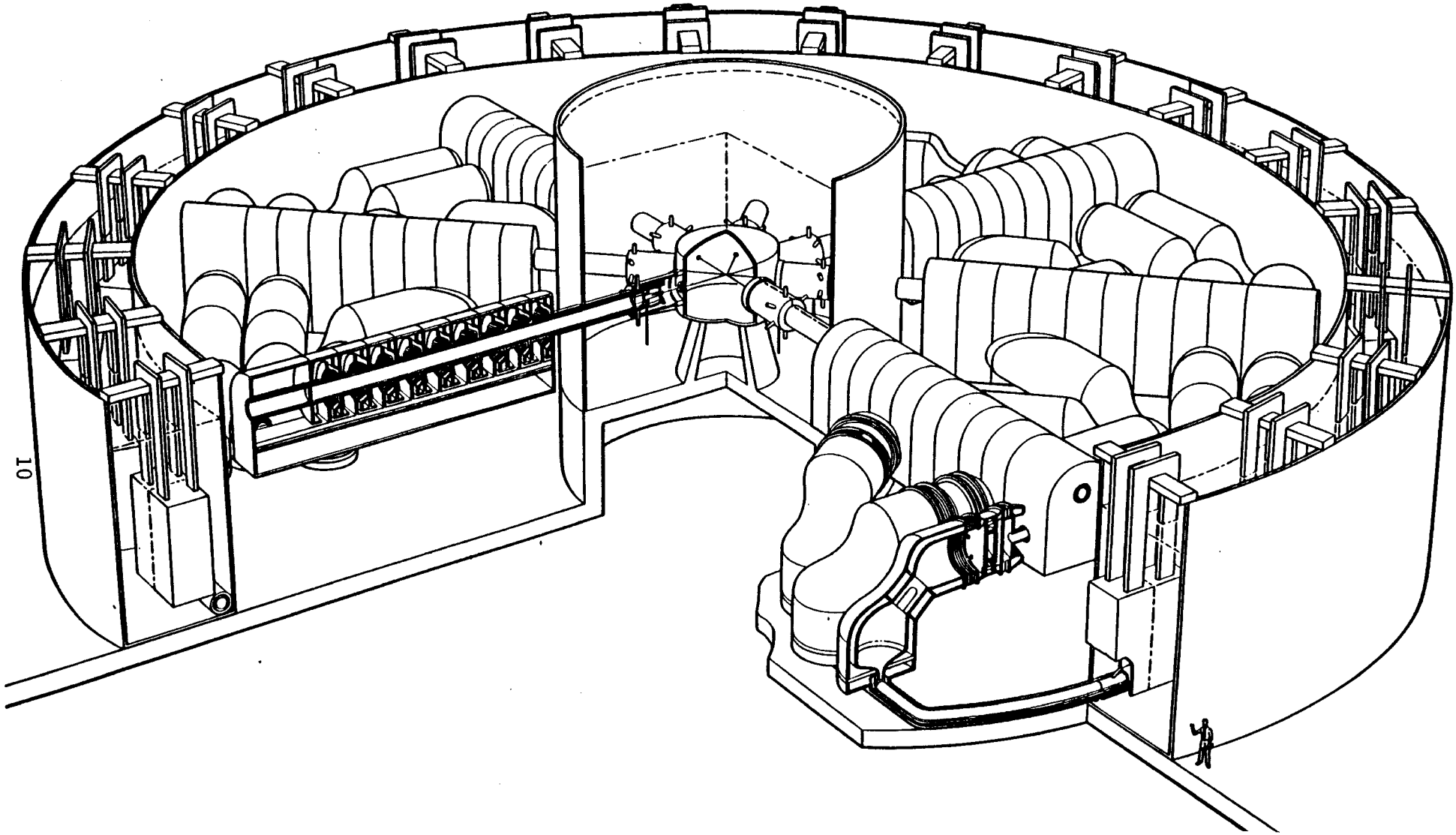

Fig. 2.1. Preliminary design of the Light Ion Fusion Target Development Facility.

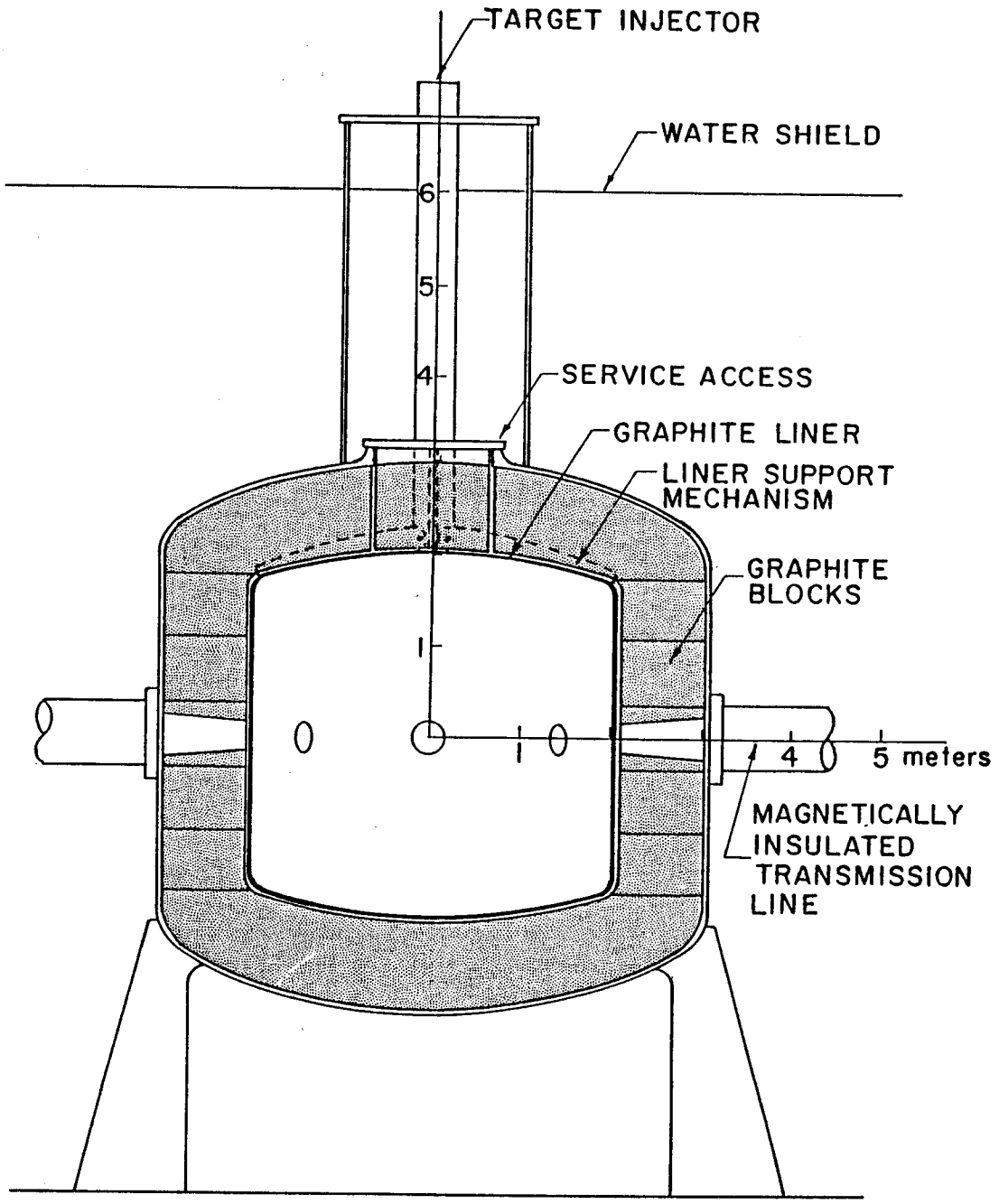

Fig. 2.2. Cut view of TDF chamber with ISSEC structure.

did not consider the effects of the activated target debris and which contained some inaccuracies in the first wall dose rate results.

2.1 Target Activation Analysis

For the radioactive target debris analysis, two ion beam targets are considered. Both are based upon a target design published by Bangerter and Meeker[2] (see Fig. 2.3). The targets are composed of a 1 mg DT region surrounded by a BeO pusher and a W tamper or a CH_2 pusher with a Au tamper. The compressed target configuration used for the neutron transport and neutron activation calculations is shown in Fig. 2.4. A fuel burnup fraction of 30% was assumed giving approximately 100 MJ of released fusion energy with 71 MJ of that being in neutrons.

For a comparison between target debris dose rates and the first wall material doses, the radioactive target debris from each pulse during a 1 year operation span is accumulated onto the interior surface of the first wall. The radioactivity decay between each pulse and accumulation of the debris is computed by a small computer code which treats the target debris radioactivity produced by each pulse as a delta function in time. The pulse sequence is assumed to be 12 shots per day for 5 days per week for 52 weeks per year which amounts to 3120 shots per year.

Figure 2.5 displays the results of the CH_2-Au target constituents. The high initial activity of 1.13×10^3 curies is due to $^{6}_{2}He$. The short lived isotope $^{9}_{3}Li$ is also produced with an initial activity of 18.7 curies. After approximately 3 minutes both isotopes will have decayed away. The remaining radioactive isotopes shown are from neutron interactions on $^{197}_{79}Au$ with the major contributors to the activity after approximately 2 minutes being $^{196}_{79}Au$ and $^{196m}_{79}Au$ (isomeric state of $^{196}_{79}Au$). Both are produced by an (n,2n) reaction

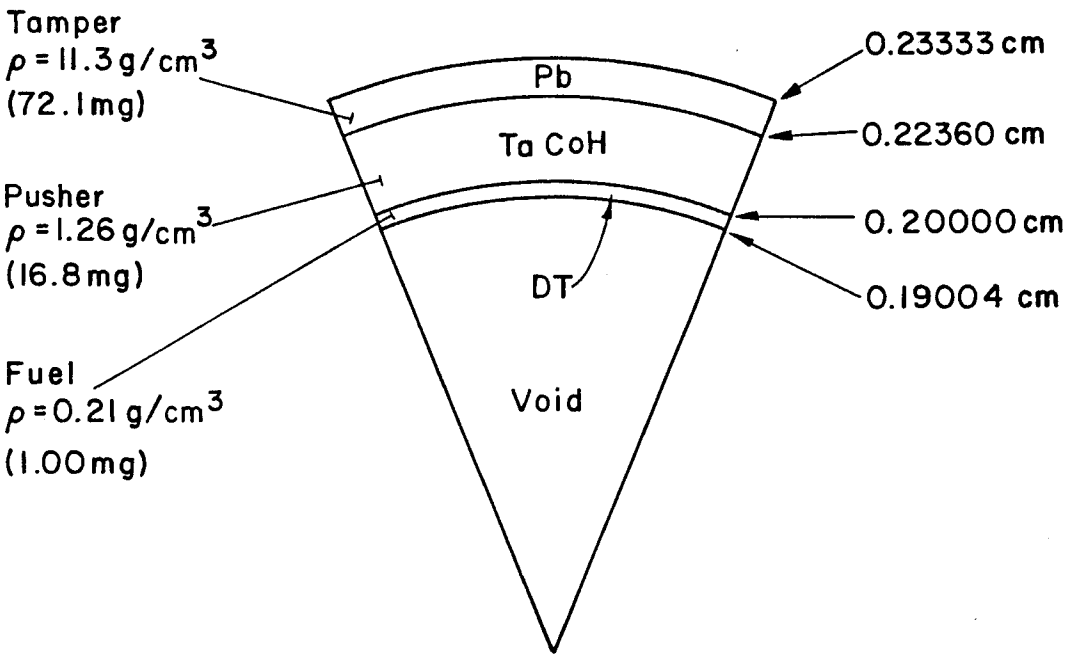

Fig. 2.3. Reference ion beam target as depicted in Ref. 2.

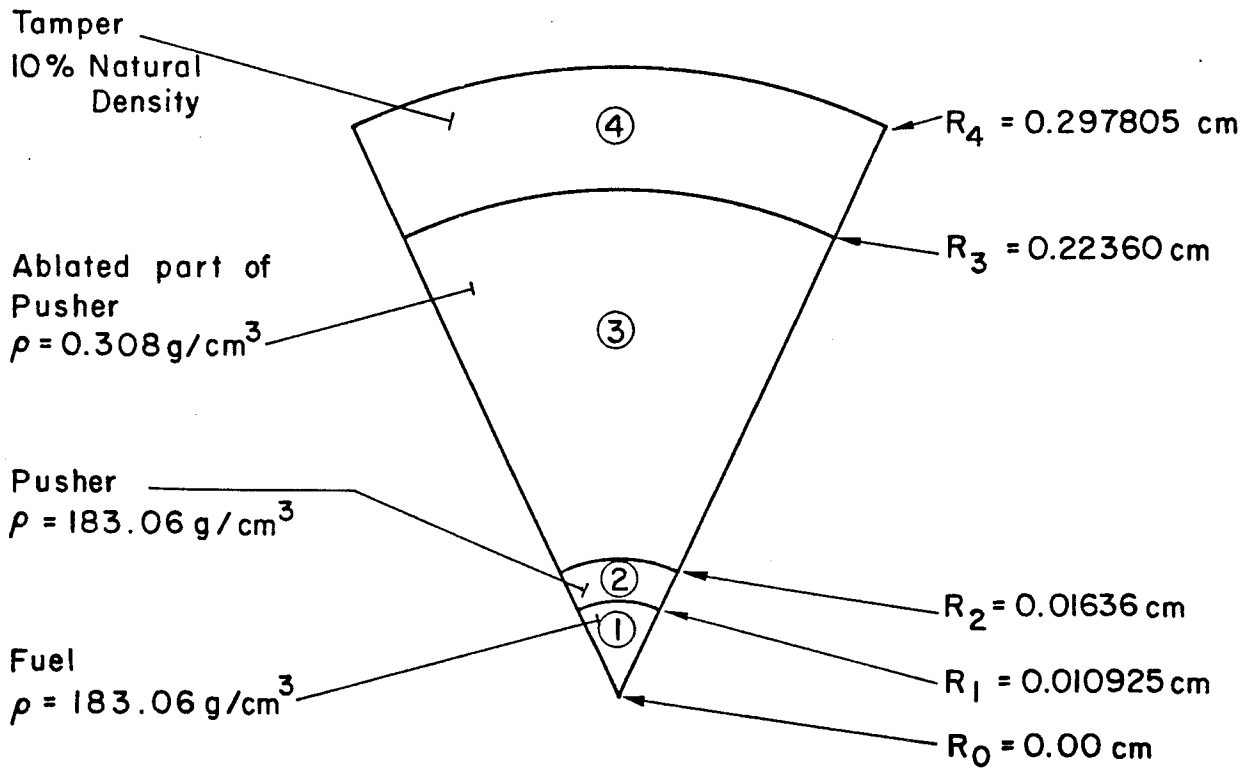

Fig. 2.4. The compressed target configuration used for the target neutronic and radioactivity calculations.

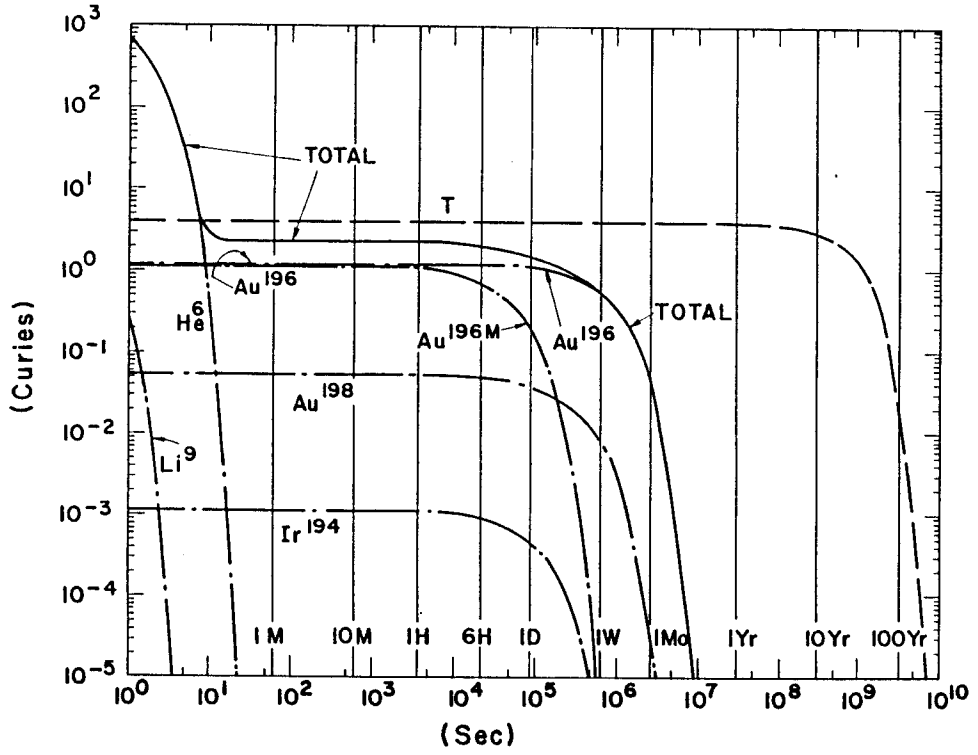

Fig. 2.5. Isotopic activation versus time for the CH_2-Au target.

with $^{197}_{79}Au$. As with the BeO-W target, the low level long term activity is again due to the $^{10}_{4}Be$ and $^{14}_{6}C$ isotopes which have initial activities of 1.11 x 10^{-13} curies and 2.07 x 10^{-14} curies, respectively. The unburnt tritium activity (dashed line) is shown for comparison. Additional information on the production of the radioactive isotopes and resulting stable isotopes can be found in Table 2.1.

A point to note about the results given above is that for times after shutdown of interest for the facility (1 day, 1 week, 1 month after shutdown), the activity of the targets is solely due to the high-Z tamper material. Thus for the chamber wall and target debris dose rate analysis, only the gamma photons emitted by the decay of the activated tamper materials are considered.

2.2 Chamber Activation Analysis

The neutrons emanating from the target are considered as sources for the first wall neutron transport calculation with the energy spectrum of the fusion neutrons shown in Fig. 2.6. The energy spectrum consists of a large peak at 14.1 MeV due to the uncollided flux of neutrons escaping the ignited target. This amounts to 70.75% of the released neutrons. For additional information on the determination and shape of the spectrum, consult Refs. 3 and 4.

The cylindrically shaped target chamber is approximated by spherical geometry and hence the results represent conditions at the midplane of the chamber. The target chamber has an inner radius of 3.0 meters while the first wall is 3.5 cm thick for ferritic steel and 14.8 cm thick for aluminum. The first wall thickness has been determined through fatigue lifetime analysis.[5] A 3.0 m thick water shield with a boron concentration of 2000 wppm is assumed for the water pool design. A schematic of the target chamber with the alumi-

Table 2.1. Nuclear Decay Chains Considered in the Target Activation Analysis

BeO Pusher-W Tamper Target

isotope $^{9}_{4}Be(n,\alpha)\ ^{6}_{2}He \rightarrow$ decays by β^-, $t_{1/2} = 0.810$ s $\rightarrow\ ^{6}_{3}Li$

$^{9}_{4}Be(n,p)\ ^{9}_{3}Li \rightarrow$ decays by β^-, $t_{1/2} = 0.178$ s $\rightarrow\ ^{9}_{4}Be$

$^{9}_{4}Be(n,\gamma)\ ^{10}_{4}Be \rightarrow$ decays by β^-, $t_{1/2} = 1.62 \times 10^{6}$ yrs $\rightarrow\ ^{10}_{5}B$

isotope $^{16}_{8}O(n,p)\ ^{16}_{7}N \rightarrow$ decays by β^-, $t_{1/2} = 7.10$ s $\rightarrow\ ^{16}_{8}O$

$^{16}_{8}O(n,\alpha)\ ^{13}_{6}C \rightarrow\ ^{13}_{6}C(n,\gamma)\ ^{14}_{6}C \rightarrow$ decays by β^-, $t_{1/2} = 5734$ yrs $\rightarrow\ ^{14}_{7}N$

isotope $^{182}_{74}W(n,p)\ ^{182}_{73}Ta \rightarrow$ decays by β^-, $t_{1/2} = 115$ days $\rightarrow\ ^{182}_{74}W$

$^{182}_{74}W(n,2n)\ ^{181}_{74}W \rightarrow$ decays by EC, $t_{1/2} = 121$ days $\rightarrow\ ^{181}_{73}Ta$

$^{182}_{74}W(n,\gamma)\ ^{183}_{74}W \rightarrow\ ^{183}_{74}W(n,n')p\ ^{182}_{73}Ta \rightarrow$ decays by β^-, $t_{1/2} = 115$ days $\rightarrow\ ^{182}_{74}W$

$^{182}_{74}W(n,\gamma)\ ^{183}_{74}W \rightarrow\ ^{183}_{74}W(n,p)\ ^{183}_{73}Ta \rightarrow$ decays by β^-, $t_{1/2} = 5.0$ days $\rightarrow\ ^{183}_{74}W$

isotope $^{183}_{74}W\begin{matrix}(n,d)\\(n,n')p\end{matrix}\ ^{182}_{73}Ta \rightarrow$ decays by β^-, $t_{1/2} = 115$ days $\rightarrow\ ^{182}_{74}W$

$^{183}_{74}W(n,p)\ ^{183}_{73}Ta \rightarrow$ decays by β^-, $t_{1/2} = 5.0$ days $\rightarrow\ ^{183}_{74}W$

$^{183}_{74}W(n,2n)\ ^{182}_{74}W \rightarrow\ ^{182}_{74}W(n,p)\ ^{182}_{73}Ta \rightarrow$ decays by β^-, $t_{1/2} = 115$ days $\rightarrow\ ^{182}_{74}W$

$^{183}_{74}W(n,2n)\ ^{182}_{74}W \rightarrow\ ^{182}_{74}W(n,2n)\ ^{181}_{74}W \rightarrow$ decays by EC, $t_{1/2} = 121$ days $\rightarrow\ ^{181}_{73}Ta$

$^{183}_{74}W(n,\gamma)\ ^{184}_{74}W \rightarrow\ ^{184}_{74}W(n,\alpha)\ ^{181}_{72}Hf \rightarrow$ decays by β^-, $t_{1/2} = 42.7$ days $\rightarrow\ ^{181}_{73}Ta$

$^{183}_{74}W(n,\gamma)\ ^{184}_{74}W \rightarrow\ ^{184}_{74}W\begin{matrix}(n,d)\\(n,n')p\end{matrix}\ ^{183}_{73}Ta \rightarrow$ decays by β^-, $t_{1/2} = 5.0$ days $\rightarrow\ ^{183}_{74}W$

$^{183}_{74}W(n,\gamma)\ ^{184}_{74}W \rightarrow\ ^{184}_{74}W(n,p)\ ^{184}_{73}Ta \rightarrow$ decays by β^-, $t_{1/2}$ = 8.7 hrs $\rightarrow\ ^{184}_{74}W$

$^{183}_{74}W(n,\gamma)\ ^{184}_{74}W \rightarrow\ ^{184}_{74}W(n,\gamma)\ ^{185}_{74}W \rightarrow$ decays by β^-, $t_{1/2}$ = 75.1 days $\rightarrow\ ^{185}_{75}Re$

isotope $^{184}_{74}W(n,\alpha)\ ^{181}_{72}Hf \rightarrow$ decays by β^-, $t_{1/2}$ = 42.7 days $\rightarrow\ ^{181}_{73}Ta$

$^{184}_{74}W(n,d)\ ^{183}_{74}W(n,n')p\ ^{183}_{73}Ta \rightarrow$ decays by β^-, $t_{1/2}$ = 5.0 days $\rightarrow\ ^{183}_{74}W$

$^{184}_{74}W(n,p)\ ^{184}_{73}Ta \rightarrow$ decays by β^-, $t_{1/2}$ = 8.7 hrs $\rightarrow\ ^{184}_{74}W$

$^{184}_{74}W(n,\gamma)\ ^{185}_{74}W \rightarrow$ decays by β^-, $t_{1/2}$ = 75.1 days $\rightarrow\ ^{185}_{75}Re$

$^{184}_{74}W(n,2n)\ ^{183}_{74}W \rightarrow\ ^{183}_{74}W(n,d)\ ^{182}_{74}W(n,n')p\ ^{182}_{73}Ta \rightarrow$ decays by β^-, $t_{1/2}$ = 115 days $\rightarrow\ ^{182}_{74}W$

$^{184}_{74}W(n,2n)\ ^{183}_{74}W \rightarrow\ ^{183}_{74}W(n,p)\ ^{183}_{73}Ta \rightarrow$ decays by β^-, $t_{1/2}$ = 5.0 days $\rightarrow\ ^{183}_{74}W$

$^{184}_{74}W(n,2n)\ ^{183}_{74}W \rightarrow\ ^{183}_{74}W(n,2n)\ ^{182}_{74}W \rightarrow\ ^{182}_{74}W(n,p)\ ^{182}_{73}Ta \rightarrow$ decays by β^-,

$t_{1/2}$ = 115 days $\rightarrow\ ^{182}_{74}W$

$^{184}_{74}W(n,2n)\ ^{183}_{74}W \rightarrow\ ^{183}_{74}W(n,2n)\ ^{182}_{74}W \rightarrow\ ^{182}_{74}W(n,2n)\ ^{181}_{74}W \rightarrow$ decays by EC,

$t_{1/2}$ = 121 days $\rightarrow\ ^{181}_{73}Ta$

isotope $^{186}_{74}W(n,p)\ ^{186}_{73}Ta \rightarrow$ decays by β^-, $t_{1/2}$ = 10.6 min $\rightarrow\ ^{186}_{74}W$

$^{186}_{74}W(n,2n)\ ^{185}_{74}W \rightarrow$ decays by β^-, $t_{1/2}$ = 75.1 days $\rightarrow\ ^{185}_{75}Re$

$^{186}_{74}W(n,\gamma)\ ^{187}_{74}W \rightarrow$ decays by β^-, $t_{1/2}$ = 23.9 hrs $\rightarrow\ ^{187}_{75}Re$

$^{186}_{74}W(n,\alpha)\ ^{183}_{72}Hf \rightarrow$ decays by β^-, $t_{1/2}$ = 1.06 hrs $\rightarrow\ ^{183}_{73}Ta \rightarrow$ decays by β^-,

$t_{1/2}$ = 5.0 days $\rightarrow\ ^{183}_{74}W$

isotope $^{186}_{74}W(n,d)^{185}_{73}Ta \rightarrow$ decays by β^-, $t_{1/2}$ = 49.5 min $\rightarrow {}^{185}_{74}W \rightarrow$ decays by β^-, $t_{1/2}$ = 75.1 days $\rightarrow {}^{185}_{75}Re$

CH_2 Pusher-Au Tamper Target

isotope $^{12}_{6}C(n,\alpha)\,{}^{9}_{4}Be \rightarrow {}^{9}_{4}Be(n,\alpha)\,{}^{6}_{2}He \rightarrow$ decays by β^-, $t_{1/2}$ = 0.810s $\rightarrow {}^{6}_{3}Li$

$^{12}_{6}C(n,\alpha)\,{}^{9}_{4}Be \rightarrow {}^{9}_{4}Be(n,p)\,{}^{9}_{3}Li \rightarrow$ decays by β^-, $t_{1/2}$ = 0.178 s $\rightarrow {}^{9}_{4}Be$

$^{12}_{6}C(n,\alpha)\,{}^{9}_{4}Be \rightarrow {}^{9}_{4}Be(n,\gamma)\,{}^{10}_{4}Be \rightarrow$ decays by β^-, $t_{1/2} = 1.62 \times 10^6$ yrs $\rightarrow {}^{10}_{5}B$

isotope $^{13}_{6}C(n,\gamma)\,{}^{14}_{6}C \rightarrow$ decays by β^-, $t_{1/2}$ = 5734 yrs $\rightarrow {}^{14}_{7}N$

isotope $^{197}_{79}Au(n,\alpha)\,{}^{194}_{77}Ir \rightarrow$ decays by β^-, $t_{1/2}$ = 19.15 hrs $\rightarrow {}^{194}_{78}Pt$

$^{197}_{79}Au(n,2n)\,{}^{196}_{79}Au \rightarrow$ decays by EC, $t_{1/2}$ = 6.17 days $\rightarrow {}^{196}_{78}Pt$

$^{197}_{79}Au(n,\gamma)\,{}^{198}_{79}Au \rightarrow$ decays by β^-, $t_{1/2}$ = 2.67 days $\rightarrow {}^{198}_{80}Hg$

$^{197}_{79}Au(n,2n)\,{}^{196}_{79}Au^{*} \rightarrow$ decays by γ, $t_{1/2}$ = 9.7 hrs $\rightarrow {}^{196}_{79}Au \rightarrow$ decays by EC, $t_{1/2}$ = 6.17 days $\rightarrow {}^{196}_{78}Pt$

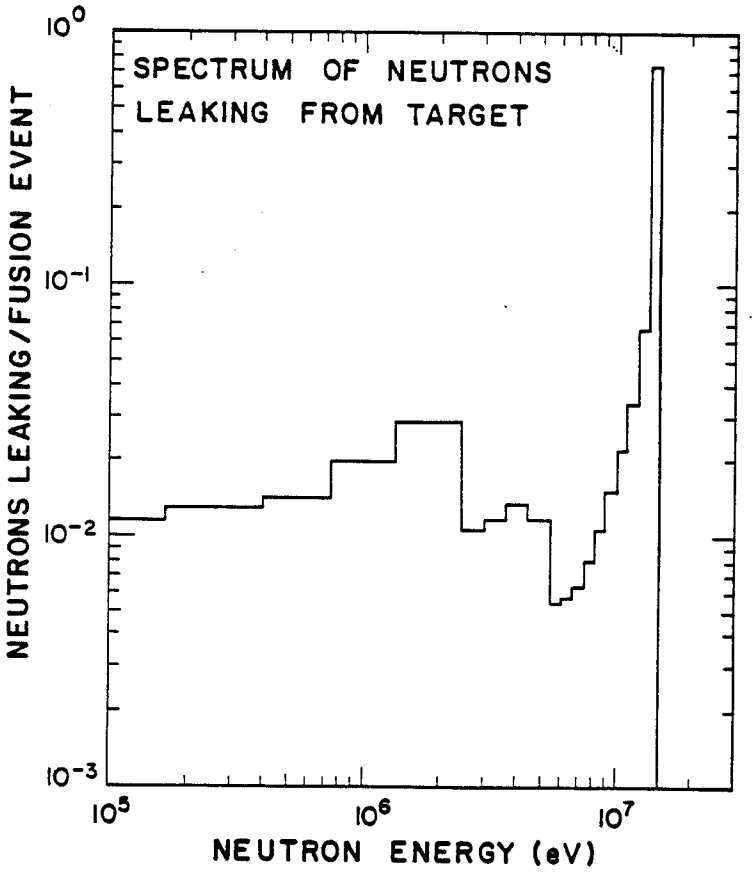

Fig. 2.6. The spectrum of neutrons leaking from the ion beam target normalized to one fusion neutron.

num first wall and borated water shield is shown in Fig. 2.1. The alternative design has the target chamber enclosed by a concrete shield. The materials examined for the ISSEC structures are graphite H-451 and titanium hydride (TiH_2). For the ISSEC designs, Boral[6] sheets (a B_4C-Al mixture and efficient thermal neutron absorber) are placed on either side of the chamber wall. A schematic of the aluminum chamber with the ISSEC structures, boral sheets and borated water shield is displayed in Fig. 2.7.

Since the DKR radioactivity code is a continuous irradiation code, the chamber wall dose rates are computed using an average steady state neutron irradiation flux. The average flux is obtained by averaging the total number of neutrons in the 3120 shots per year over the one year operation period. Thus the dose rate values given assume a continuous one year irradiation of the chamber.

All of the chamber wall and target debris dose rates are normalized to a target yield of 200 MJ and 3120 shots per year. The biological dose rates of the accumulated target debris (BeO-W and CH_2-Au targets), and the steel and aluminum chamber walls have been compared at shutdown and 1 day, 1 week, 1 month and 1 year after shutdown for the borated water pool design. Table 2.2 presents the results for the biological dose rates at the inner surface of the first wall upon which the target debris has accumulated. Several points to note are:

1. A comparison between the dose rates of the accumulated target debris shows that the dose rate of the Au debris is approximately two orders of magnitude higher than that of the W debris through 1 month after shutdown. This changes as the activity of the Au debris decreases rapidly after approximately 3 months. At 1 year after shutdown the dose rate of the W

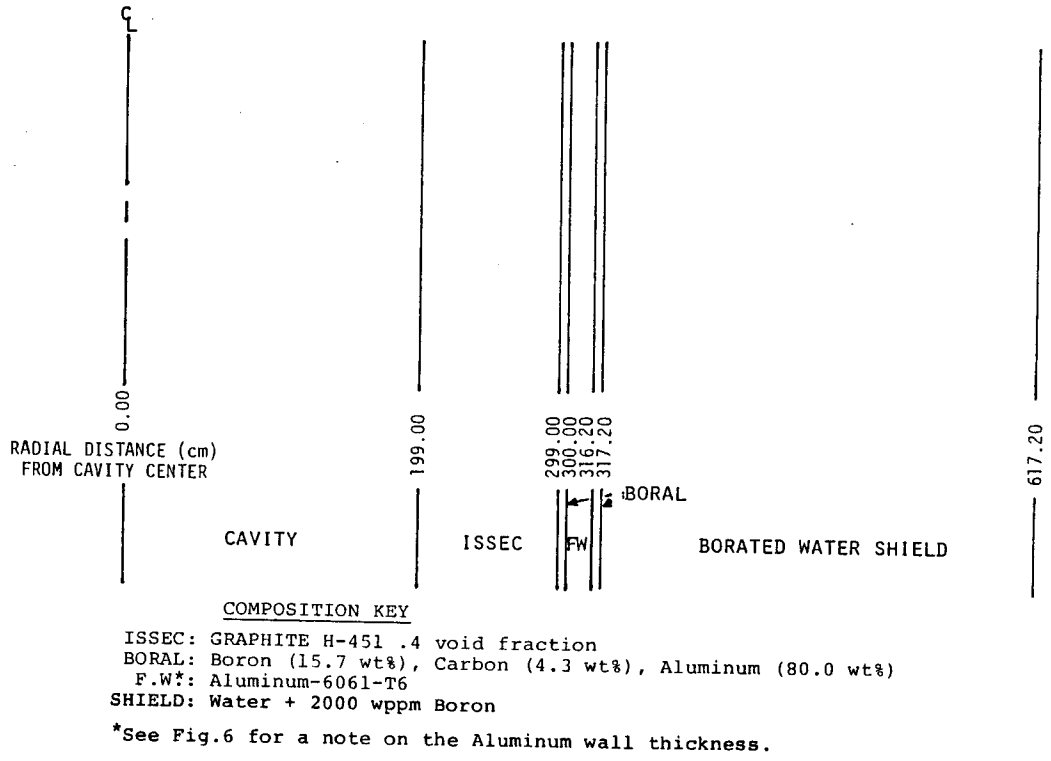

Fig. 2.7. One-dimensional schematic of the Target Development Facility aluminum chamber and shield with graphite ISSEC used for the neutronic and activation calculations.

Table 2.2. Dose Rate (mrem/hr) at Inner Surface of First Wall

	T = 0	T = 1 day	T = 1 wk	T = 1 mo	T = 1 yr
Aluminum First Wall	6.44×10^{6}	1.12×10^{6}	4.26×10^{3}	2.48×10^{3}	1.02×10^{3}
Au (with Al F.W.)	3.05×10^{4}	2.95×10^{4}	1.51×10^{4}	1.08×10^{3}	5.0×10^{-14}
W (with Al F.W.)	6.25×10^{2}	1.88×10^{2}	4.07×10^{1}	2.42×10^{1}	2.49
Steel First Wall	8.54×10^{5}	6.39×10^{4}	5.96×10^{4}	5.22×10^{4}	1.98×10^{4}
Au (with Steel F.W.)	2.72×10^{4}	2.63×10^{4}	1.35×10^{4}	9.57×10^{2}	4.4×10^{-14}
W (with Steel F.W.)	5.84×10^{2}	1.77×10^{2}	3.80×10^{1}	2.33×10^{1}	2.43
Aluminum + Au	6.47×10^{6}	1.15×10^{6}	1.94×10^{4}	3.56×10^{3}	1.02×10^{3}
Aluminum + W	6.44×10^{6}	1.12×10^{6}	4.30×10^{3}	2.50×10^{3}	1.02×10^{3}
Steel + Au	8.81×10^{5}	9.02×10^{4}	7.31×10^{4}	5.32×10^{4}	1.98×10^{4}
Steel + W	8.55×10^{5}	6.41×10^{4}	5.96×10^{4}	5.22×10^{4}	1.98×10^{4}

debris is 2.5 mrem/hr whereas that of the Au debris has become negligibly small.

2. The dose rate of the aluminum chamber wall is larger than that of the steel up to approximately 1 day after shutdown. After a period of 1 week the dose rate of the steel exceeds that of the aluminum.
3. The dose rate of both chamber materials is seen to be considerably larger than that due to the W debris, whereas the dose rate of the Au debris is comparable to the steel at 1 day and 1 week after shutdown and is larger than that of the aluminum at 1 week after shutdown.

Thus one can conclude that at the inner surface of the chamber, depending on the target material composition, the dose rate due to the accumulated target debris can become comparable to that of the chamber itself. Since a liner on the inside of the chamber wall is being considered for protection of the wall from thermal effects of the target explosion, the condensable target debris collected on the liner could be periodically removed, thereby reducing the dose rate component due to the target debris at the inner surface of the chamber wall. Elimination of the Au debris would reduce the combined aluminum wall plus Au debris dose rate to approximately 22% of its present value and the combined steel wall plus Au debris dose rate to approximately 81.5% of its present value at 1 week after shutdown. Even with this reduction, the dose rate within the chamber remains too high for hands on maintenance.

It may be possible to perform underwater maintenance with the water shield in place. The biological dose rate a diver would receive at the outer surface of the target chamber is presented in Table 2.3. Here, as with the dose rates at the inner surface, the target debris dose rate of the Au exceeds that of the W until approximately 3 months after shutdown. Also, the dose rate of the aluminum chamber exceeds that of the steel chamber, but after a 1 week shutdown period, the steel chamber dose rate is larger. One notices now, however, that the target debris dose rate at the outer surface is considerably lower than that of the chamber materials. This is because the gamma photons emitted by the accumulated target debris can be considered as emanating from a surface source and hence are attenuated as they pass through the chamber wall, decreasing the target debris component to the outer surface dose rate. Thus, the dose rates exterior to the chamber wall can essentially be considered to be those of the chamber wall materials. This is again seen in Table 2.4 which

Table 2.3. Dose Rate (mrem/hr) at Outer Surface of First Wall

	T = 0	T = 1 day	T = 1 wk	T = 1 mo	T = 1 yr
Aluminum First Wall	2.75×10^{6}	3.61×10^{5}	1.29×10^{3}	7.18×10^{2}	2.84×10^{2}
Au (with Al F.W.)	4.84×10^{2}	4.66×10^{2}	2.36×10^{2}	1.66×10^{1}	7.7×10^{-16}
W (with Al F.W.)	1.69×10^{1}	5.32	1.27	9.17×10^{-1}	1.04×10^{-1}
Steel First Wall	6.69×10^{5}	3.82×10^{4}	3.54×10^{4}	2.94×10^{4}	8.90×10^{3}
Au (with Steel F.W.)	7.65×10^{2}	7.33×10^{2}	3.68×10^{2}	2.58×10^{1}	1.2×10^{-15}
W (with Steel F.W.)	3.21×10^{1}	1.02×10^{1}	2.38	1.78	2.02×10^{-1}
Aluminum + Au	2.75×10^{6}	3.61×10^{5}	1.53×10^{3}	7.35×10^{2}	2.84×10^{2}
Aluminum + W	2.75×10^{6}	3.61×10^{5}	1.29×10^{3}	7.19×10^{2}	2.84×10^{2}
Steel + Au	6.70×10^{5}	3.89×10^{4}	3.58×10^{4}	2.94×10^{4}	8.90×10^{3}
Steel + W	6.69×10^{5}	3.82×10^{4}	3.54×10^{4}	2.94×10^{4}	8.90×10^{3}

Table 2.4. Dose (mrem/hr) at 27.5 cm from Outer Surface of First Wall

	T = 0	T = 1 day	T = 1 wk	T = 1 mo	T = 1 yr
Aluminum First Wall	5.75×10^{5}	7.66×10^{4}	2.14×10^{2}	1.01×10^{2}	4.06×10^{1}
Au (with Al F.W.)	5.67×10^{1}	5.42×10^{1}	2.71×10^{1}	1.90	8.79×10^{-17}
W (with Al F.W.)	2.76	8.94×10^{-1}	2.35×10^{-1}	1.79×10^{-1}	2.09×10^{-2}
Steel First Wall	2.32×10^{5}	5.18×10^{3}	4.80×10^{3}	3.99×10^{3}	1.20×10^{3}
Au (with Steel F.W.)	1.02×10^{2}	9.71×10^{1}	4.82×10^{1}	3.36	1.56×10^{-16}
W (with Steel F.W.)	5.55	1.80	4.55×10^{-1}	3.49×10^{-1}	4.06×10^{-2}
Aluminum + Au	5.75×10^{5}	7.67×10^{4}	2.41×10^{2}	1.03×10^{2}	4.06×10^{1}
Aluminum + W	5.75×10^{5}	7.66×10^{4}	2.14×10^{2}	1.01×10^{2}	4.06×10^{1}
Steel + Au	2.32×10^{5}	5.28×10^{3}	4.85×10^{3}	3.99×10^{3}	1.20×10^{3}
Steel + W	2.32×10^{5}	5.18×10^{3}	4.80×10^{3}	3.99×10^{3}	1.20×10^{3}

presents the dose rates at 27.5 cm from the outer surface of the chamber wall with borated water in between.

The dose rate a person would receive standing at the edge of the borated water shield at shutdown is 10^4 rem/hr for the aluminum chamber and 2×10^4 rem/hr for the steel chamber. One day after shutdown these values are reduced to 0.25 mrem/hr for the aluminum and 1.7×10^{-4} mrem/hr for the steel. The values at shutdown reflect the activity of the borated water shield (1.2 curies/liter), in particular the $^{16}_{7}N$ isotope which has a 7.1 s half-life. After about 5 to 6 minutes after shutdown the activity of $^{16}_{7}N$ is negligible, therefore the dose rates will be reduced to approximately the values given at 1 day.

The contribution of the thermal neutron albedo from the borated water shield to the dose rates in the wall was investigated with the results presented in Table 2.5. The case labeled "with borated water shield" represents the dose rate calculation for the present preliminary design. The case labeled "without borated water shield" has the shield replaced by vacuum thereby simulating an idealized zero neutron albedo boundary condition (i.e., no neutron return current from the shield) and thus represents the best possible situation. Hence, the difference between the computed dose rates is attributed to the thermal neutron albedo. From Table 2.5 one notices that the thermal neutron albedo contribution changes with the time after shutdown. This is because the individual isotopes contributing to the decay gamma source all decay with different decay constants. At 1 day and 1 week after shutdown, the thermal neutron albedo component contributes more than 50 percent of the steel dose rate compared to only 9.7 and 19.4 percent for the aluminum chamber wall. Thus, the total dose can be reduced by roughly a factor of 2 for the

Table 2.5. Dose in mrem/hr at Aluminum First Wall Outer Surface

Time	With Borated Water Shield	Without Borated Water Shield	Thermal Neutron Contribution
0	2.75×10^6	1.19×10^6	56.73%
1 day	3.16×10^5	3.26×10^5	9.70%
1 week	1.29×10^3	1.04×10^3	19.38%
1 month	7.18×10^2	5.59×10^2	22.14%
1 year	2.84×10^2	2.39×10^2	15.85%

Dose in mrem/hr at Steel First Wall Outer Surface

Time	With Borated Water Shield	Without Borated Water Shield	Thermal Neutron Contribution
0	6.69×10^5	2.74×10^5	59.04%
1 day	3.82×10^4	1.75×10^4	54.19%
1 week	3.54×10^4	1.65×10^4	53.39%
1 month	2.94×10^4	1.55×10^4	47.28%
1 year	8.90×10^4	7.23×10^3	18.76%

steel chamber and 1.1 and 1.25 for the aluminum chamber by increasing the weight percent boron in the borated water shield or by placement of a boral shield on the outer surface of the wall. This reduction does not offer any qualitative difference in the dose rate problem at the wall surface; it still remains too high for hands on maintenance.

2.3 Internal Spectrum Shifter Design

An examination of the nuclide decay chains given by the DKR code[7] shows that the remaining dose rate component is mainly the result of neutron transmutation reactions above neutron threshold values in the MeV energy range.

Table 2.6 presents the radioactive isotopes which produce more than 90 percent of the gamma photons at various times after shutdown. The neutron transmutation reactions and threshold energies of the initial stable isotopes and the resulting radioactive isotopes of Table 2.6 are found in Table 2.7. Therefore, to reduce the dose rates significantly, the large component of high energy neutrons must be reduced below the neutron threshold values prior to their interaction with the first wall.

To achieve this, two ISSEC (Internal Spectrum Shifter and Energy Convertor) structures, one made of graphite and the other of titanium hydride, are considered with each of the chamber wall materials. Figure 2.2 shows a cut view of the target chamber with the graphite ISSEC.

Figure 2.8 displays the neutron group flux spectrum within the first mesh cell of the aluminum chamber wall for the ISSEC structures considered. For all of the ISSEC structures considered, the high energy neutron component is reduced. The best result is achieved with the 40% porosity carbon ISSEC structure.

For the following comparisons, the outer surface of the second boral zone for the ISSEC structure cases corresponds approximately to the first wall outer surface (bare first wall) and will be referred to as the first wall outer surface. Also, the ISSEC structure outer surface will be referred to as the first wall inner surface as they correspond approximately to the same position. The ISSEC structure inner surface has no equivalent in the bare first wall cases, thus it will be referred to as the ISSEC inner surface.

Table 2.8 presents a comparison of the dose rates for the aluminum chamber wall with and without the presence of the 40% porosity carbon ISSEC structure. As the comparison shows, the decrease in the dose rate due to the pre-

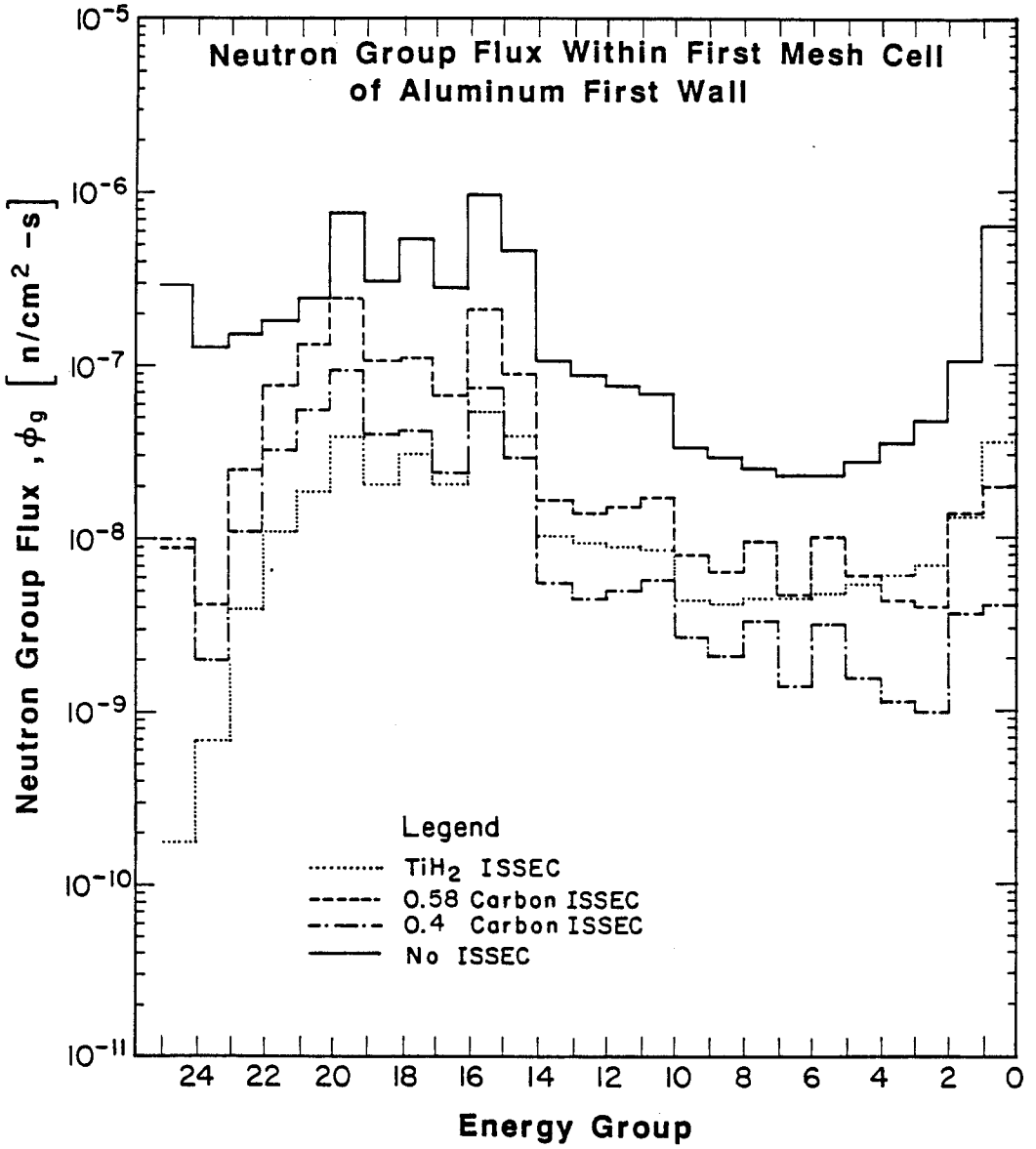

Fig. 2.8. Neutron group flux within first mesh cell of the aluminum chamber wall.

Table 2.6. Important Gamma-Photon Producing Isotopes

Chamber Wall: 2-1/4 Cr-1 Mo Steel

Time 0	1 day	1 week	1 month	1 year
Al-28	Cr-51	Cr-51	Cr-51	Mn-54
Cr-51	Mn-54	Mn-54	Mn-54	
V-52	Fe-59	Fe-59	Fe-59	
Mn-54				
Mn-56				
Fe-59				

Chamber Wall: Aluminum-6061-T6

Time 0	1 day	1 week	1 month	1 year
Na-24	Na-24	Cr-51	Cr-51	Mn-54
Mg-27		Mn-54	Mn-54	
Al-28				

Borated Water Shield

Time 0	1 day	1 week	1 month	1 year
N-16	---	---	---	---

sence of the ISSEC structure is approximately a factor of 1000 at the first wall inner surface and a factor of 100 at the first wall outer surface. Noticeable for the ISSEC structure values, is the large drop in the dose rates to more tolerable levels over the 1 day to 1 week time period after shutdown with the dose rates being 4050 mrem/hr and 13.1 mrem/hr, respectively. This is due to the decay of the $^{24}_{11}Na$ radionuclide which has a half life of 15

Table 2.7. Neutron Transmutation Reactions Leading to the Radioactive Isotopes in Table 17

2-1/4 Cr-1 Mo Steel Chamber Wall

Reaction(s)	Decay Mode	Threshold Energy (Ref. 17)
$^{28}_{14}Si(n,p)\ ^{28}_{13}Al$	β^-	4.0 MeV (n,p)
$^{52}_{24}Cr(n,p)\ ^{52}_{23}V$	β^-	3.3 MeV (n,p)
$^{52}_{24}Cr(n,2n)\ ^{51}_{24}Cr$	EC	12.3 MeV (n,2n)
$^{53}_{24}Cr\ ^{(n,d)}_{(n,n')p}\ ^{52}_{23}V$	β^-	9.1 MeV (n,d)
$^{54}_{26}Fe(n,\gamma)\ ^{55}_{26}Fe \rightarrow EC \rightarrow\ ^{55}_{25}Mn(n,2n)\ ^{54}_{25}Mn$	EC	10.4 MeV (n,2n)
$^{56}_{26}Fe(n,t)\ ^{54}_{25}Mn$	EC	12.1 MeV (n,t)
$^{56}_{26}Fe(n,p)\ ^{56}_{25}Mn$	β^-	3.0 MeV (n,p)
$^{57}_{26}Fe\ ^{(n,d)}_{(n,n')p}\ ^{56}_{25}Mn$	β^-	8.5 MeV (n,d)
$^{57}_{26}Fe(n,\gamma)\ ^{58}_{26}Fe \rightarrow\ ^{58}_{26}Fe(n,\gamma)\ ^{59}_{26}Fe$	β^-	---
$^{58}_{26}Fe(n,t)\ ^{56}_{25}Mn$	β^-	12.3 MeV (n,t)

Isotope	Primary Gamma (Ref. 15) Energy (MeV)	Secondary Gamma Energy (MeV)
$^{28}_{13}Al$	1.78	---
$^{52}_{23}V$	1.43	---
$^{51}_{24}Cr$	0.325	0.7
$^{54}_{25}Mn$	0.836	---
$^{56}_{25}Mn$	0.845	1.81
$^{59}_{26}Fe$	1.29	1.10

Aluminum-6061-T6 Chamber Wall

Reaction	Decay Mode	Threshold Energy
$^{24}_{12}Mg(n,p)\ ^{24}_{11}Na$	β^-	4.9 MeV (n,p)
$^{26}_{12}Mg(n,\gamma)\ ^{27}_{12}Mg$	β^-	---
$^{27}_{13}Al(n,p)\ ^{27}_{12}Mg$	β^-	1.9 MeV (n,p)
$^{27}_{13}Al(n,\alpha)\ ^{24}_{11}Na$	β^-	3.3 MeV (n,α)
$^{27}_{13}Al(n,\gamma)\ ^{28}_{13}Al$	β^-	---
$^{28}_{14}Si(n,p)\ ^{28}_{13}Al$	β^-	4.0 MeV (n,p)
$^{52}_{24}Cr(n,2n)\ ^{51}_{24}Cr$	EC	12.3 MeV (n,2n)
$^{56}_{26}Fe(n,t)\ ^{54}_{25}Mn$	EC	12.1 MeV (n,t)

Isotope	Primary Gamma Energy (MeV)	Secondary Gamma Energy (MeV)
$^{24}_{11}Na$	2.75	1.37
$^{27}_{12}Mg$	0.84	1.01
$^{28}_{13}Al$	1.78	---
$^{51}_{24}Cr$	0.325	0.7
$^{54}_{25}Mn$	0.836	---

Borated Water Shield

Reaction	Decay Mode	Threshold Energy
$^{16}_{8}O(n,p)\ ^{16}_{7}N$	β^-	10.2 MeV (n,p)

Isotope	Primary Gamma Energy (MeV)	Secondary Gamma Energy (MeV)
$^{16}_{7}N$	6.13	7.11

Table 2.8. Dose Rate Comparison Between Pure Aluminum First Wall and Aluminum Chamber with 40% Porosity Graphite ISSEC

Dose Rates (mrem/hr)

Time After Shutdown	ISSEC* Inner Surface	ISSEC* Outer Surface	Inner+ Surface of First Wall	Outer* Surface of Second Boral Zone	Outer+ Surface Of First Wall
At shutdown	3.54×10^3	8.06×10^4	(6.44×10^6)	3.81×10^4	(2.75×10^6)
1 min	2.87×10^3	6.73×10^4	---	3.14×10^4	---
10 min	1.01×10^3	3.09×10^4	---	1.56×10^4	---
1 hr	7.37×10^2	2.40×10^4	---	1.23×10^4	---
6 hr	5.76×10^2	1.86×10^4	---	9.46×10^3	---
1 day	2.51×10^2	7.98×10^3	(1.12×10^6)	4.05×10^3	(3.61×10^5)
1 week	3.80	25.2	(4.26×10^3)	13.1	(1.29×10^3)
1 month	2.47	12.7	(2.48×10^3)	6.67	(7.18×10^2)
1 year	0.24	4.61	(1.02×10^3)	2.44	(2.84×10^2)

*TDF chamber with carbon ISSEC (0.4 void fraction)

+TDF chamber without ISSEC

hours. The lowest dose rate values are achieved at the ISSEC inner surface. This is a result of both the low activation of the graphite and its impurities and also the attenuation of the aluminum chamber wall gamma photons as they pass through the ISSEC structure. Target debris is not included in this analysis.

Figure 2.9 is a plot of the fractional contribution to the total dose rate for several major contributing isotopes versus time after shutdown for the aluminum chamber wall with the 40% porosity carbon ISSEC structure. Noticeable is the sharp drop in the $^{24}_{11}Na$ contribution beginning at 5 days after shutdown. At 1 week after shutdown the total dose rate has dropped to 13.1 mrem/hr (see Table 2.8) with $^{24}_{11}Na$ and $^{54}_{25}Mn$ having equal contributions. As the $^{24}_{11}Na$ radionuclide decays away the $^{54}_{25}Mn$ radionuclide begins to dominate the total dose. At 29 days after shutdown, its contribution to the total dose rate is approximately 75%. As the shutdown time increases, its dominance steadily increases until at 1 year after shutdown, its dominance is above 96%. Thus, the two major contributing isotopes to the dose rate for this case are $^{24}_{11}Na$ and $^{54}_{25}Mn$.

The best combination of target chamber wall material and ISSEC structure is the aluminum chamber wall with a carbon ISSEC structure. Dose rate at 1 day and 1 week after shutdown versus porosity of a 1 meter thick graphite ISSEC structure, Fig. 2.10, was made by extrapolating the results obtained from the two point design calculations. The bare aluminum chamber wall cases are indicated and correspond to 100% porosity. A comparison of ISSEC designs is given in Fig. 2.11 where the dose rate at the outer surface of the first wall is plotted vs. time.

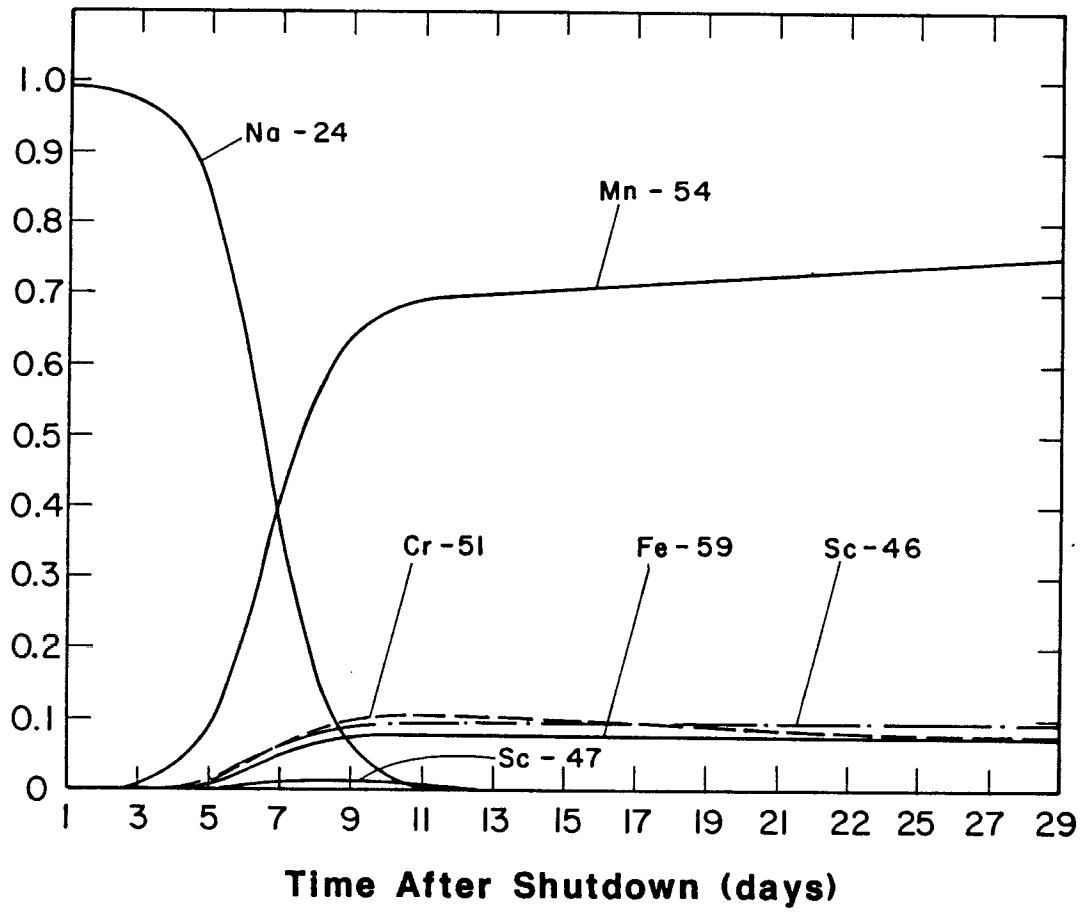

Fig. 2.9. Fractional contribution to the total dose rate for several major contributing isotopes for the TDF aluminum chamber with 40% porosity carbon ISSEC after 1 year of operation.

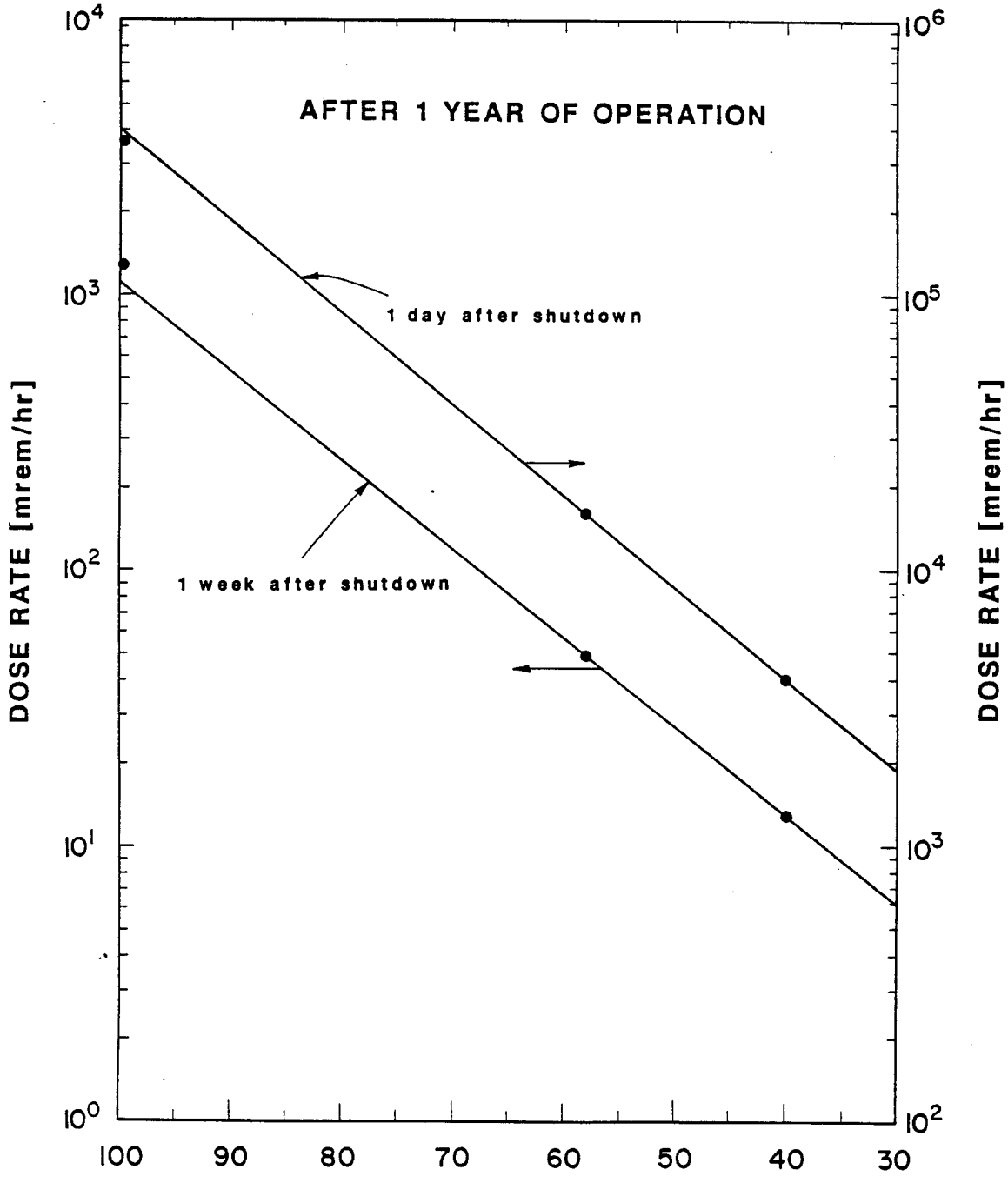

Fig. 2.10. Dose rate versus porosity of carbon ISSEC in a 1 meter thickness zone.

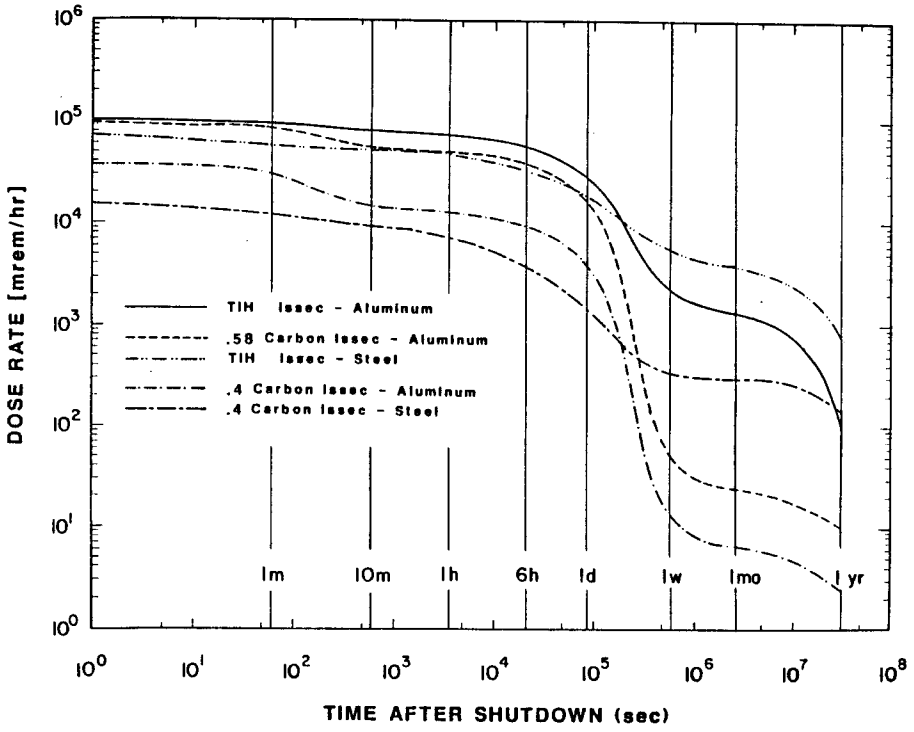

Fig. 2.11. Dose rate at the chamber wall outer surface versus time after shutdown for the 5 different design cases involving ISSEC structures.

2.4 Maintenance Schedule

An aluminum chamber wall with a carbon ISSEC can substantially lower the value for the dose rate at the first wall outer surface at 1 week after shutdown. This case will serve as the basis for the definition of a maintenance schedule.

As the Target Development Facility is an experimental facility, access to the ion diodes relatively soon after the last shot is important. Thus it is essential to have detailed knowledge of the dose rates for the first several days after shutdown of the facility. Table 2.9 presents the dose rate at half day intervals for the time period 1 day through 1 week. Beginning at 1 day after shutdown, the dose rate drops approximately by a factor of 1.74 each half day period until 4 days after shutdown. It is to be remembered that during this time period the $^{24}_{11}Na$ radionuclide dominates the total dose rate.

Using the information presented in Table 2.9 and having identified the major contributors to the dose rate between 1 day and 1 week after shutdown the total integrated dose that a person would receive working in this radiation environment is calculated. The maintenance schedules presented are based on the following criteria: 5 rem per year, an average of 1.25 rem per quarter, 3 rem for the worst quarter with an average of 2/3 rem per quarter available for the remaining 3 quarters, 13 weeks per quarter. The position chosen was the outer surface of the second boral zone. Two maintenance schedules are suggested: the first has the maintenance period as 2 days for which a worker would be working 8 hours per day and the second has a 12 hour continuous working period.

Table 2.10 presents the 2 day maintenance period working schedule. The schedule is broken up into four different operating + waiting period cycles

Table 2.9. Dose Rates for Aluminum Chamber with 40% Porosity Graphite ISSEC at Half Day Intervals

Dose Rates (mrem/hr)

Time After Shutdown	ISSEC Inner Surface[+]	ISSEC Outer Surface	Outer Surface Second Boral
At shutdown	3.54×10^3	8.06×10^4	3.81×10^4
1 day	2.51×10^2	7.98×10^3	4.05×10^3
1.5 days	1.46×10^2	4.58×10^3	2.33×10^3
2 days	85.7	2.64×10^3	1.34×10^3
2.5 days	50.9	1.52×10^3	7.72×10^2
3 days	31.0	8.79×10^2	4.46×10^2
3.5 days	19.4	5.11×10^2	2.59×10^2
4 days	12.8	3.00×10^2	1.52×10^2
4.5 days	8.93	1.79×10^2	91.0
5 days	6.68	1.09×10^2	55.7
5.5 days	5.35	69.1	35.4
6 days	4.57	46.1	23.7
6.5 days	4.09	32.8	17.0
1 week	3.80	25.2	13.1

[+]Values are for a carbon ISSEC having 0.4 void fraction

Table 2.10. Maintenance Schedule for the Target Development Facility with Aluminum Chamber with 40% Porosity Graphite ISSEC

Criteria

1.25 rem per quarter

3 rem for worst quarter

Outer surface of second boral zone

2 days of maintenance work @ 8 hours per day

13 weeks per quarter gives 91 days per quarter

	Operate 4.5 Days Wait 3.5 Days	Operate 4.5 Days Wait 4.5 Days	Operate 4.5 Days Wait 5.5 Days	Operate 4.5 days Wait 6.5 Days
Dose rate at beginning	259 mrem/hr	91.0 mrem/hr	35.4 mrem/hr	17.0 mrem/hr
Dose rate at end	65.0 mrem/hr	26.7 mrem/hr	14.1 mrem/hr	9.96 mrem/hr
Dose received during one work cycle	2.36 rem	0.861 rem	0.369 rem	0.207 rem
Cycles/quarter	9.75	8.81	8.03	7.38
Work to receive 1.25 rem	0.53 cycles	1.45 cycles	3.39 cycles	6.04 cycles
Work to receive 3 rem	1.27 cycles	3.48 cycles	8.13 cycles	14.49 cycles
Work to receive 0.67 rem	0.28 cycles	0.77 cycles	1.81 cycles	3.22 cycles

with the operating period being 4.5 days of testing. As an example of the schedule let's choose the column: operate 4.5 days -- wait 6.5 days. The dose rate at the beginning of the maintenance period (in this case it's after 6.5 days of waiting) is 17.0 mrem/hr and at the end of the second day maintenance period, the dose rate is 9.96 mrem/hr. The integrated dose received during the maintenance period by the worker is 0.207 rem. This is labeled as "Dose received during one work cycle." The number of such operating + working cycles in one quarter year is given in the next row. For our example this is 7.4. The number of cycles a worker can work to receive the average dose of 1.25 rem is 6 cycles (i.e., the worker rests 1 cycle per quarter). To receive a dose of 3 rem, the worker can work 14.5 cycles and to receive 2/3 rem the worker can only work 3.2 cycles. Thus, as one views Table 2.10, one notices that the column "operate 4.5 days -- wait 6.5 days," has the best match between cycles/quarter and work to receive the average dose of 1.25 rem.

Our latest examination of the dose rates after a single pulse in comparison to the continuous irradiation approximation used in the reported analysis reveals that the short-lived isotopes, some of which contribute to the dose rate up to 1 hr after shutdown, are affected most by the pulse nature of the facility. For the aluminum target chamber, preliminary calculations indicate that the pulse sequence or operation sequence chosen for the facility may influence the dose rate component attributed to $^{24}_{11}Na$ up to a factor of 2, which in turn would affect the chamber maintenance. On the same note, the saturation period for $^{24}_{11}Na$ is approximately 1 week so that any problems associated with it will be present whether one operates the facility for 1 week or for 1 year. Investigation of the pulsed nature of the TDF and its effects on activation and dose are continuing.

References for Chapter 2

1. K.J. O'Brien, G.A. Moses, A.M. White, "Neutron Activation and Shielding of the Light Ion Fusion Target Development Facility," Nucl. Tech./Fusion 4, 883 (1983).

2. R.O. Bangerter, "Ion Beam Targets, Laser Program Annual Report - 1976," UCRL-50021-76, Lawrence Livermore National Laboratory, Section 4.2.

3. D.L. Henderson, A.M. White, G.A. Moses, "Target Material Activation Calculations for High Gain Light Ion Fusion Targets," University of Wisconsin Fusion Technology Institute Report UWFDM-572 (1984).

4. B. Badger et al., "HIBALL - A Conceptual Heavy Ion Beam Driven Reactor Study," University of Wisconsin Fusion Technology Institute Report UWFDM-450, KfK-3202, Part I, Chapter III (1981).

5. R.L. Engelstad, E.G. Lovell, G.A. Moses, "Fatigue Strength Analysis of the Sandia Target Development Facility Reaction Chamber," Sixth Top. Mtg. on the Tech. of Fusion Energy, San Francisco, CA, 3-7 March 1985.

6. Theodore Rockwell, III, Reactor Shielding Design Manual, D. Van Nostrand Company (1956), p. 189.

7. Tak Yun Sung, "DKR: A Radioactivity Calculation Code for Fusion Reactors," University of Wisconsin Fusion Technology Institute Report UWFDM-170 (1976).

3. Mechanical Analysis of the Target Chamber

3.1 General Considerations for Cylindrical Chambers

This section summarizes improvements in the mechanical analysis lifetime computations for basic TDF chambers. Complete details are available in UWFDM-656.[1]

Earlier estimates of fatigue life were based upon conservative guidelines from the ASME Pressure Vessel Code. The magnitudes of the peak pressures generated at the chamber wall by the microfireball shock were used with dynamic load factors restricted to be not less than unity. This procedure has been replaced by a less conservative but more accurate technique using the impulse value of the shock. The response is essentially determined by the impulse magnitude rather than the pulse shape and peak pressure if the mean pulse width is considerably less than the vibration periods. This representation also facilitates the generation of parametric data. In previous calculations, the maximum dynamic pressure was also conservatively doubled to account for uncertainties in the microfireball numerical modeling. The current work does not use this additional factor.

For cylindrical chambers, extreme stresses and strains are flexural at the ends, and circumferential over most of the unsupported length. Procedures for the determination of these have been improved. In addition, fatigue calculations are now based upon strain criteria, which is necessary for an accurate assessment of the effects of intense dynamic loads from a limited number of shots.

3.2 Fatigue Summary for the Base Case Cylinder

The base case design is a cylindrical shell with radius and effective height of 3 m and 2 m, respectively, and a wall thickness not less than 3 cm.

Materials considered are 2.25 Cr-1 Mo ferritic steel and 6061-T6 aluminum unwelded and welded. Target yield is 200 MJ with the corresponding impulse 110 Pa-s. With these parameters and 2% damping, displacement and stress histories have been determined using the relevant axisymmetric harmonics.

Maximum axial flexural stress occurs at the ends of the cylinder. Results for a 3 cm steel wall are shown in Fig. 3.1. Increasing the wall thickness will decrease the peak stress. For example, the maximum stress can be reduced by more than a factor of two by doubling the wall thickness as indicated in Fig. 3.2. This stress distribution is characterized by a rather steep axial gradient and thus can be controlled by a localized increase in thickness near the ends, i.e., a hub. In the greater percentage of the shell which excludes the ends, the dominant stress is circumferential. The design thickness is based upon this value which is more uniformly distributed and also of smaller amplitude. For comparison purposes, Fig. 3.3 is the circumferential stress history corresponding to Fig 3.1.

The stress and strain histories are characterized by multiple cycles of different amplitudes. Thus cumulative damage criteria are used to assess chamber lifetimes. The ASME Pressure Vessel Code procedures for cumulative damage are followed. This involves the determination of the effects of the number of applied cycles of various amplitudes as compared with the number of corresponding design allowable cycles. Instead of the Code's stress design curves, the material properties used consist of fully reversed alternating strain as a function of the number of cycles to failure. With such basic data, the guidelines call for safety factors of two on strain magnitude or twenty on cycles, whichever is more conservative. This is the only formal inclusion of a safety factor in the analysis and design.

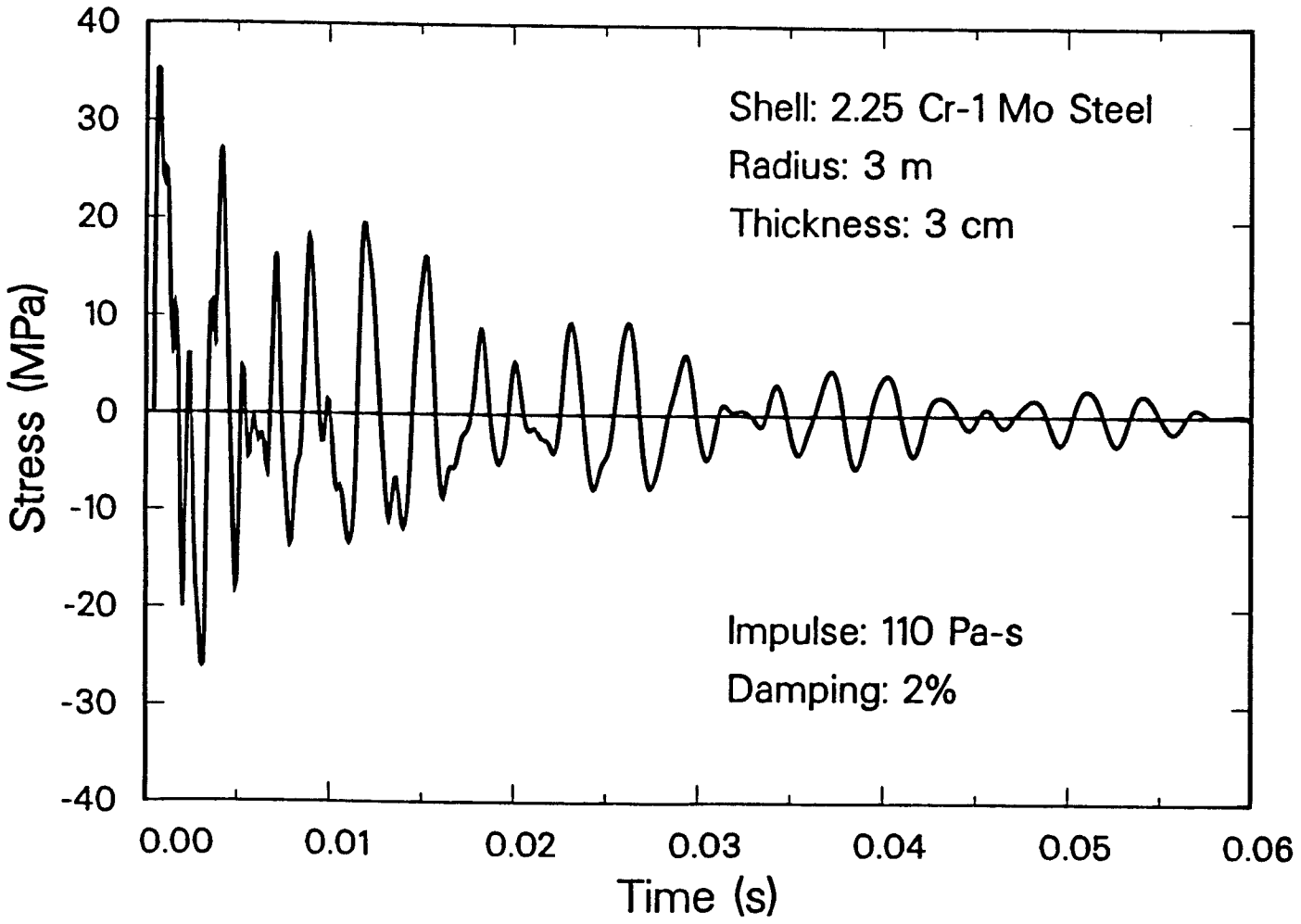

Fig. 3.1. TDF cylindrical shell flexural mechanical stress.

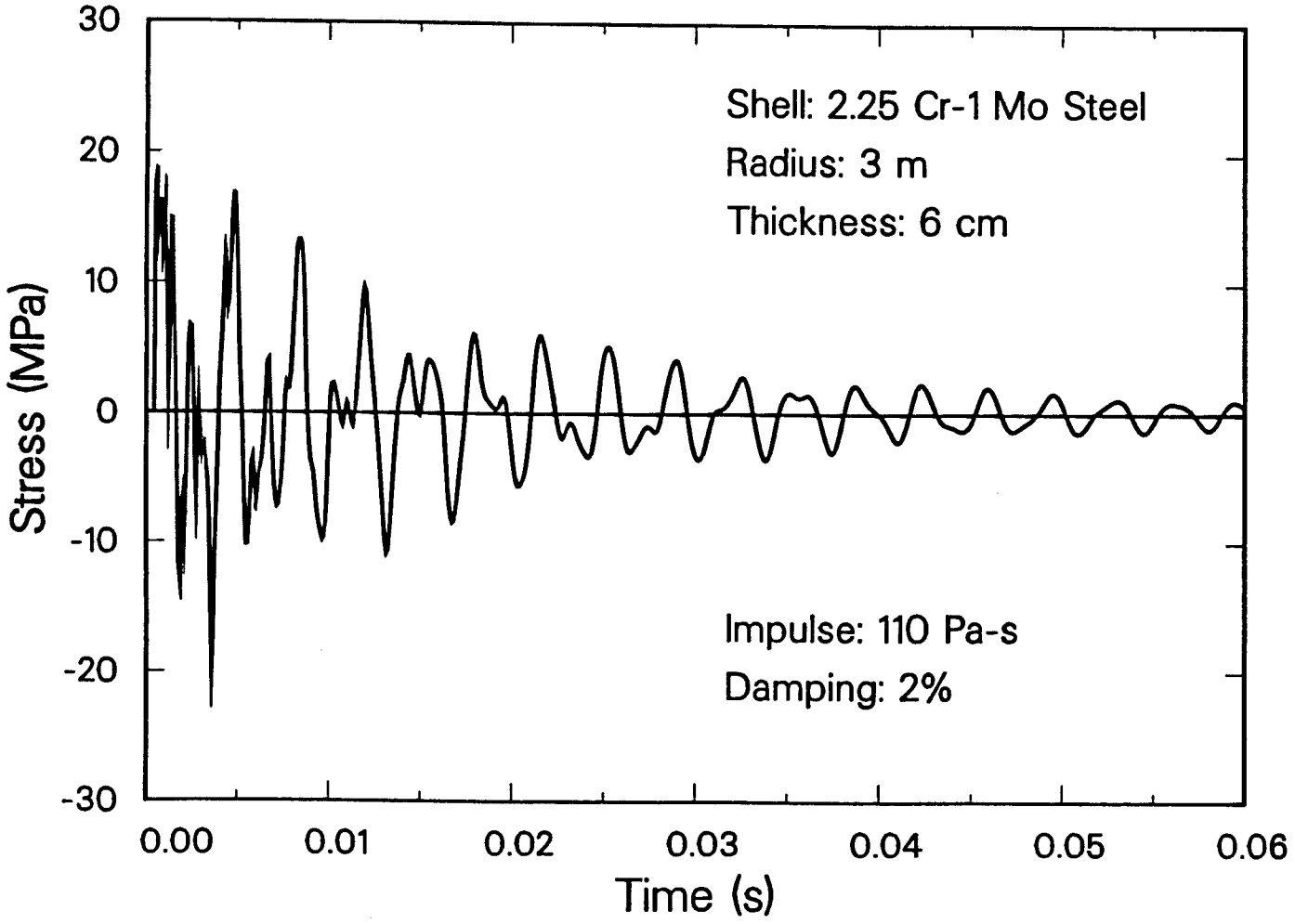

Fig. 3.2. TDF cylindrical shell flexural mechanical stress.

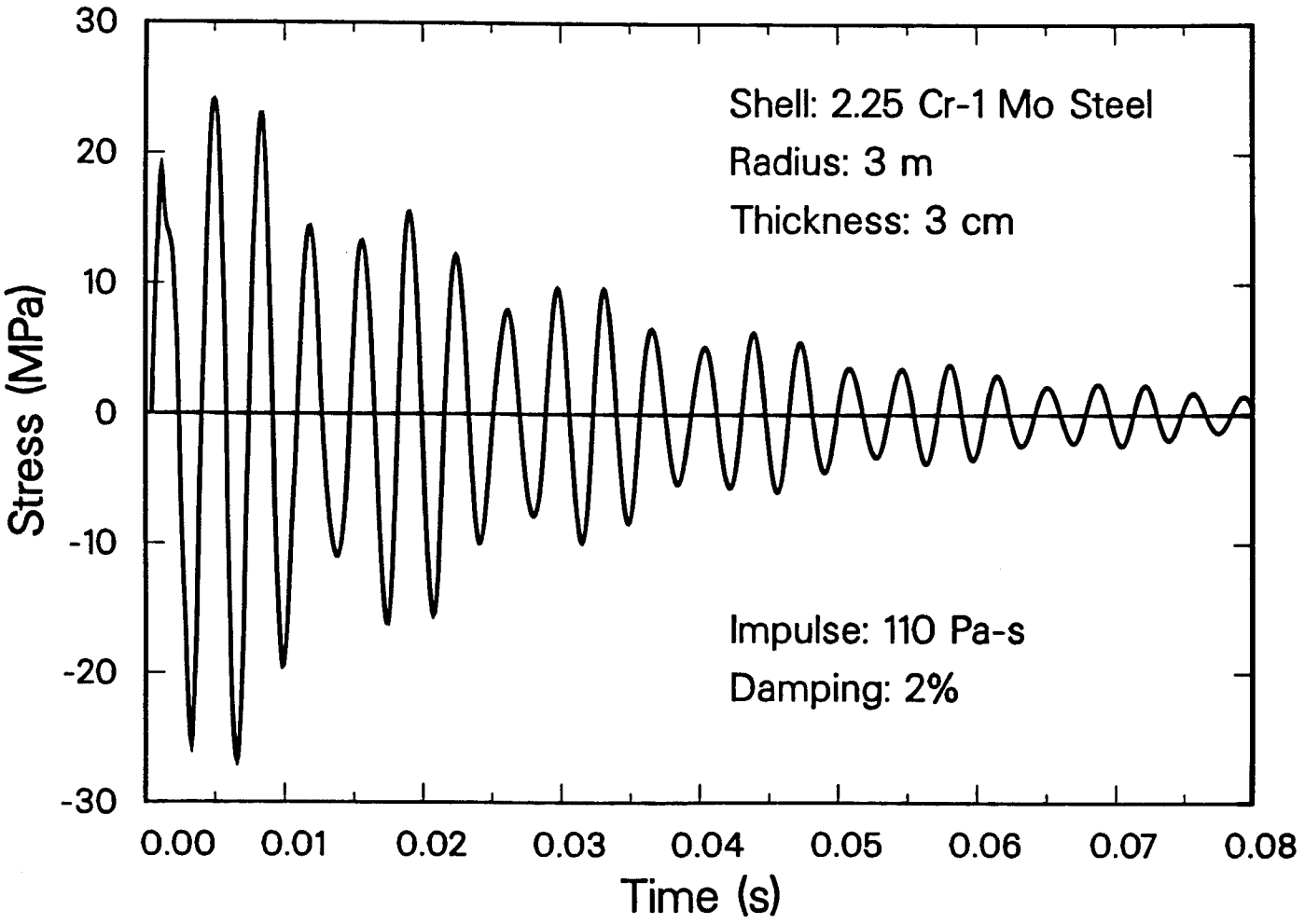

Fig. 3.3. TDF cylindrical shell circumferential mechanical stress.

A computer code has been developed for the determination of fatigue life. The principal steps in the program include accurately calculating natural frequencies and mode shapes for a specific material, thickness, radius and length. The displacement and strain histories are then determined for each value of the impulsive loading. Typical examples are shown in Figs. 3.4 and 3.5 for steel and aluminum base cases with 3 cm walls. A counting procedure is applied to each history, assessing cumulative damage and comparing with stored data for strain amplitude as a function of cycles to failure. This results in identification of the number of shots permissible for a given chamber subjected to impulsive pressures spanning the range of interest. The process is then repeated completely for a change in one parameter, e.g., the wall thickness.

The family of fatigue life design curves for welded aluminum chambers with various thicknesses and a radius of 3 m is shown in Fig. 3.6. Terminal points on the curves joined to vertical limits identify impulsive pressures which cause dynamic yielding. With a thickness of 3 cm and an impulse of 110 Pa-s (200 MJ) the number of permissible shots is 32,300 as compared with the design goal of 15,000. Corresponding calculations for 2.25 Cr-1 Mo and unwelded aluminum (at 110 Pa-s and 3 cm) show that all values are below the endurance limits.

The parametric lifetime data presented in UWFDM-656 indicates that the 15,000 shot design goal can be met with higher yields if the wall thickness is increased moderately. Alternatively, the desired number of 200 MJ shots can be sustained by a chamber with a smaller radius. Combinations of 200 MJ and higher yield shots are also possible.

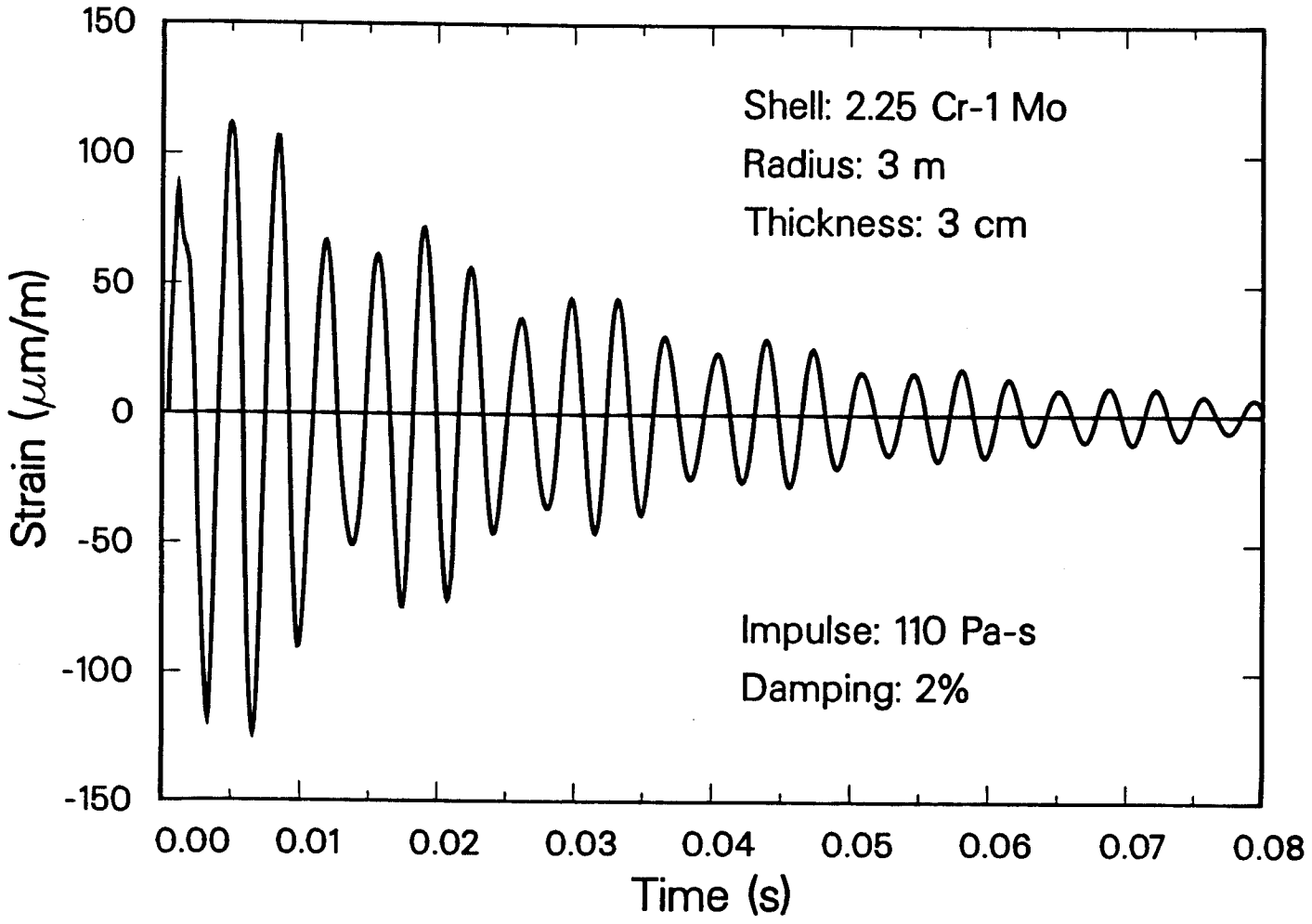

Fig. 3.4. TDF cylindrical shell circumferential mechanical strain.

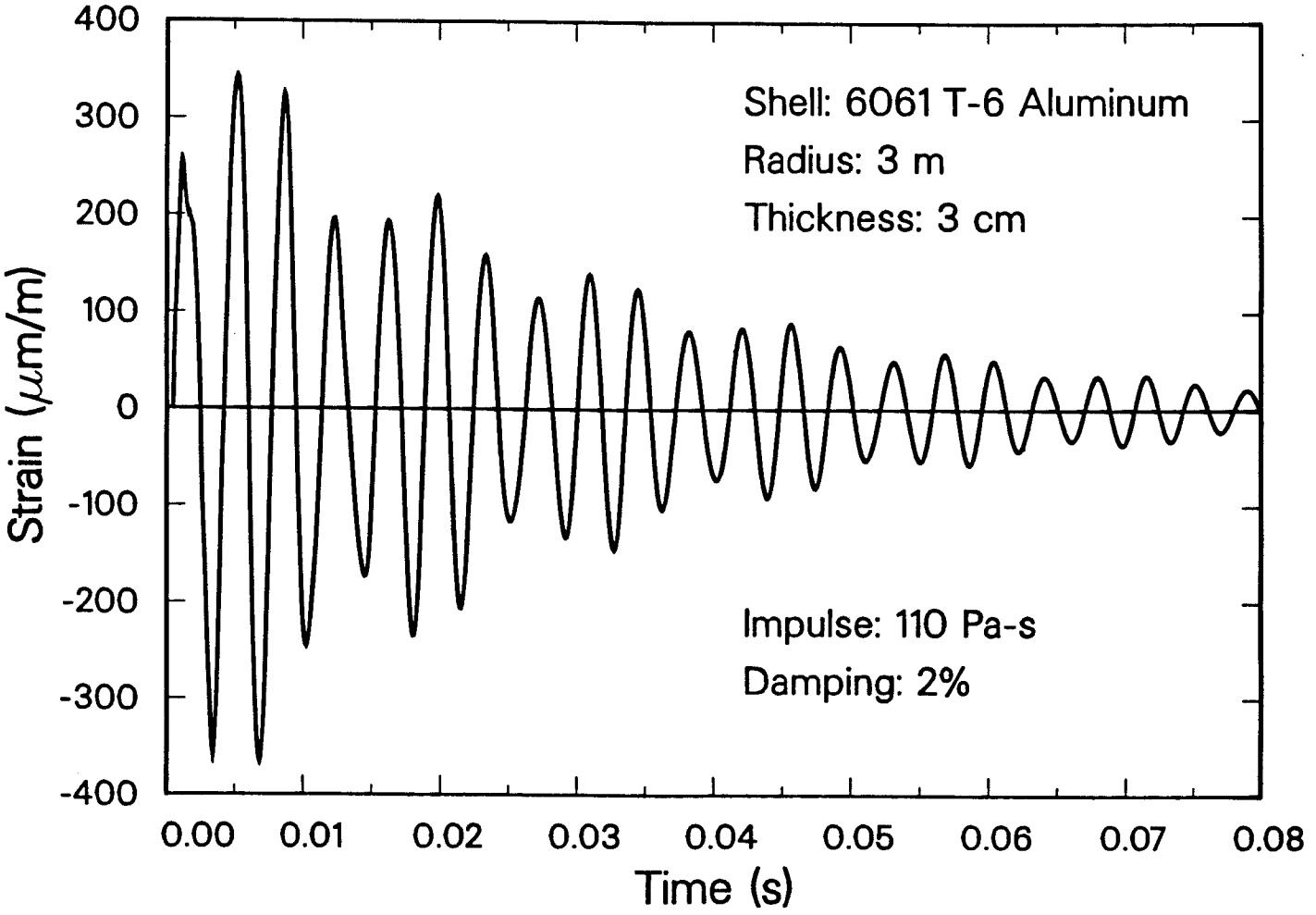

Fig. 3.5. TDF cylindrical shell circumferential mechanical strain.

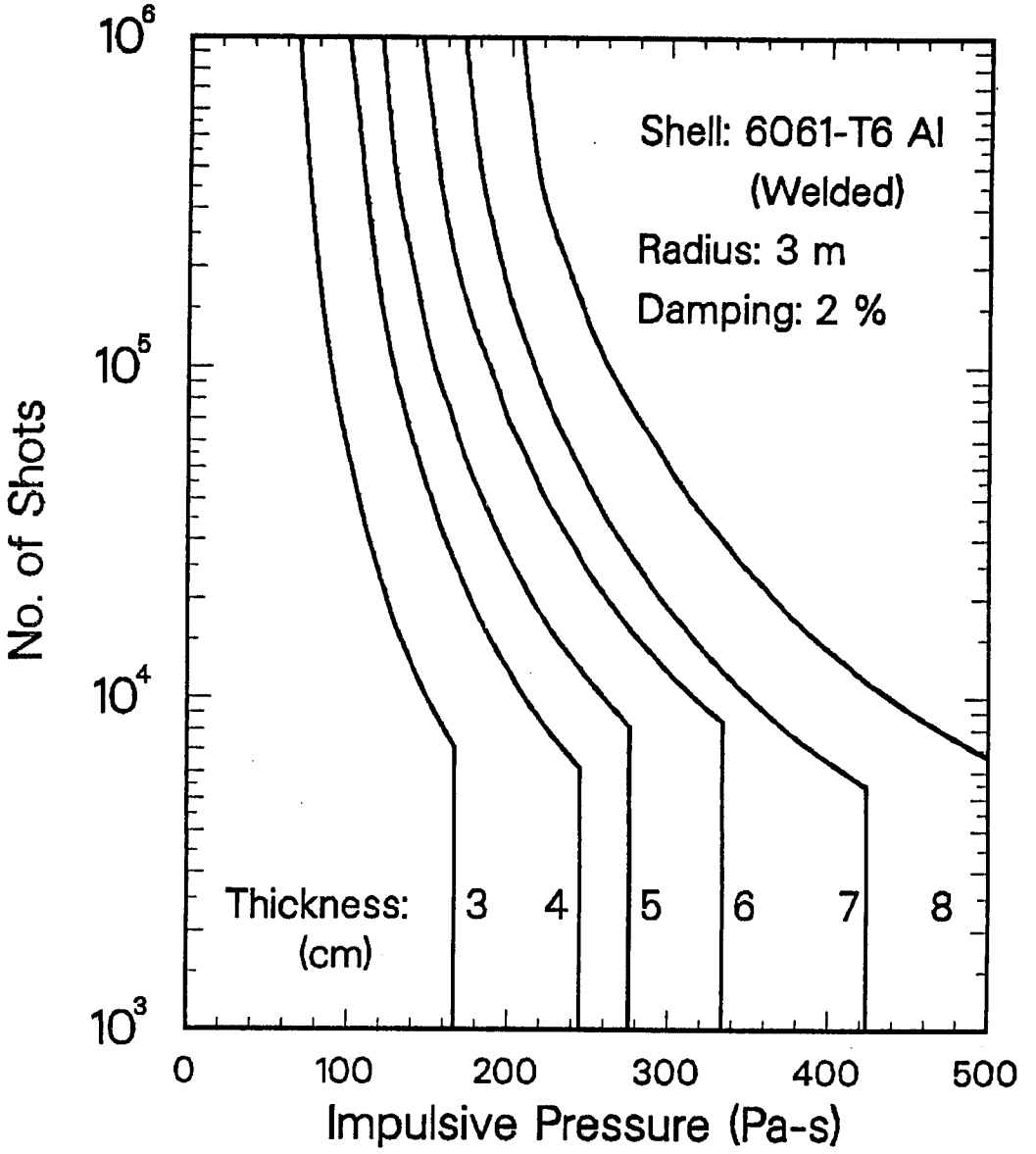

Fig. 3.6. Fatigue life of TDF cylindrical shell.

3.3 Spherical Chamber Analysis Summary

For sustaining completely symmetric internal pressure pulses, a spherical vessel is the optimum structural shape. Thus the mechanical response characteristics of spherical chambers have been studied to obtain the best case basis for performance comparisons with other configurations.

The model for the chamber is an elastic, relatively thin shell (radius/thickness > 50). The only displacement component is radial, i.e., the shell is always spherical and simply expands and contracts with time. A thin shell has a single natural frequency. A thick shell has multiple frequencies but for a moderate thickness, the fundamental frequency is much lower than any other and the contribution to stress and displacement from higher modes is negligible. Additional related information is contained in UWFDM-655.[2]

The spherical shell frequency (Hz) can be expressed by $\frac{[E/2\rho(1-\nu)]^{1/2}}{\pi a}$ in which E, ρ, ν and a denote the elastic modulus, density, Poisson's ratio and shell radius, respectively. From this it can be shown that for shells of interest, the vibration period is considerably larger than the pulse width of the corresponding mechanical shocks. The practical consequence of this is the representation of the loading by its impulsive value. This procedure is more accurate than using peak pressures and also more convenient for parametric studies in which the impulsive pressure is a single additional variable.

The corresponding maximum (undamped) circumferential normal stress is independent of chamber radius and is also essentially the same for steel or aluminum. The latter result is attributable to the dependence of stress on the modulus/density ratio. Typical values are shown in Fig. 3.7 for a chamber of 6061-T6 aluminum. The specific stress history of Fig. 3.8 corresponds to a 200 MJ yield in a 3 m chamber with a 3 cm thick wall. Maximum stress ampli-

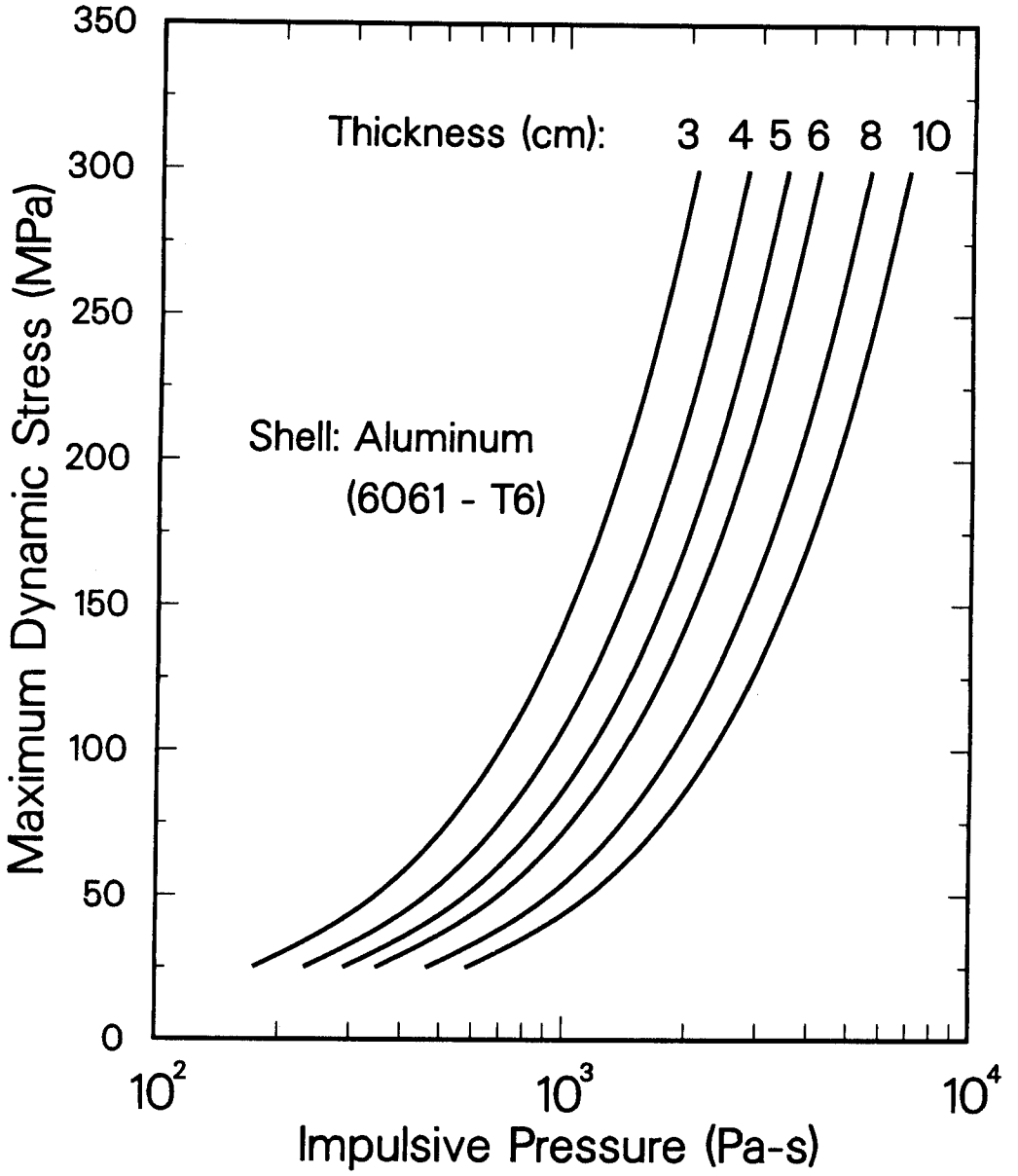

Fig. 3.7. Spherical shell mechanical stress from uniform impulsive pressure.

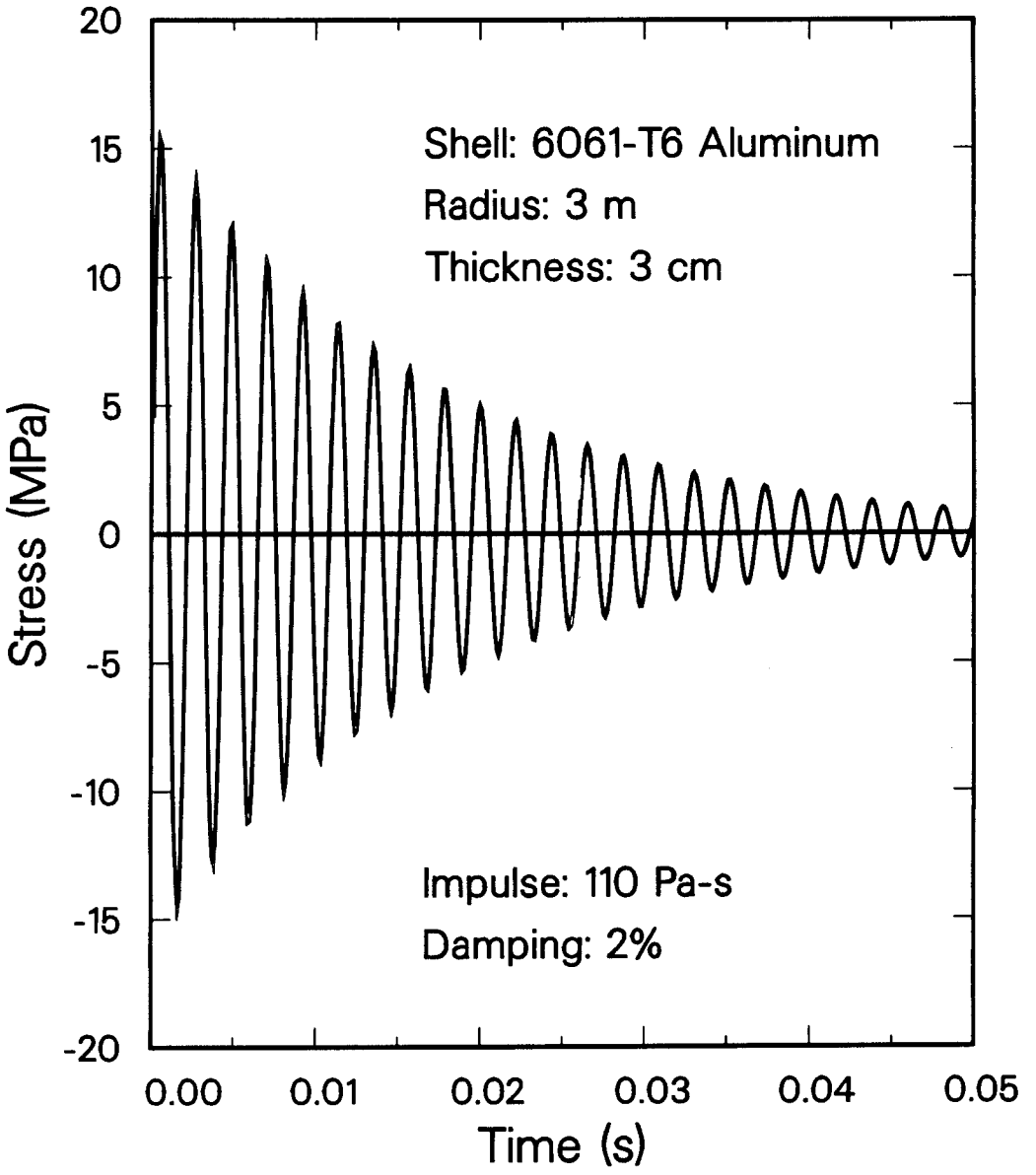

Fig. 3.8. Spherical shell mechanical stress history.

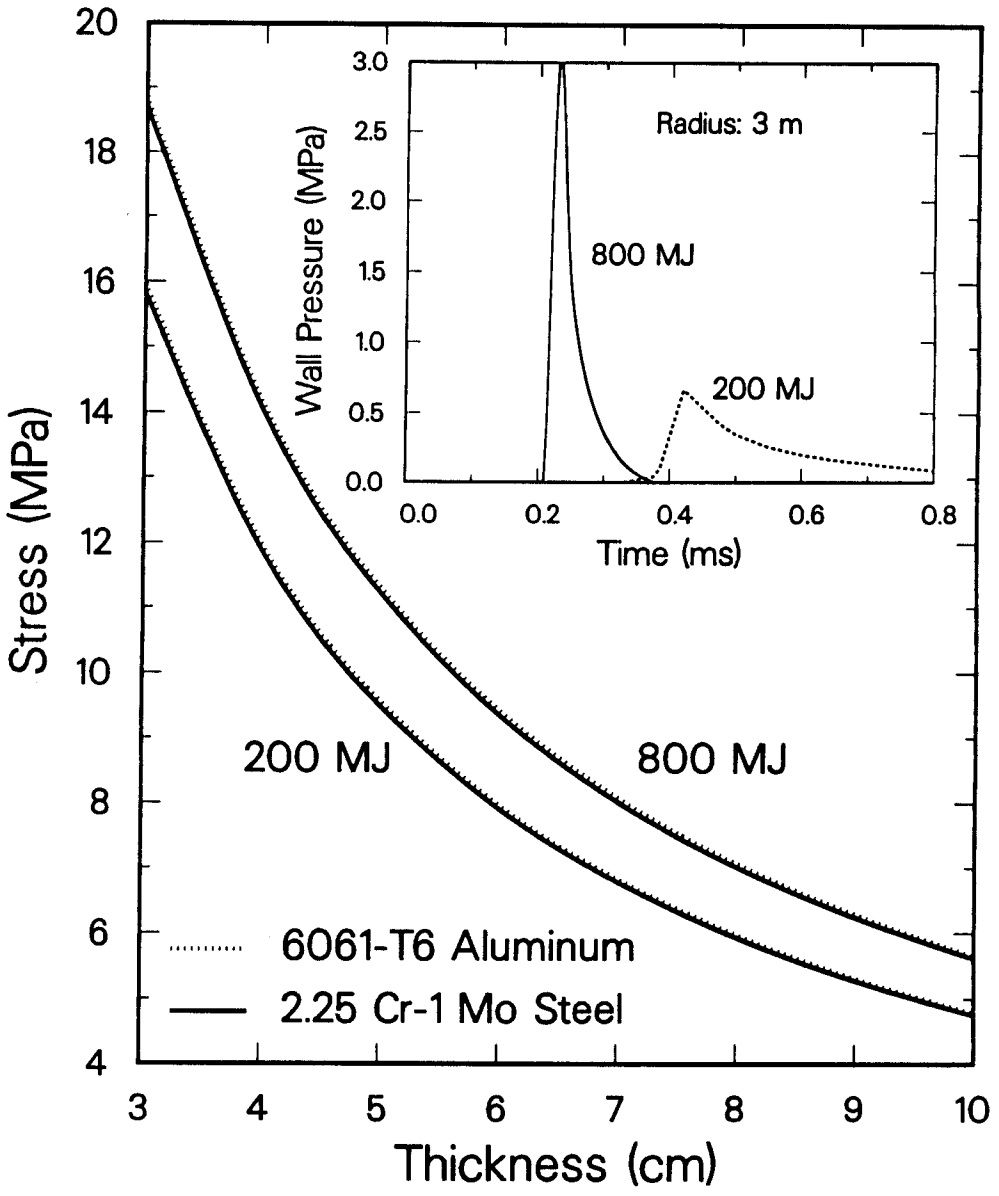

Fig. 3.9. Maximum dynamic stresses in spherical shells.

tudes are also compared in Fig. 3.9 for yields of 800 and 200 MJ in 3 m chambers for various thicknesses. It should be noted that while the peak pressures are quite different in these cases, the impulses are comparable. The near coincidence of results for aluminum and steel is also evident.

The maximum dynamic stresses for relevant spherical chamber sizes and yields are well below static and fatigue design limits, including welded aluminum plate.

3.4 Transmission Line Shock Isolation

The interface between the magnetically insulated transmission lines and the target chamber wall require some form of mechanical isolation to prevent shocks from being transmitted to the components of the transmission line. Requirements of such a coupling is that it be vacuum tight and be capable of compensating for minor component misalignments. Some sort of bellows immediately comes into mind.

The kind of bellows that seems to fit this application is a single convolution formed bellows referred to as an omega bellows due to its resemblance to the greek letter omega. Such a bellows shock isolation system is shown in Fig. 3.10. One of the limitations of such a bellows is that it can accommodate a very small displacement. In the case of TDF this is not a problem. Among its salient features is the fact that it can be adapted to many applications involving both high pressure and vacuum. Such bellows have been extensively used in rapid cycling bubble chambers both at liquid hydrogen temperature (20 K) and at room temperature. They have been manufactured in sizes up to 3 m in diameter by hydraulic forming and spin forming. Because such a bellows is not usually used to support a heavy load, we have assumed that the weight of the transmission line is supported separately. Alternatively, the protective sleeve shown in Fig. 3.10 can be used to support the

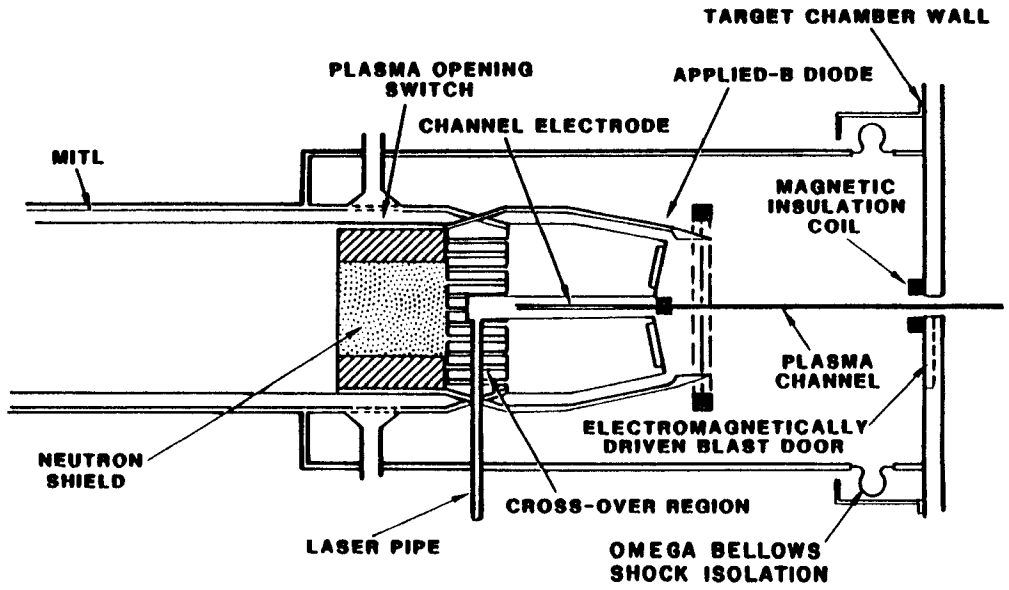

Fig. 3.10. Cutaway view of TDF MITL showing a shock isolating connection to the target chamber wall.

transmission line on the target chamber wall while still permitting shock isolation through the omega bellows.

An omega bellows is very versatile with respect to its adaptation to the required needs. The size of the convolution and the thickness of the bellows material determine the stress as a function of displacement, as well as the natural frequency. The convolution can also be inverted such that it faces inward rather than outward, as shown in Fig. 3.10. In some cases that may be the preferred configuration. The bellows can also be designed with a damper to provide shock absorption as well as isolation. All of these considerations will have to be evaluated before a final design for shock isolation in TDF can be arrived at.

References for Chapter 3

1. R.L. Engelstad and E.G. Lovell, "Parametric Lifetime Analysis of Cylindrical Chambers for the Target Development Facility," University of Wisconsin Fusion Technology Institute Report UWFDM-656, October 1985.

2. R.L. Engelstad and E.G. Lovell, "Dynamic Response of Target Development Facility Spherical Chambers," University of Wisconsin Fusion Technology Institute Report UWFDM-655, October 1985.

4. Plasma Channel Design and Analysis

Plasma channels in the TDF Target Chamber will guide the eight ion beams from the diodes to the target. A gas of molecular nitrogen (N_2) will fill the target chamber at a density of 9.63×10^{17} cm^{-3} and will act as a medium for the channels. Lasers will preionize the gas to the point that it will break down along preferred directions. Banks of capacitors will be discharged through the channels to drive an electron current that will heat and rarefy the channels and will create several kilogauss magnetic fields to confine the beam ions. At an optimal time in the development of the channels, the ion diodes will inject a pulse of ions into each channel. These are lithium ions, with an average energy of 30 MeV. At injection, each ion beam will have a maximum current of 1.25 MA and a main pulse width of 30 ns with a 100 ns long prepulse. This current history is shown in Fig. 4.1. As the beams move toward the target, they increase their instantaneous currents due to bunching induced by voltage ramping at the diode. At the target, their currents and thus their powers, have doubled. The current per channel at the target is shown in Fig. 4.2, where the maximum is 2.5 MA and the main pulse has a width of 15 ns. Thus, the eight channels direct a total pulse of 9 MJ into the region surrounding the target at a maximum power of 600 TW.

We have reported on three aspects of the plasma channels: the formation and behavior of channels before and during the injection of the ion beams, the interaction of plasma channels with neighboring channels, and the effect of an externally applied magnetic field on the channel behavior, where the magnetic field is meant to prevent breakdown between the channel and the TDF target chamber vessel. Each of these items are discussed in the following sections.

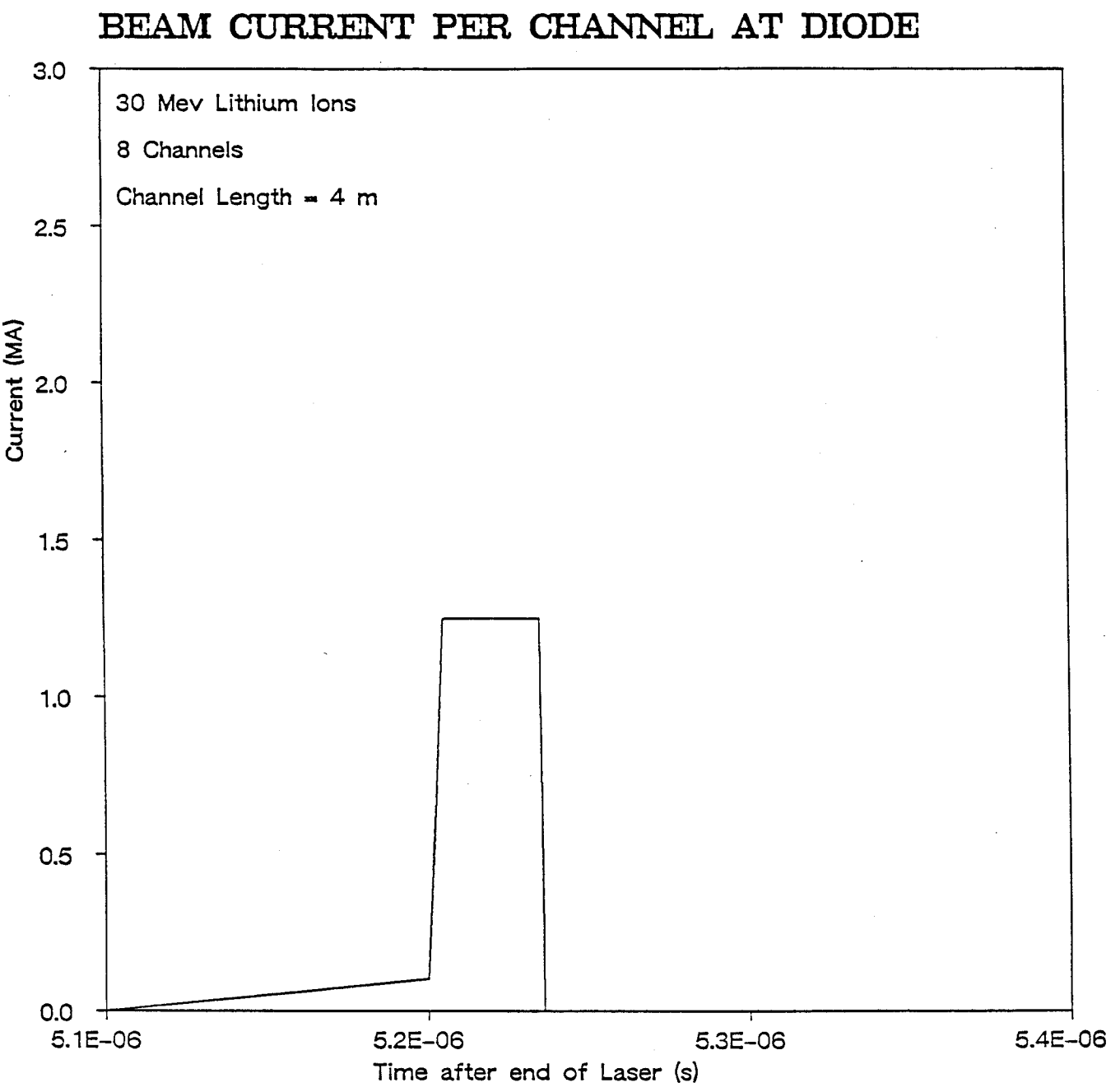

Fig. 4.1. TDF ion current in each channel near the diode.

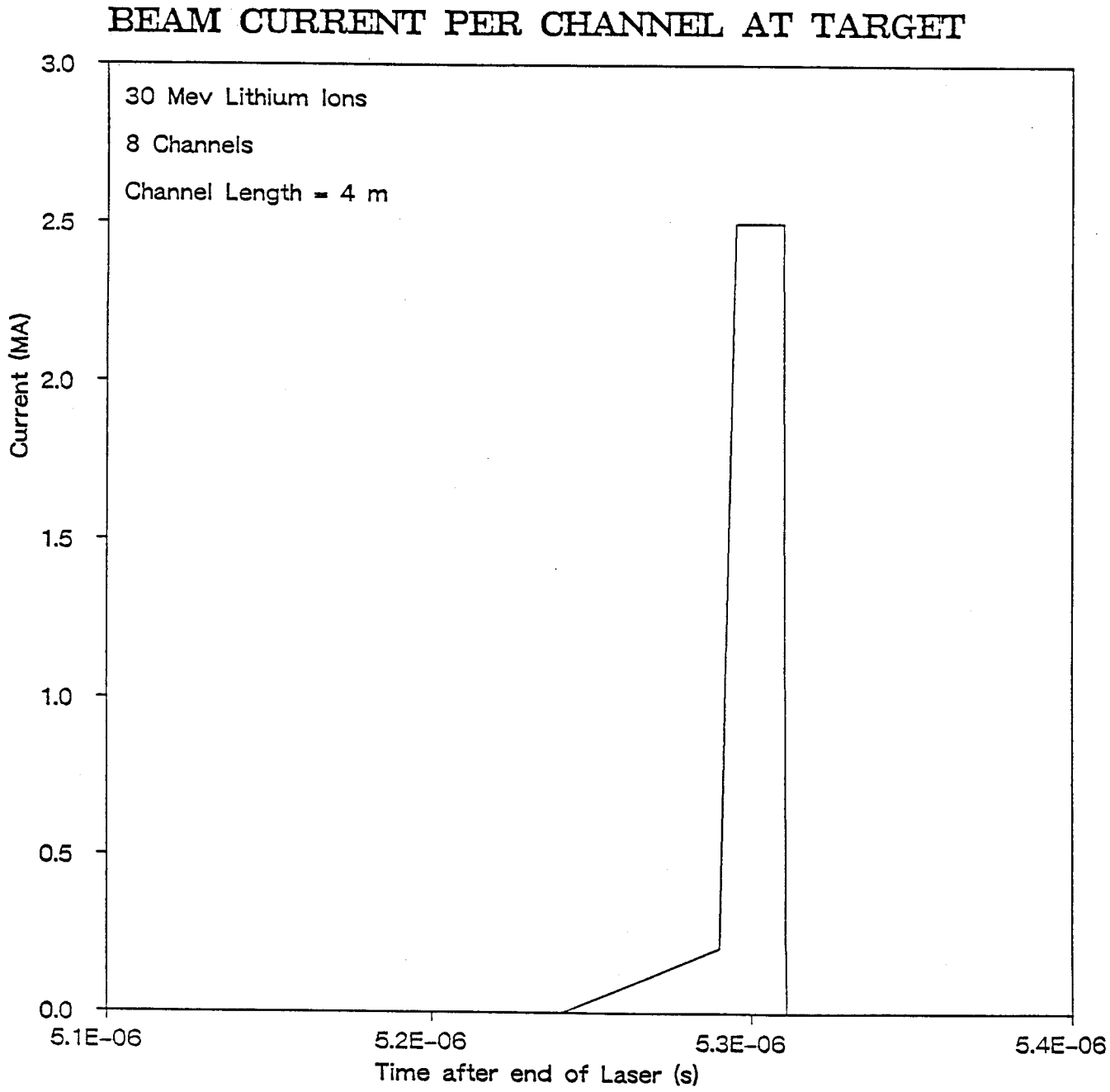

Fig. 4.2. TDF ion current in each channel near the target.

4.1 Channel Behavior

We have studied the radial behavior of plasma channels with a one-dimensional Lagrangian magnetohydrodynamics multigroup radiative heat transfer computer code with discharge current flow, ion beam heating, and magnetic field generation and diffusion.[1] This code is called Z-PINCH. The channels are to be formed in a N_2 background gas. A laser guides the channel formation by providing an increased temperature along the axis of the channel. The initial temperature profile is 0.78 eV at the center of the channel and has a full width at half maximum of 0.8 cm. The initial gas density is uniformly 9.6×10^{17} cm^{-3}. We have assumed that the channel is 4 meters long.

Starting from these initial conditions, we have investigated the formation of the plasma channels under the the influence of the two discharge current profiles shown in Figs. 4.3 and 4.4. The parameters of the circuit used to drive the discharge current are the voltage drop across the channel, the capacitance of the capacitor bank that is discharged to create the current and the inductance of the channel. A symbolic circuit diagram of the discharge circuit is shown in Fig. 4.5. The current profile shown in Fig. 4.3 is close to the form of the current used in an earlier study[2] and we have used it as a reference case. To get this profile, we use two circuits: one to drive the prepulse and one to drive the main pulse. The two circuits require inductances of 1.216 μH and 0.135 μH, capacitances of 0.9 μF and discharge voltages of 2.12 kV and 20 kV for the early and late pulses respectively. There are certain physical realities that disallow some of these values. Using experimental values for breakdown voltages for N_2 as a function of the product of the gas density and length of the breakdown $(nd)^3$ and using a value for nd of 1.92×10^{20} cm^{-2}, one finds a breakdown voltage of 182 kV. Since one only

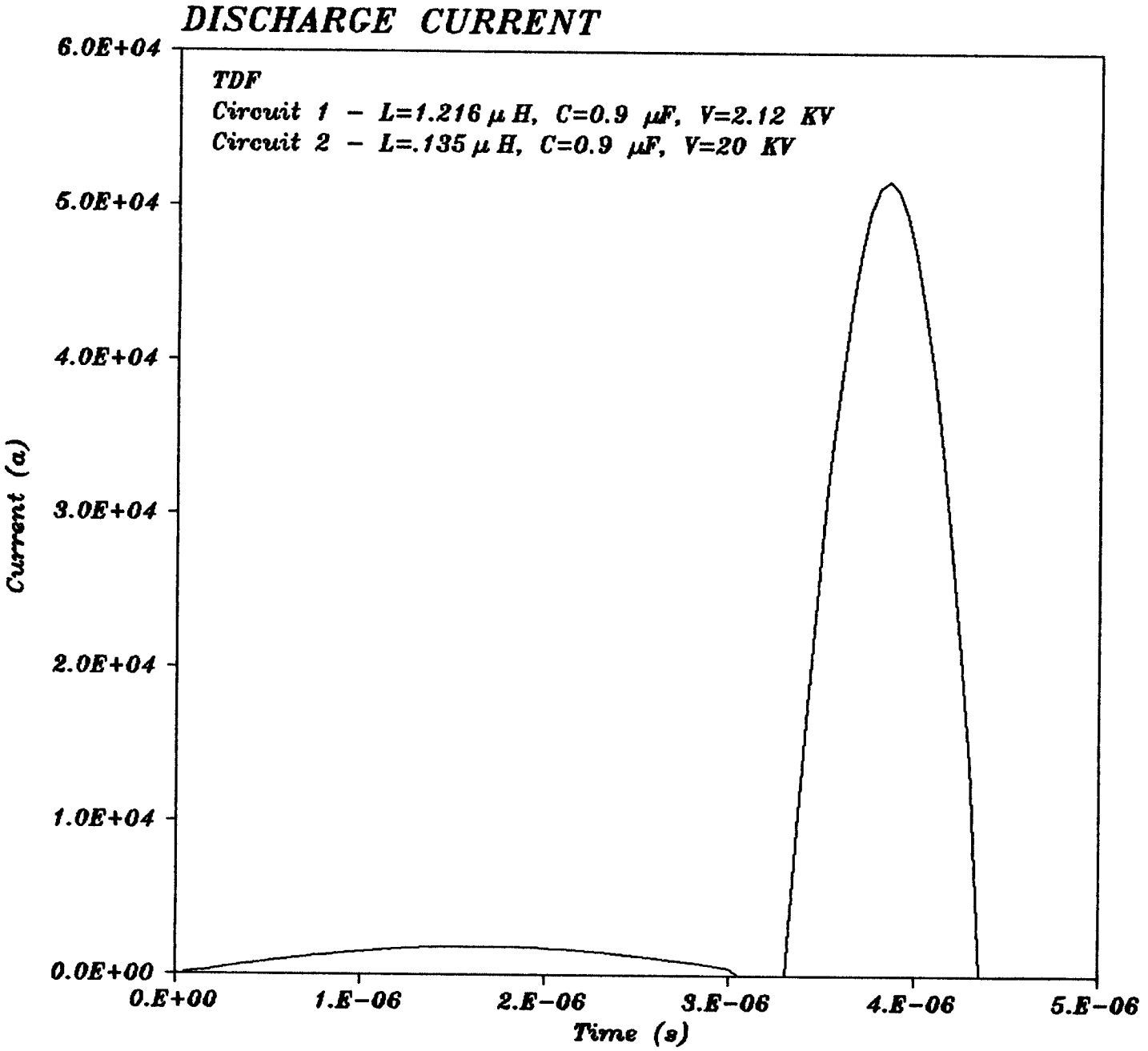

Fig. 4.3. Discharge current in each channel where a low channel inductance is allowed.

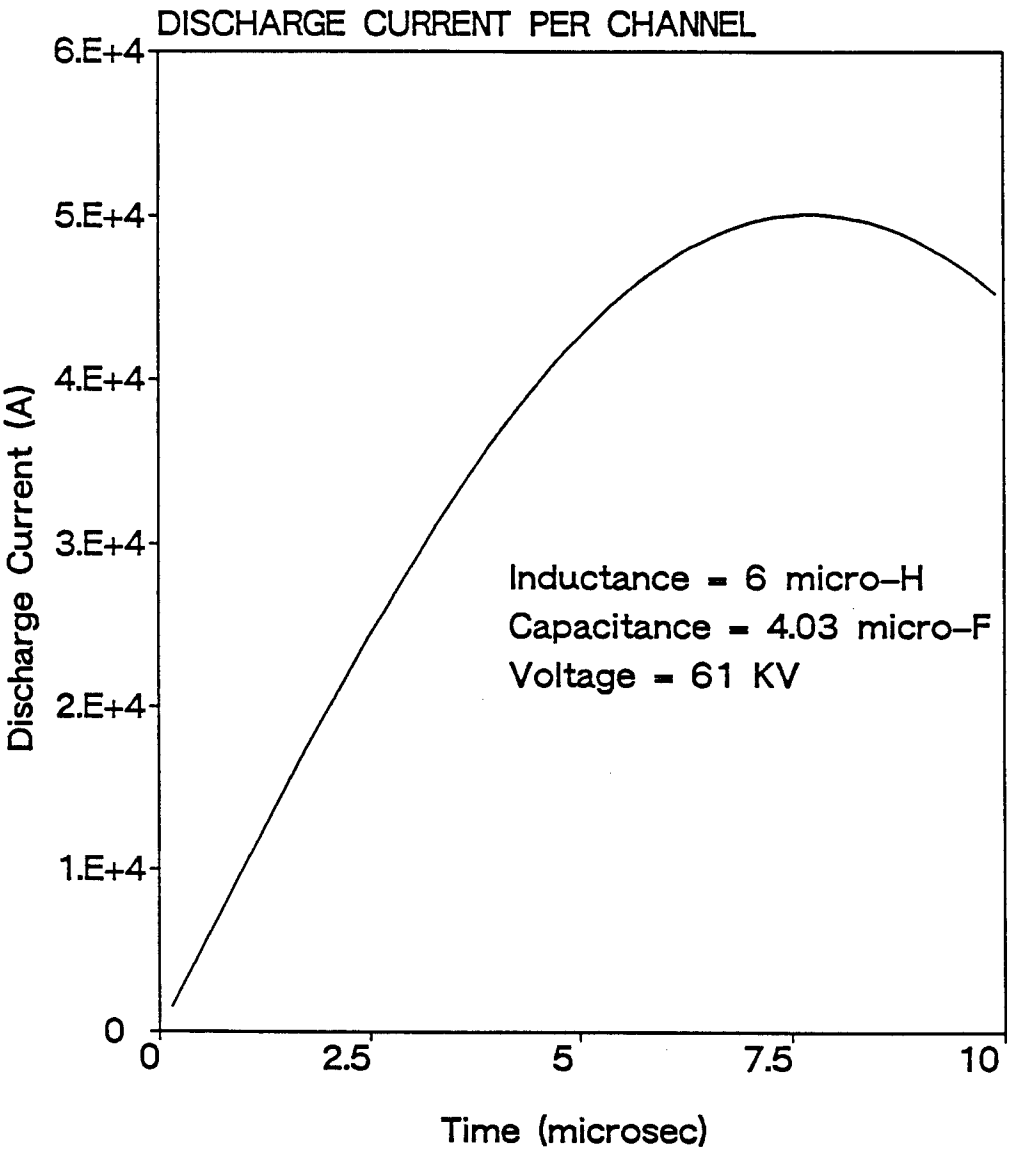

Fig. 4.4. Discharge current in each channel where a realistic channel inductance is demanded.

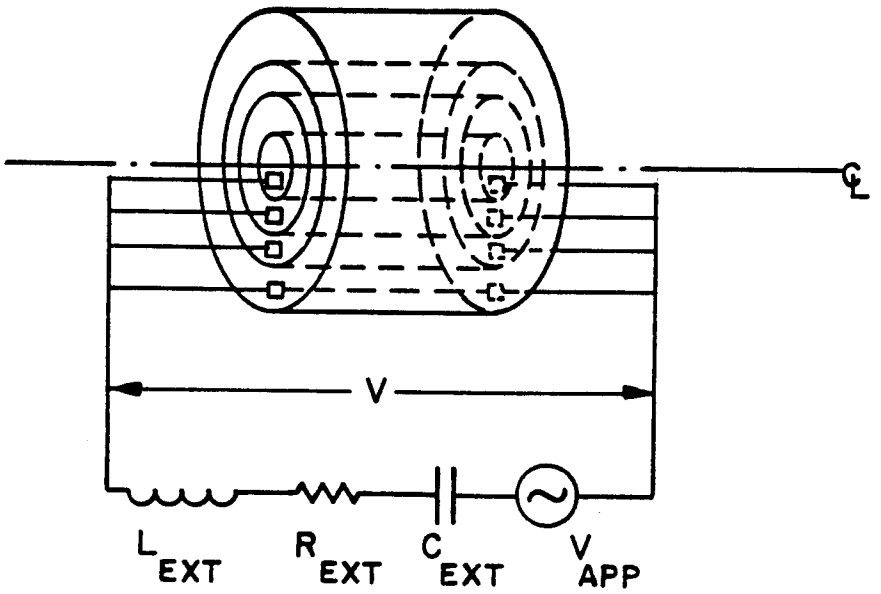

Fig. 4.5. Symbolic discharge circuit.

wants to break down along the path of laser preionization, a discharge voltage of one third of the breakdown voltage, or 61 kV, should be used. The channel is the dominant inductance in the discharge circuit and a value of 1.5 μH per meter of channel seems to be a minimum estimate. Thus, for a 4 meter long channel, a value of 6 μH for the circuit is reasonable if one neglects other inductances outside the channels. These two values, with the requirement of a maximum discharge current of 50 kA, lead to a capacitance of 4.03 μF for the circuit. This circuit will create the much more slowly rising current profile shown in Fig. 4.4.

The ZPINCH computer code has been used to simulate the behavior of plasma channels with the two previously discussed discharge current profiles. The "fast" discharge current in Fig. 4.3 causes the channel to behave as shown in Figs. 4.6 through 4.9. The mass density of the channel is shown in Fig 4.6, plotted against distance from the centerline of the channel for various times. One sees that the gas is swept out to a radius of about 1 cm in a few μs and that the density in the channel center drops by a factor of 3 or 4. The gas temperatures, shown in Fig. 4.7, increases substantially over the same time scale. The discharge current heats up the center and radiative heat transfer heats the gas outside the channel. This heating of the gas outside the channel causes the spreading region of reduced resistivity pictured in Fig. 4.8. By 4.3 μs after the start of the discharge the low resistivity has spread to 2.7 cm from the channel center. This allows the discharge current to spread out and causes ohmic heating of these outer regions. Because the discharge current has spread out, the azimuthal magnetic field that is generated by this current, is less concentrated and has a reduced amplitude. This is shown in Fig. 4.9, where the magnetic field is seen to have a local maximum

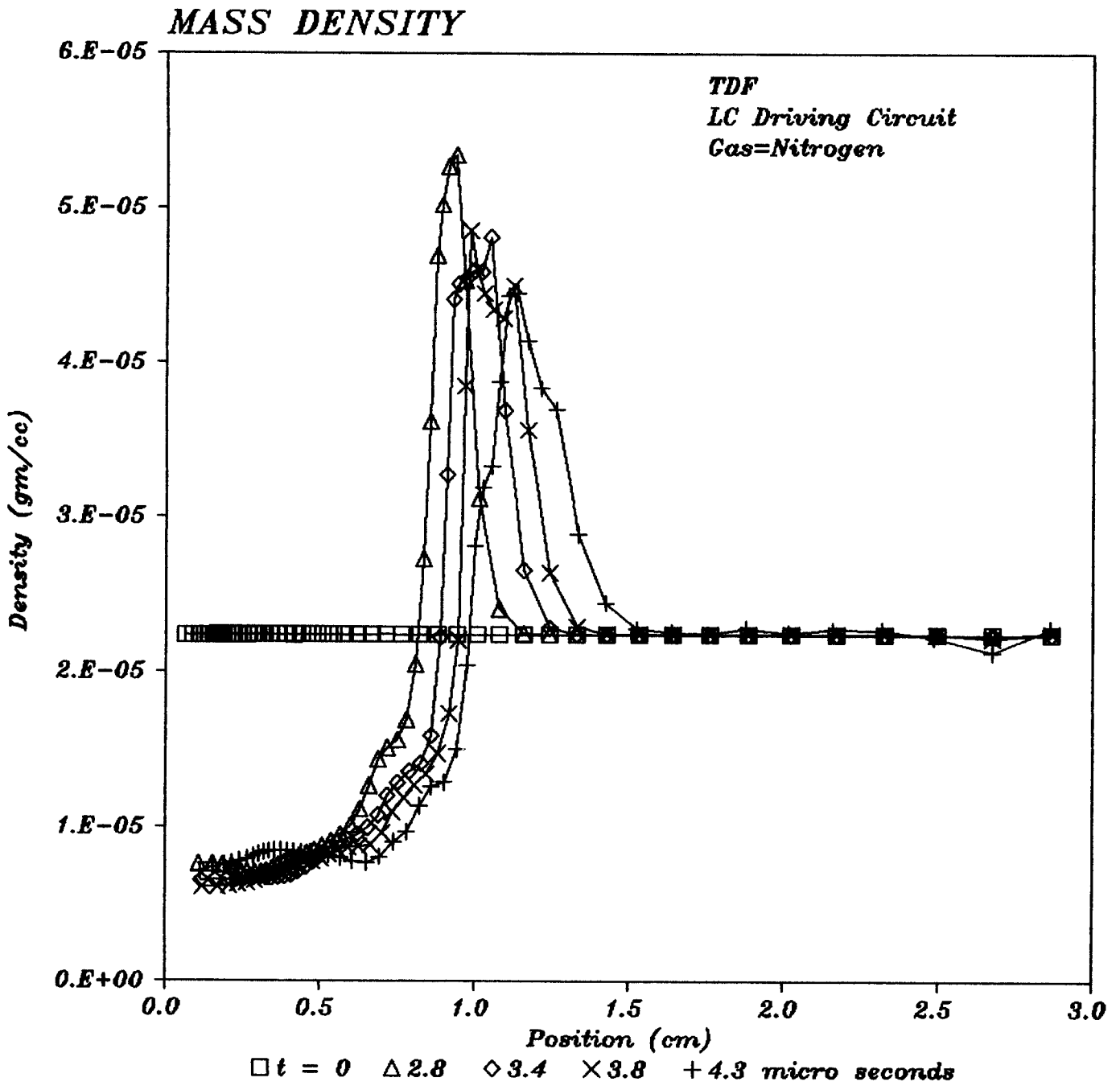

Fig. 4.6. Radial mass density profile for fast discharge current in N_2.

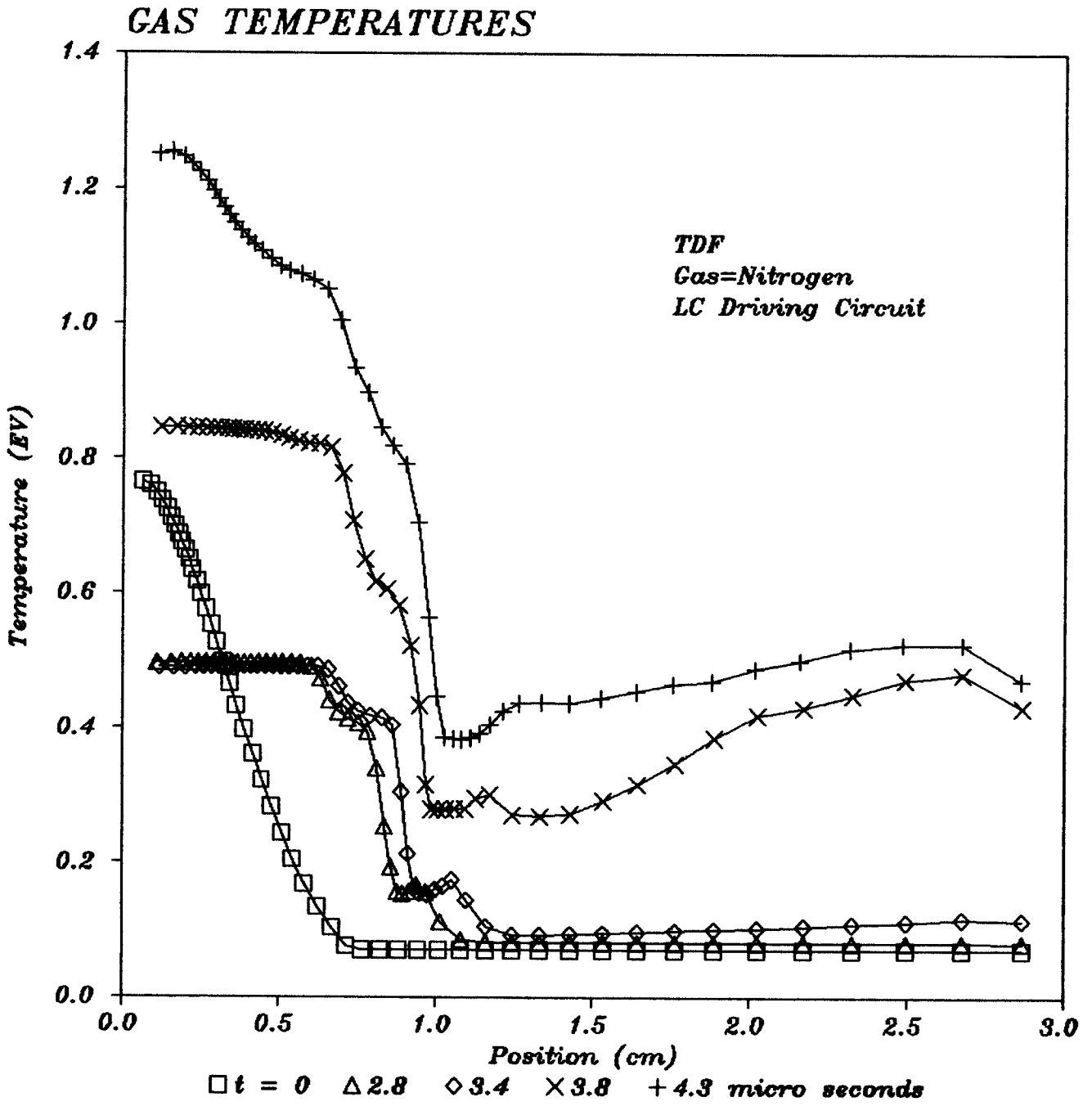

Fig. 4.7. Radial temperature profile for fast discharge current in N_2.

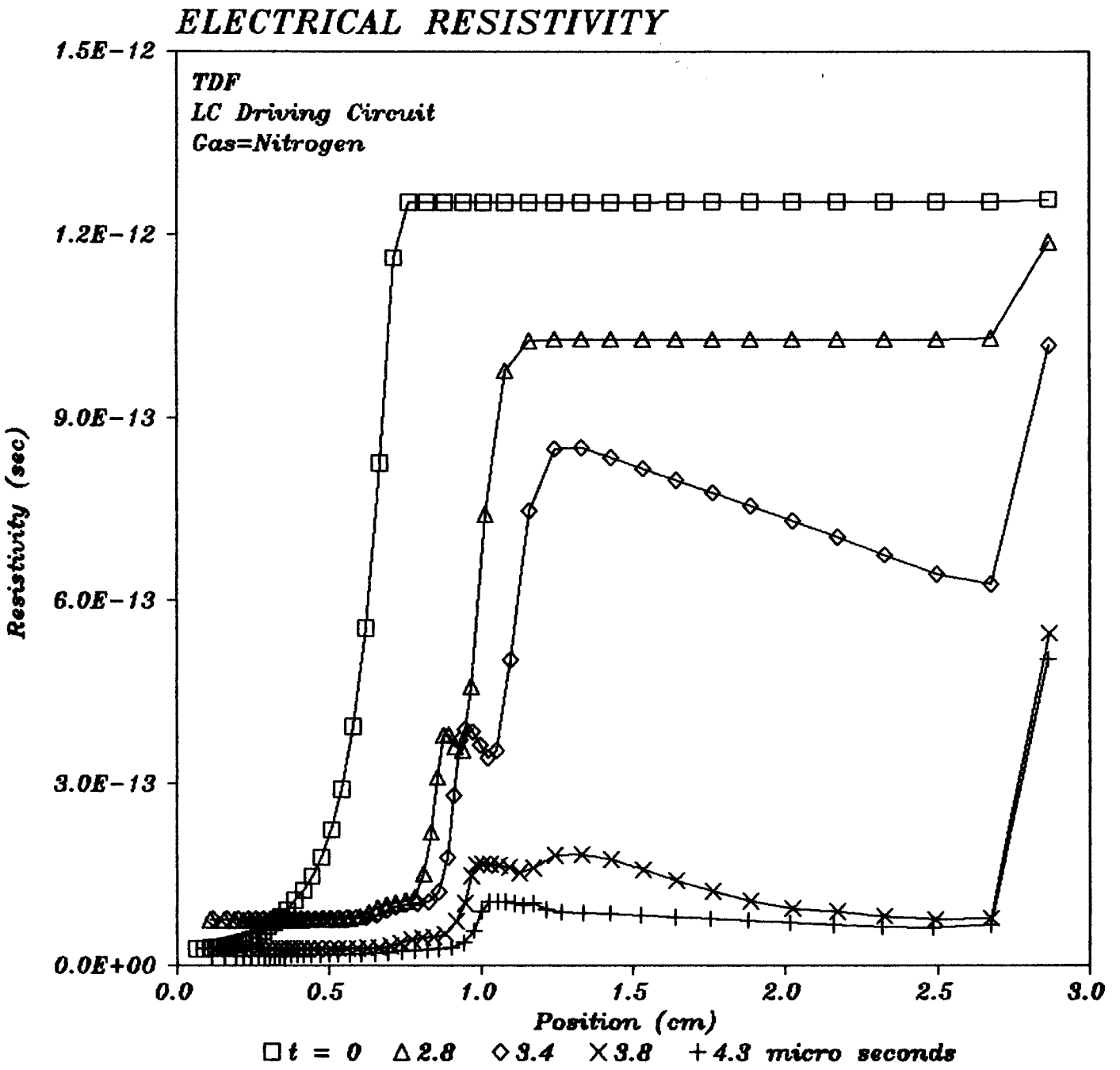

Fig. 4.8. Radial electrical resistivity profile for fast discharge current in N_2.

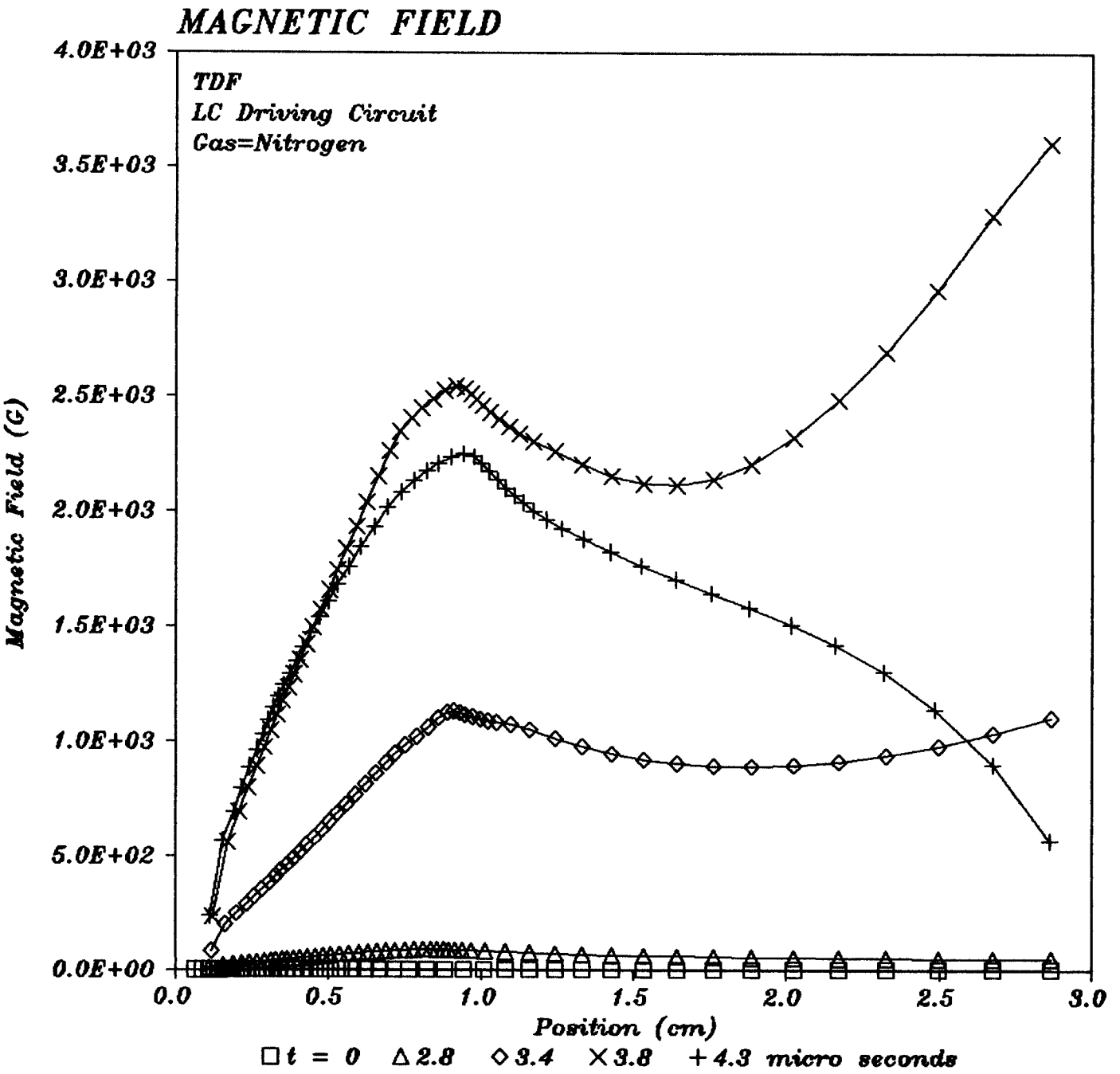

Fig. 4.9. Radial profile of the azimuthal magnetic field for fast discharge current in N_2.

at about 1 cm but a tendency to increase again at large radius. As we will now see, these results are somewhat more optimistic than those for the more realistic discharge current profile.

ZPINCH has been used to simulate the behavior of a channel under the influence of the "slow" discharge current of Fig. 4.4. The mass density, gas temperature, electrical resistivity, and azimuthal magnetic field plotted against radial position and time are shown respectively in Figs. 4.10, 4.11, 4.12, and 4.13. One sees for this case a mass density near the channel center that is less reduced than in the previous case, though the reduced density region still extends out to about 1 cm. The maximum mass densities are lower and the density peaks are more spread out because the current rise is slower. The gas temperature profiles are similar for the two cases as are the electrical resistivities. The magnetic field profiles are somewhat like those of the "fast" discharge, in that they have local maxima about 1 cm from the channel center and the increasing fields at large radii that imply significant discharge current densities outside the channel. The very different time dependence of the discharge currents naturally lead to changes in the details of the magnetic field profiles. The local maximum fields at 1 cm from the center are between 2.5 and 3.0 kG for both "slow" and "fast" discharges. Of course, the time at which one achieves the maximum magnetic field in the proper location is much later in the "slow" discharge. Therefore, the important differences between channels created by "slow" and "fast" discharges are in the density in the center of the channel and time scale for formation of the channel. The next important question is how efficiently can ions propagate through such channels to the target.

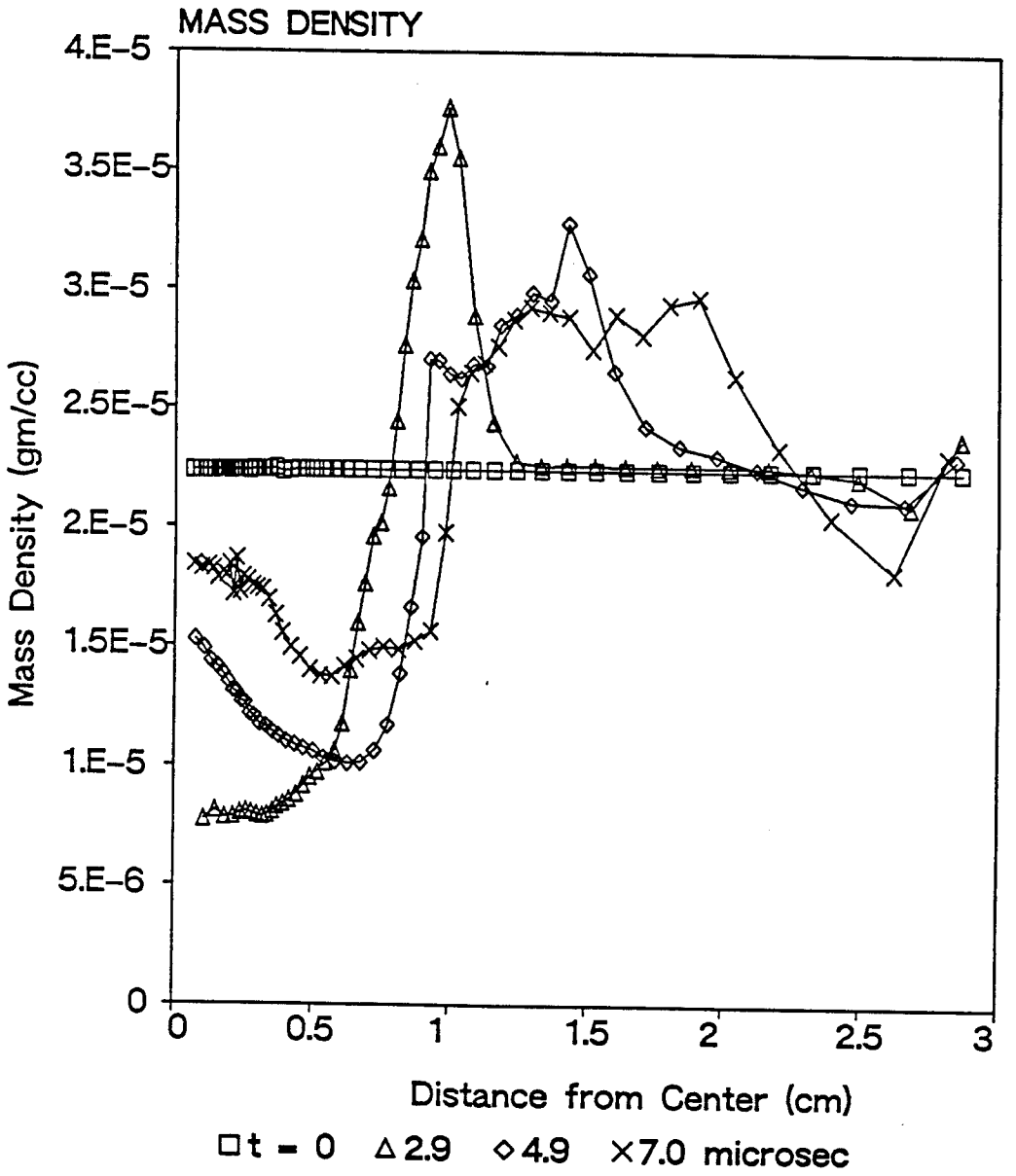

Fig. 4.10. Radial mass density profile for slow discharge current in N_2.

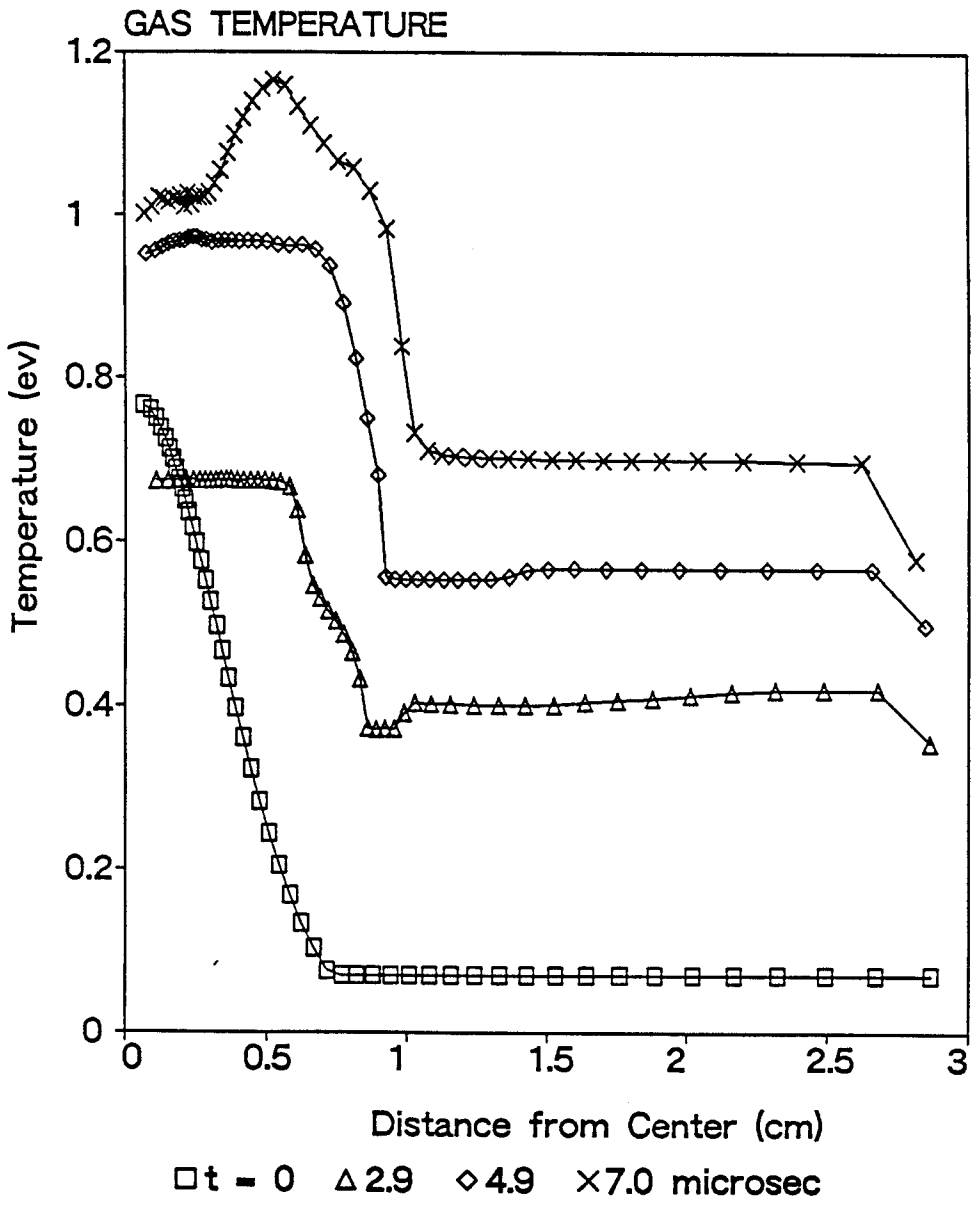

Fig. 4.11. Radial temperature profile for slow discharge current in N_2.

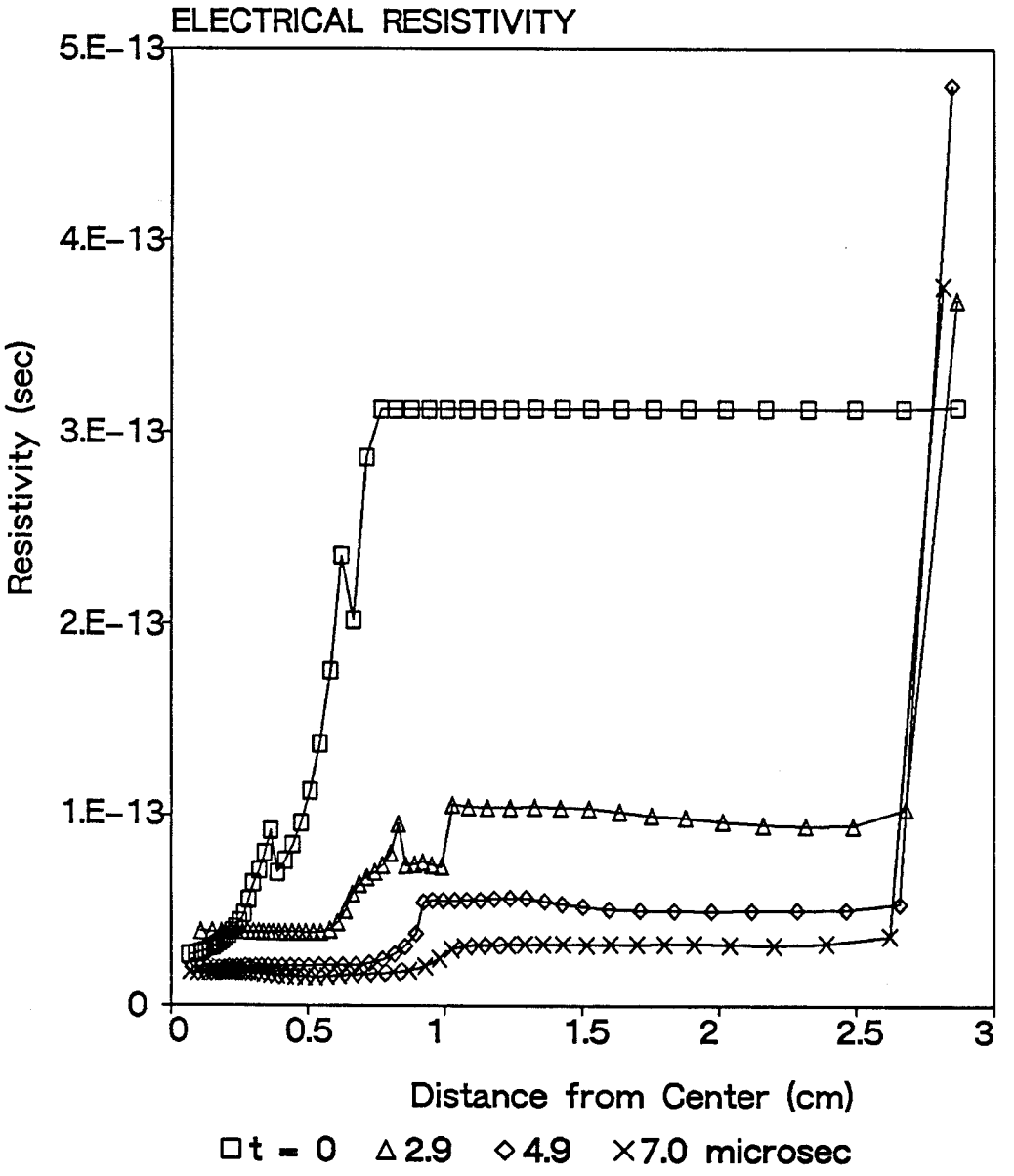

Fig. 4.12. Radial electrical resistivity profile for slow discharge current in N_2.

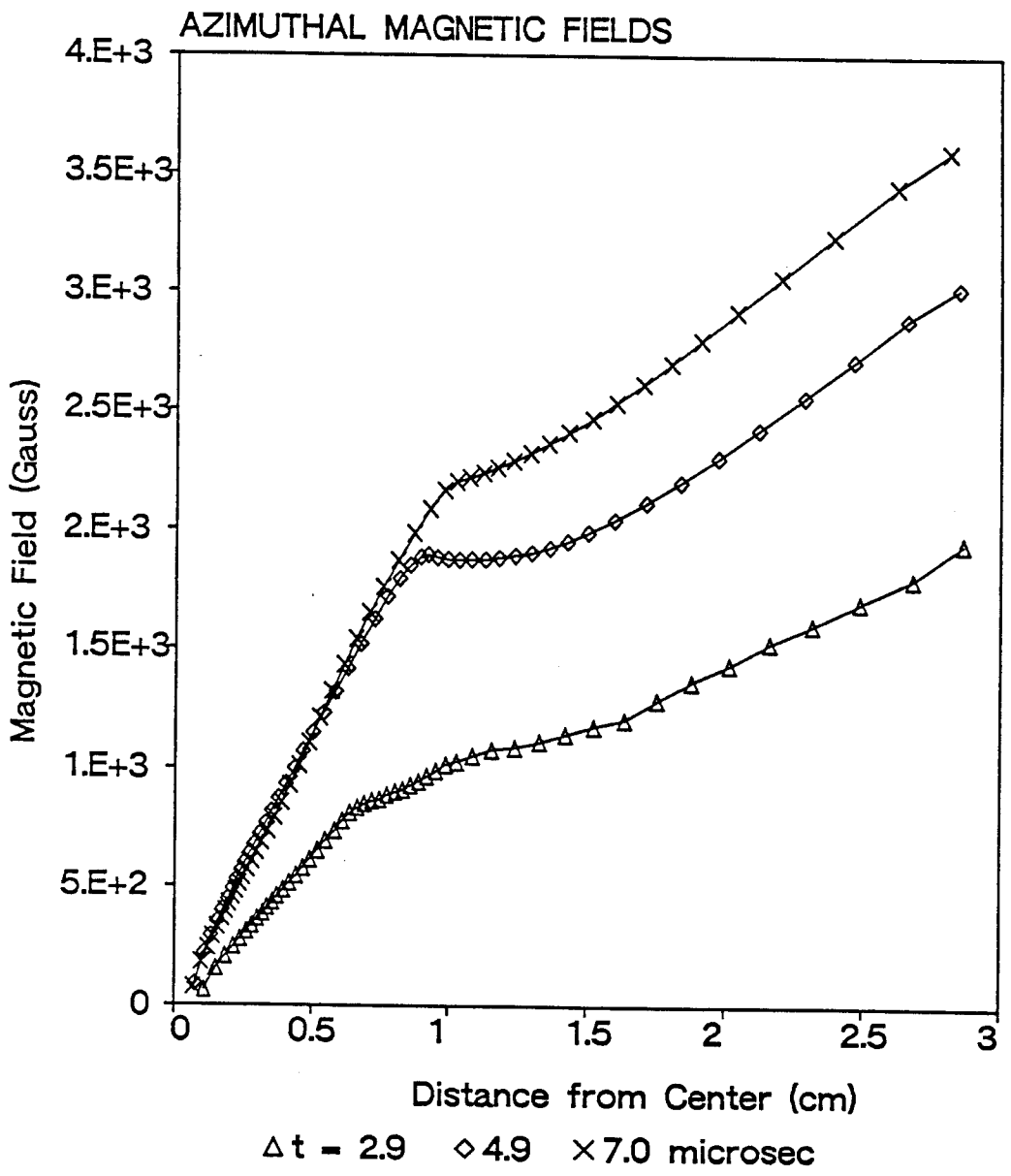

Fig. 4.13. Radial profile of the azimuthal magnetic field for slow discharge current in N_2.

Three aspects of ion propagation have been studied: the effects that are seen in the channel behavior due to the presence of the ion beam, the radial confinement of the ions by the azimuthal magnetic fields, and the limits on the ion current and thus the ion power due to plasma instabilities and energy losses to the ions. The behavior of the plasma channels is once again studied with the the ZPINCH computer code. The "slow" discharge current of Fig. 4.4 is used and the particle current of 30 MeV lithium ions near the diode, seen in Fig. 4.1, is assumed. The radial mass density profile in Fig. 4.14 shows that the ion beam causes a great rarefaction of the channel center. In this case the ion beam was assumed to have a Gaussian radius of 0.5 cm, which is the width of the rarefied region 1.3 μs after the start of the main ion pulse. This rapid outward movement causes a v x B force on the ions that is a major contributor to their energy loss in the channel. The gas temperature of the center of the channel is shown as a function of time in Fig. 4.15 for ion beam Gaussian widths of 1 and 2 cm (Gaussian radii of 0.5 and 1 cm, respectively). For the 0.5 cm radius beam the maximum temperature is 32 eV, while it is 20 eV for the wider beam. The trajectories of 30 MeV lithium ions in the "slow" discharge channel have been calculated and are shown in Fig. 4.16 for the case of a focal spot Gaussian radius of 0.15 cm at the entrance to the channel and a maximum injection angle of 0.075 radians. The average radius of the beam in the channel is much larger than the focal spot. For this case 21 out of the 25 trajectories calculated were confined. Results of other combinations of injection angles and spot sizes are given in Table 4.1. The window of beam propagation in ion beam injection angle versus ion beam power space is shown in Fig. 4.17. This result comes from the WINDOW computer code[4] that is based on models developed at NRL.[5] The window of propagation is that region

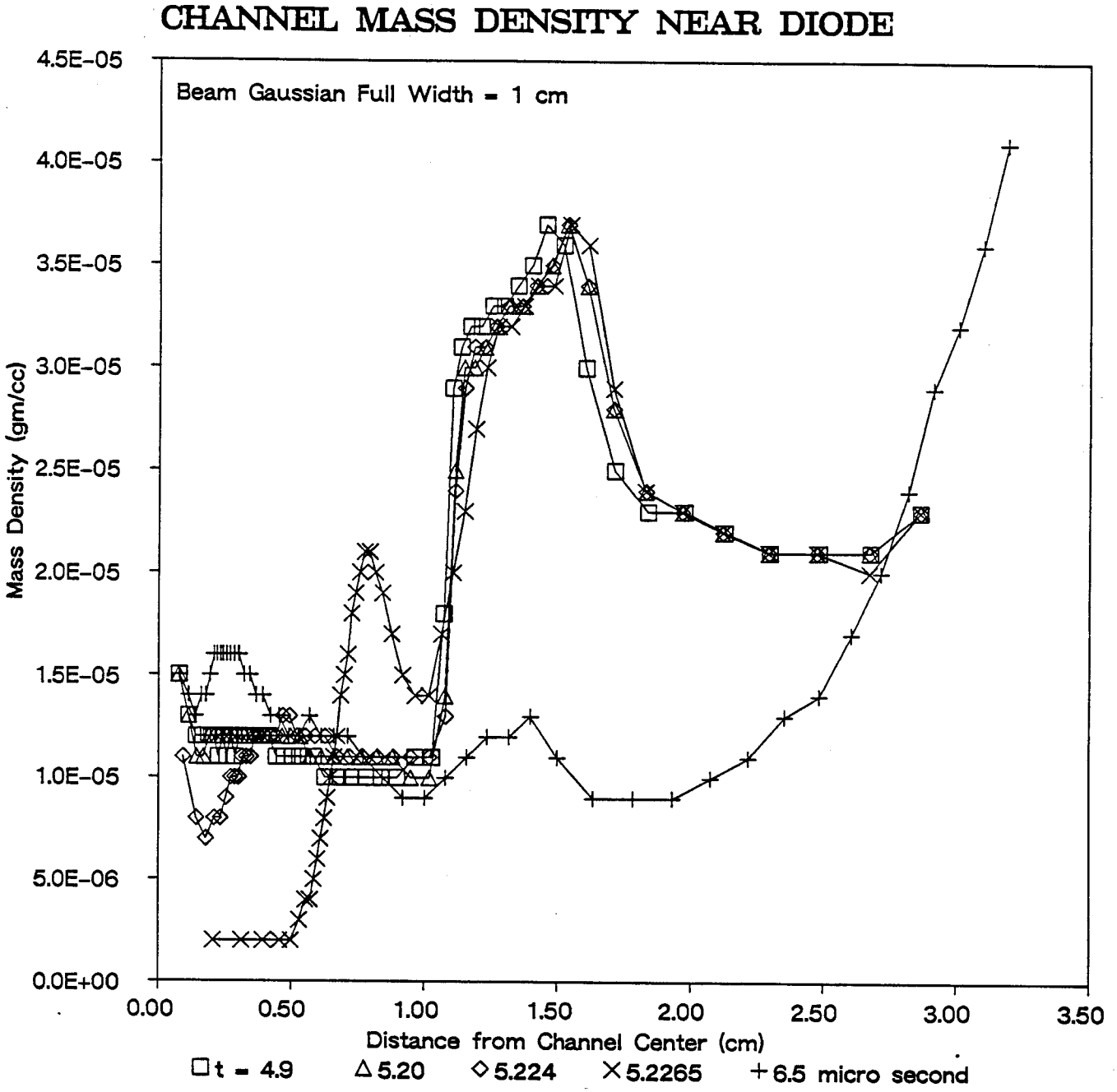

Fig. 4.14. Mass density profile in the presence of an ion beam near to the diode.

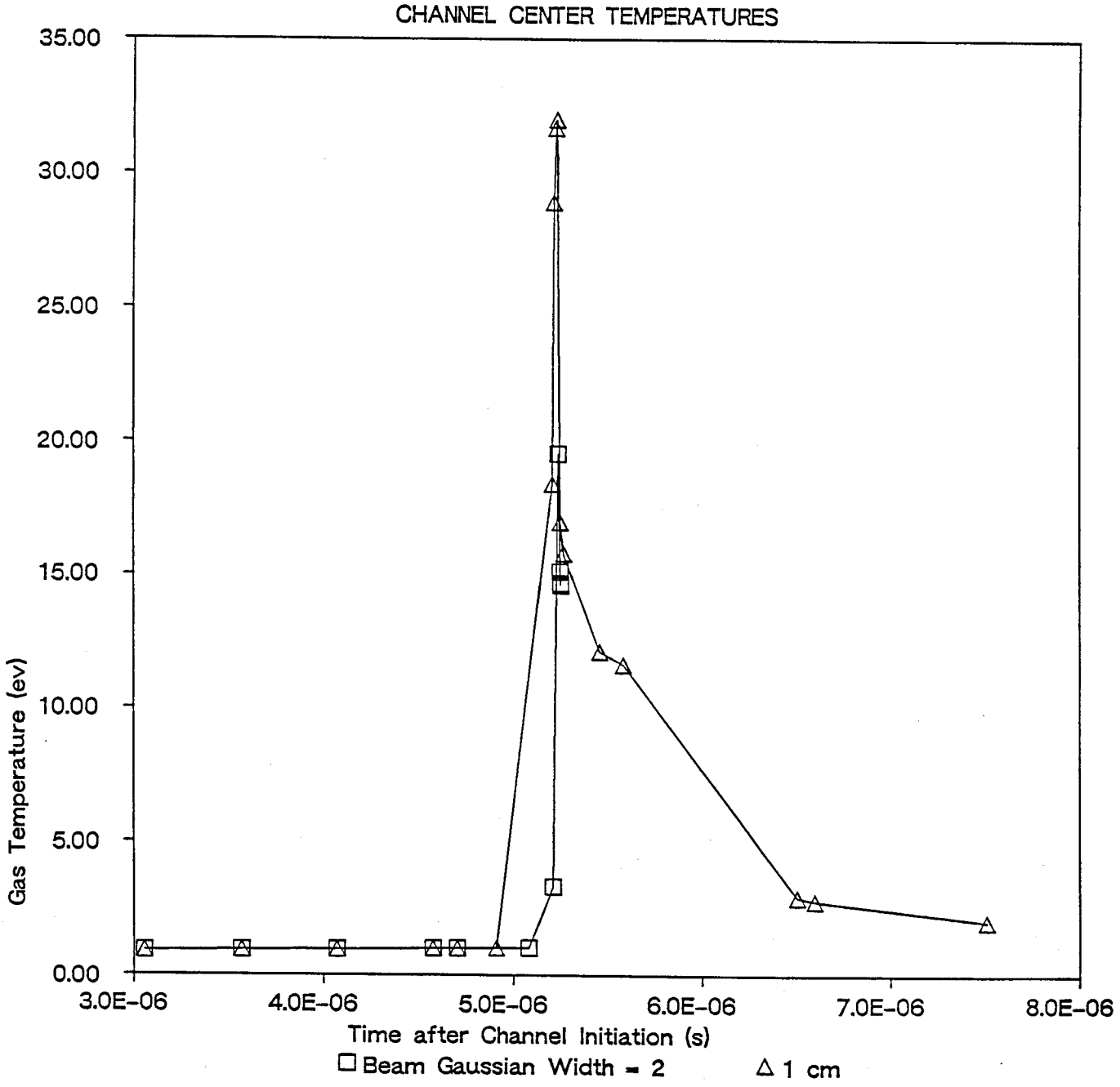

Fig. 4.15. Central gas temperature of the channel in the presence of an ion beam near to the diode.

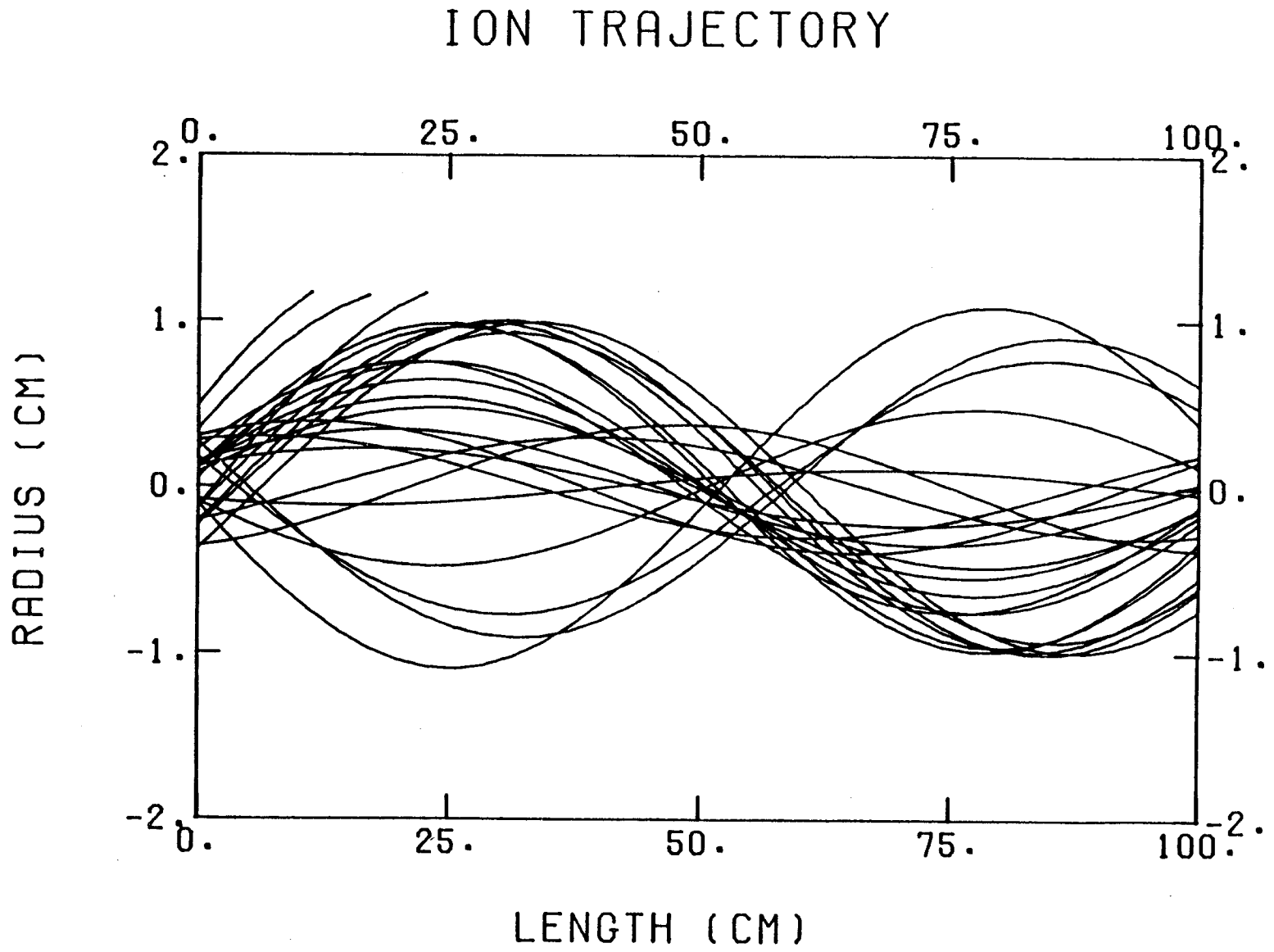

Fig. 4.16. Trajectories of 30 MeV lithium ions in a channel formed with a "slow" discharge.

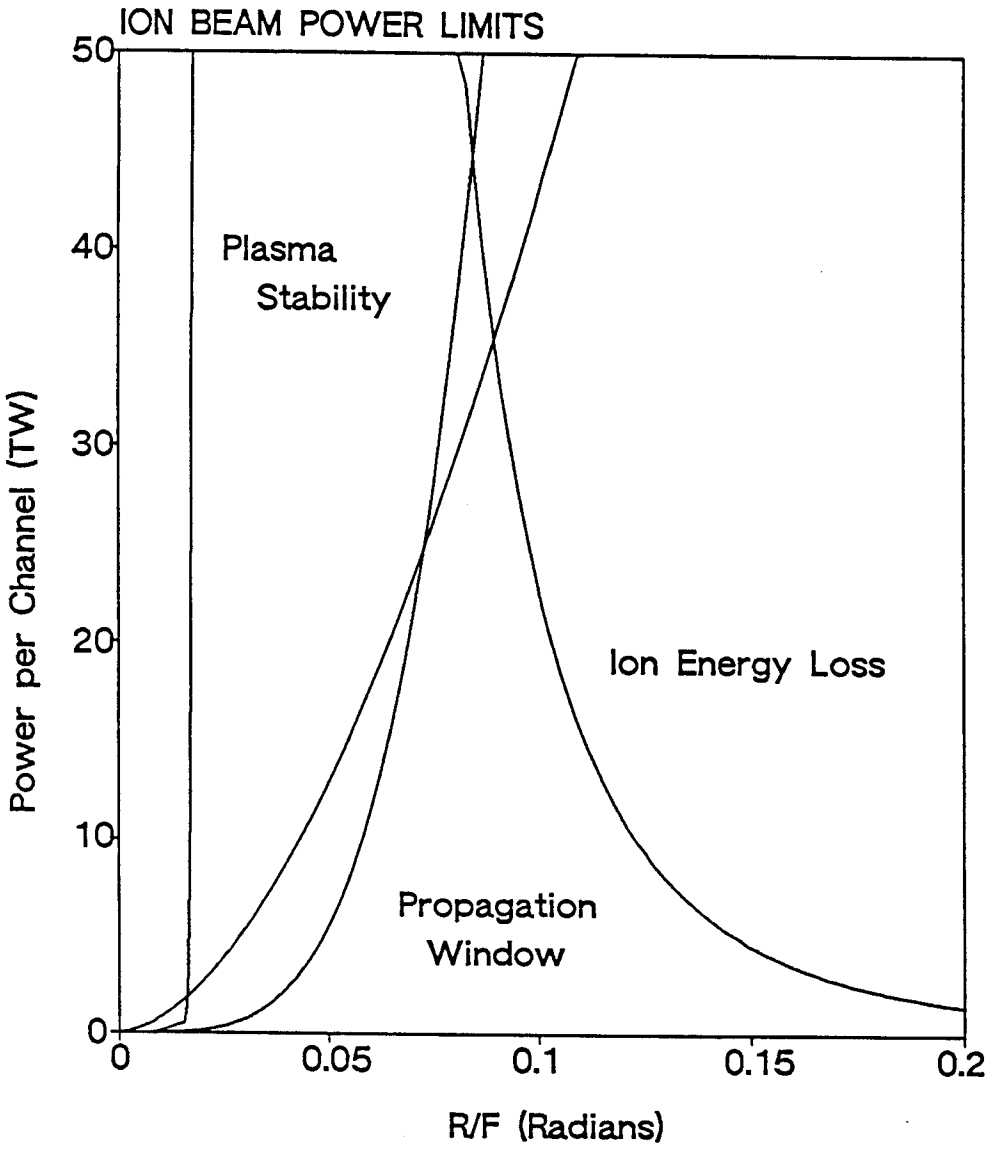

Fig. 4.17. Window of propagation in ion injection angle versus ion power space for 30 MeV lithium ions in the "slow" discharge channel.

Table 4.1. Ion Beam Confinement

Ion Species	Focal Spot Radius (cm)	Maximum Divergence Angle (radians)	Fraction of Ions Confined
30 MeV Li	0.3	0.075	19/25
30 MeV Li	0.15	0.075	21/25
30 MeV Li	0.15	0.1	14/25
30 MeV Li	0.3	0.1	21/25
50 MeV B	0.15	0.035	25/25

below all of the curves. The curves on the left are due to the constraints imposed by electrostatic, beam current filamentation, and channel current filamentation instabilities, while the curve on the right is due to beam ion energy loss. This energy loss ion power limit requires that the ions lose no more than 25% of their energy during transit down a 4 meter long channel and assumes that the channel is created in a deuterium gas. The results differ from that for a N_2 gas because N_2 radiates much more strongly and will not get as hot and will have a lower outward velocity leading to smaller v x B forces. Figure 4.17 shows that one should be able to propagate 1 MA of 30 MeV lithium ions at an injection angle of 0.1 radians. From our ZPINCH runs, we have estimated ion energy losses for a 1.25 MA beam to be about 6 MeV per ion or 20%.[6] All of these results seem to indicate that the TDF channel design allows 1.25 MA of 30 MeV lithium ions to be propagated per channel.

4.2 Forces Between Channels

Plasma channels each carry up to 50 kA of discharge current and 2.5 MA of ion beam current which could conceivably couple with similar currents in neighboring channels, causing mutual forces between channels. The discharge current occurs over the period of time up to the time of ion injection at 5.1 μs while the ion current is limited to a pulse 15 to 30 ns long. The ion current is neutralized to a large degree so we will not consider the forces due to it. The component of the force in the plane of the channels on a channel due to an adjacent channel can be expressed as

$$F = -\frac{2I}{c^2}\int_0^{r_c} dr' \int_0^{2\pi} d\theta \frac{r'\, j(r',\theta)\cos(\phi)}{\sqrt{R_c^2 + (r')^2 - 2R_c r' \cos\theta}} \qquad (4.1)$$

where $j(r,\theta)$ is the current density, R_c is the distance between the centers of the channels, r_c is the channel radius, c is the speed of light and I is the total current in the channel supplying the force. ϕ is the angle, seen from the center of the channel supplying the force, between the position of the current element and the center of the channel experiencing the force. At this point we assume that $j(r,\theta)$ is constant at a value of j out to r_c, beyond which is vanishes. For the TDF geometry, the average value for R_c is 117 cm and r_c is 1 cm. Doing the integrals in Eq. (4.1), we obtain

$$F = -6.23 \times 10^{-23}\, jI \qquad (4.2)$$

where the currents have units of statamps and the force is in dynes. Considering the discharge current part of the force, I is 50 kA and j is 16 kA/cm^2, so the force on the channel is -4.48×10^5 dynes/cm, where the minus

sign implies that the force tends to pull the channels together. If this force is turned on for 5 μs and if the mass of the channel is 7×10^{-5} g/cm, the channel will move 0.08 cm. This is certainly small compared to the radius of the channel and the current and current density are always below the values used here, as one can see in Fig. 4.4. Also, this is the displacement if there is no channel on the other side to balance the force. However, at the target end of the channels, R_c is only 2 cm and we must reconsider.

At the target end of the channels, the force for R_c of 2 cm and an r_c of 1 cm is

$$F = -4.36 \times 10^{-21} \, jI \tag{4.3}$$

where the units are the same as in Eq. (4.2). If we use the time dependent currents in Fig. 4.4, we get a displacement of 1.4 cm at 5 μs balanced after the start of the discharge, which is significant. However, if all 8 channels are formed this displacement will not occur because the forces will be balanced by those from the channel on the other side from the one considered here. What this does mean is that, if one of the channels is not formed for some reason, the other channels may not direct their beams to the target.

4.3 Channels in an Externally Applied Magnetic Field

Electrical breakdown from the plasma channels to the target chamber wall could prevent the formation of the plasma channels. An externally applied magnetic field can significantly increase the effective breakdown voltage between the channel and the wall.[7] The magnetic field could be supplied by solenoidal coils around the openings in the vessel wall. We have attempted to determine the effects of the external magnetic field on the plasma channels.

If the coils are truly solenoidal, the magnetic field in the plane of the wall will be uniform and axial. Since it is uniform, the addition to the pressure due to this field is also uniform and the gradient of the pressure in the radial direction is unchanged from the case where no external field is present. Therefore, the radial motion of the channel should be unchanged by the external field. This is borne out by one-dimensional computer simulations done with the Z-PINCH computer code, where a 5 tesla uniform field is applied to the base case channel described in Section 4.1 and no changes were seen in the channel behavior. The axial nature of the field means that the cross product of the radial fluid velocity and the applied magnetic field produces an azimuthal force that does not cause an energy loss for the beam ions.

In reality the coils are of finite length so that, as one moves away from the wall in an axial direction, the externally applied field is neither uniform nor axial. The field in these fringe regions would cause additional magnetic pressure gradients in the axial and possibly the radial directions. The strengths of the resulting forces would depend greatly on the coil design. The radial component of the applied magnetic field in these regions crossed into the axial velocity caused by these forces induces a relatively harmless azimuthal force on the beam ions.

References for Chapter 4

1. J.J. Watrous, G.A. Moses and R.R. Peterson, "Z-PINCH - A Multifrequency Radiative Transfer Magnetohydrodynamics Computer Code," University of Wisconsin Fusion Technology Institute Report UWFDM-584 (June 1985).

2. J.R. Freeman, L. Baker and D.L. Cook, "Plasma Channels for Intense-Light-Ion-Beam Reactors," Nucl. Fusion 22, 383 (1982).

3. J.M. Meek and J.D. Craggs, Electrical Breakdown of Gases, John Wiley & Sons (New York, 1978).

4. R.R. Peterson, "WINDOW - A Code to Compute Ion Power Constraints," Fusion Power Associates Report FPA-84-6 (December, 1984).

5. P.F. Ottinger, S.A. Goldstein and D. Mosher, "Constraints on Transportable Ion Beam Power," Naval Research Laboratory Memorandum Report 4948 (November, 1982).

6. R.R. Peterson, J.J. Watrous and G.A. Moses, "Numerical Simulation of Plasma Discharge Channels for Ion Beam Propagation in the Light Ion Target Development Facility," Bull. Amer. Phys. Soc. 30, 1504 (1985).

7. R.E. Olson, "Magnetic Insulation of Plasma Channels," Bull. Am. Phys. Soc. 29, 1389 (1984) 8R11.

5. Stratified Cavity Gas

An investigation was made to determine if the use of multiple layered cavity gases with different opacities could reduce the overpressure on the diodes or on diagnostic equipment placed below the target in a light ion beam chamber. Figure 5.1 illustrates the geometry under consideration. The target chamber was taken as a right circular cylinder. The cavity gases were then segregated into the two regions as illustrated; the top region would contain an optically transparent gas. The hypothesis is that once the radiation front of the fireball has reached the gas interface, "venting" of the radiation upward would then result in a nonspherical hydrodynamic expansion of the fireball in region B and thus reduce the pressure loading in the radial and downward axial directions.[1]

To test this theory, a 2-D Eulerian radiation fluid dynamics computer code was written.[2] The 2-T diffusion approximation[3] was used for modeling the radiation field. This assumption is valid in the lower cavity gas (region B) but is incorrect for the upper gas due to its low opacity. However, since we were not interested in modeling the behavior of the fireball in this region, the diffusion model was sufficient to obtain realistic boundary conditions for the lower gas region. The ramifications of this approximation will be discussed later. A tabular equation of state was used for the lower gas;[4] the upper gas was modeled as optically transparent.

5.1 Calculations

The present analysis used helium as the transparent gas (region A) and nitrogen as the "cavity" gas (region B). The calculations were done in cylindrical geometry using 5 cm square computational meshes. The radius was taken as 250 cm with a no-flow boundary. The axial "top" and "bottom" were modeled

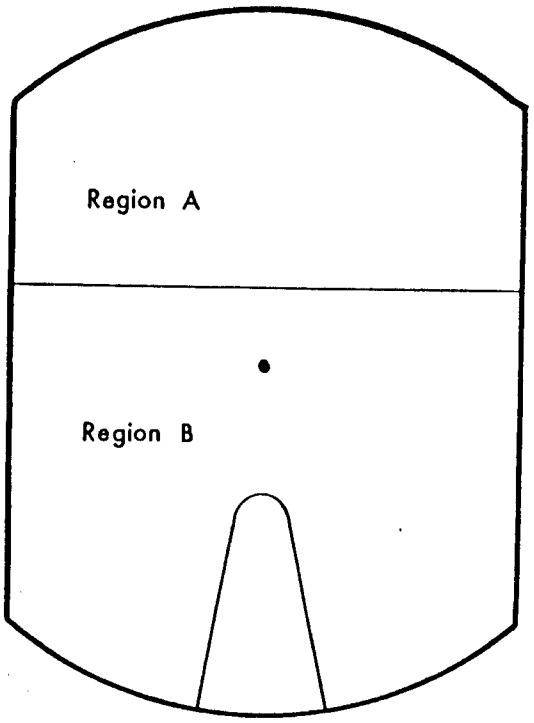

Fig. 5.1. TDF Cavity.

as free-flow boundaries. Typically the region below the target was 250 cm and the He region 200 cm. This was done to prevent any boundary contamination to affect the region of interest. Figure 5.2 shows the computational domain for the 100 cm calculation.

The initial number density was taken as 15 torr; the shot energy was 200 MJ (the standard TDF base case). The present code does not model ion deposition; therefore, MF-FIRE[5] was used to generate the initial ion temperature profile. Figure 5.3 shows this profile. Also indicated in the figure is the region where the shock is "launched": when the hydrodynamic speed is greater than the diffusion speed. The distance between the He region and the target was varied in this investigation; the three values are also shown in the figure (10, 40, and 100 cm). These were chosen to be inside the initial high energy deposition region (10 cm), just beyond it (40 cm), and prior to launching the shock (100 cm).

The present investigation was not concerned with detailed modeling of the nitrogen-helium interface. Thus, the computer code considered only a single species; the helium region was just modeled as nitrogen with negligible opacity (transparent gas). Essentially, the helium region served as a pseudo-boundary condition for the nitrogen region. Only the pressure loading in the nitrogen region (radial and downward axial) was of interest.

5.1.1 100 cm Distance Between Target and Gas Interface

The first calculation positioned the interface 100 cm above the target. This allowed sufficient time for the fireball to form before it encountered the He region. Figure 5.4 shows the development of the fireball. One can note that it has just begun to interact with the He at 17 microseconds. Prior to this time, it has essentially undergone a spherical expansion. At about 32

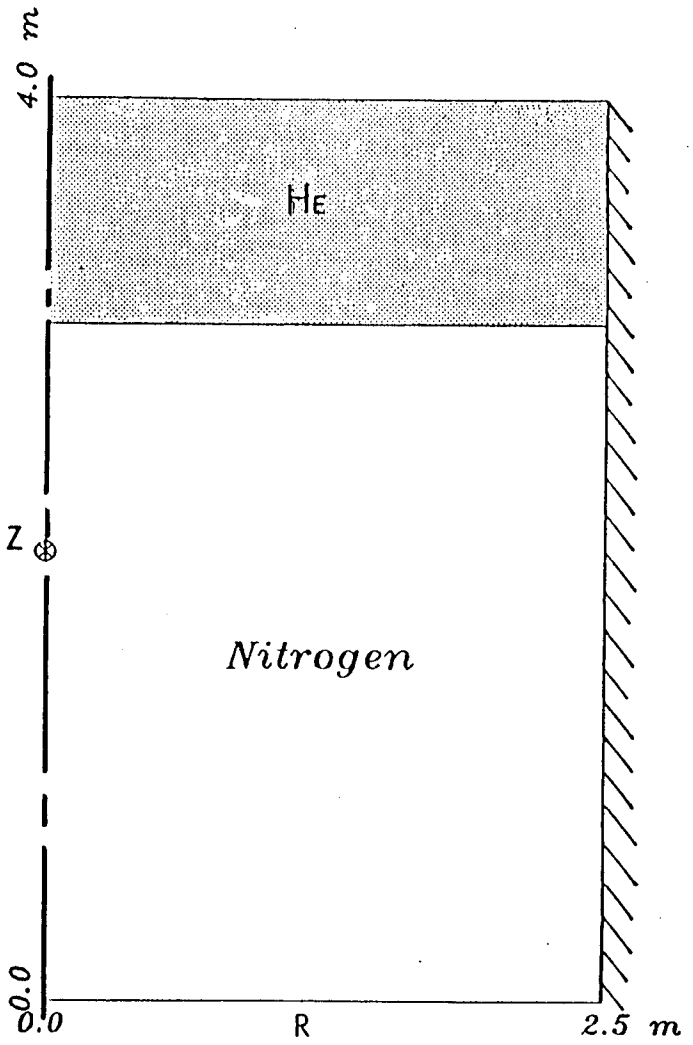

Fig. 5.2. Typical computational domain (100 cm case).

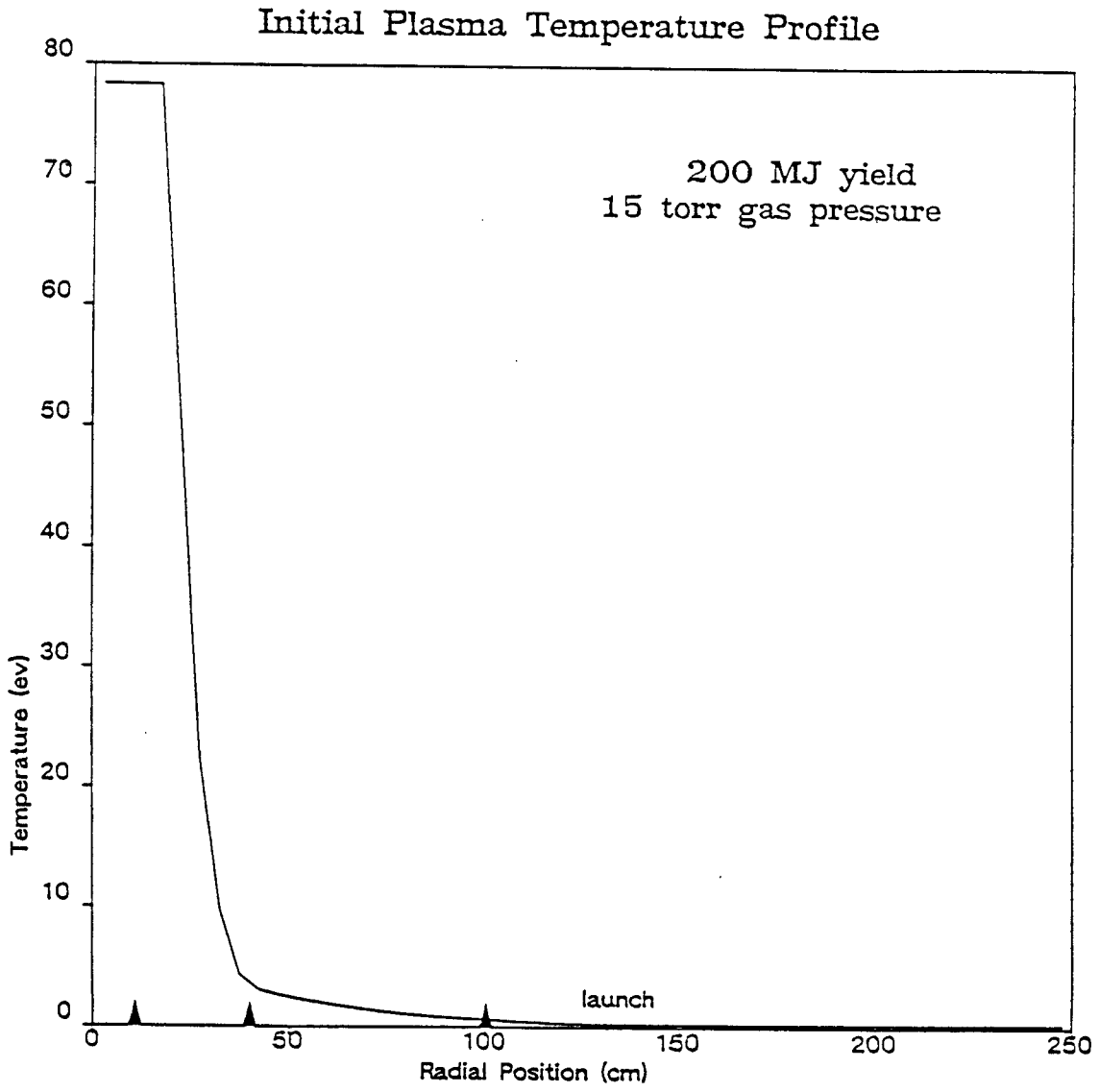

Fig. 5.3. Initial gas temperature profile.

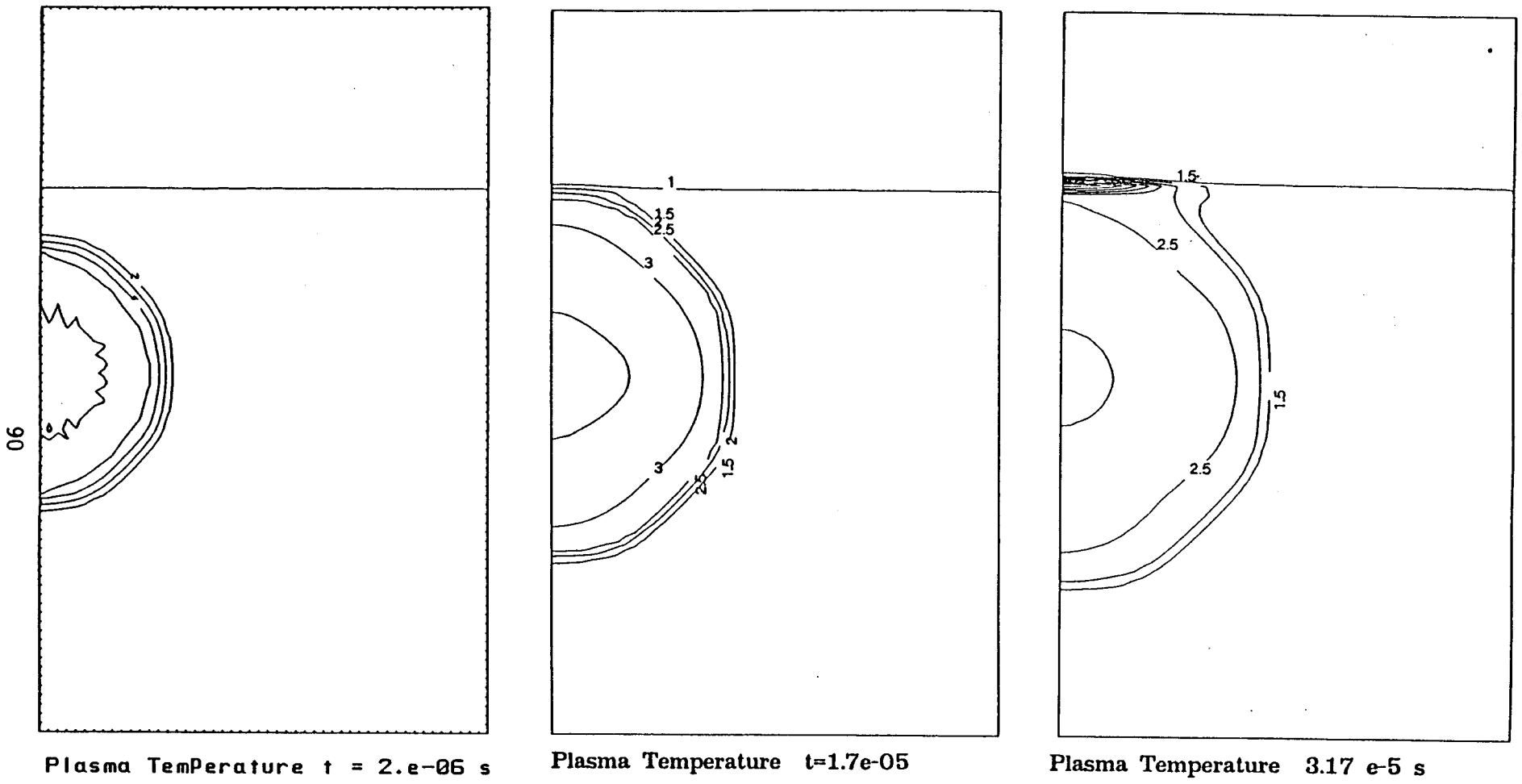

Fig. 5.4. Gas temperature contours for 100 cm case.

microseconds, the fireball has become nonspherical due to the change in gas properties at the interface; the effective gas conductivity in the He region is much smaller than the N_2 region due to the small He opacity. Therefore, on the time scales illustrated, the thermal wave does not propagate into the He region. Figure 5.5 illustrates an interesting effect of this opacity discontinuity: the gas temperature in the first He zone increases rapidly. This is due to the rapid compression of the He from the high stationary pressure gradient at the interface. The propagation of the thermal wave is dominated by the energy exchange between the radiation and the plasma fields; this exchange does not take place in the He region due to the pure transparent assumption. Finally, Fig. 5.6 illustrates the spatial distribution of the radiation temperature after the fireball has reached the interface. Here we can see that the radiation field has "burst" into the He gas and the fireball is venting energy "upward" in the cavity. One will note that the radiation temperature is approximately 2.5 eV at this point. This will be a crucial value in determining the effectiveness of this pressure reduction scheme.

Figure 5.7 shows the comparison between the vented 100 cm case and a single region nitrogen case. Essentially there are only minor differences. This is due to the relatively low radiation interface temperature when the fireball reaches the He. Since the radiation energy density is proportional to the fourth power of temperature, the actual energy flux being vented out of the fireball is comparatively small. Thus, the effect on the overpressure is negligible.

5.1.2 40 cm Distance Between Target and Gas Interface

In an effort to increase the interface radiation temperature when the fireball reaches the He region, the separation distance was reduced from 100

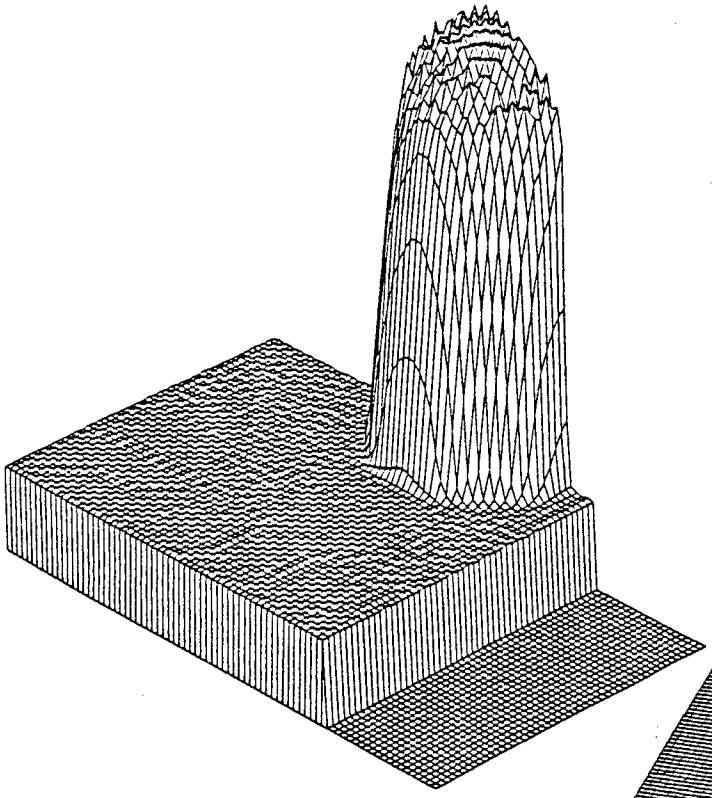

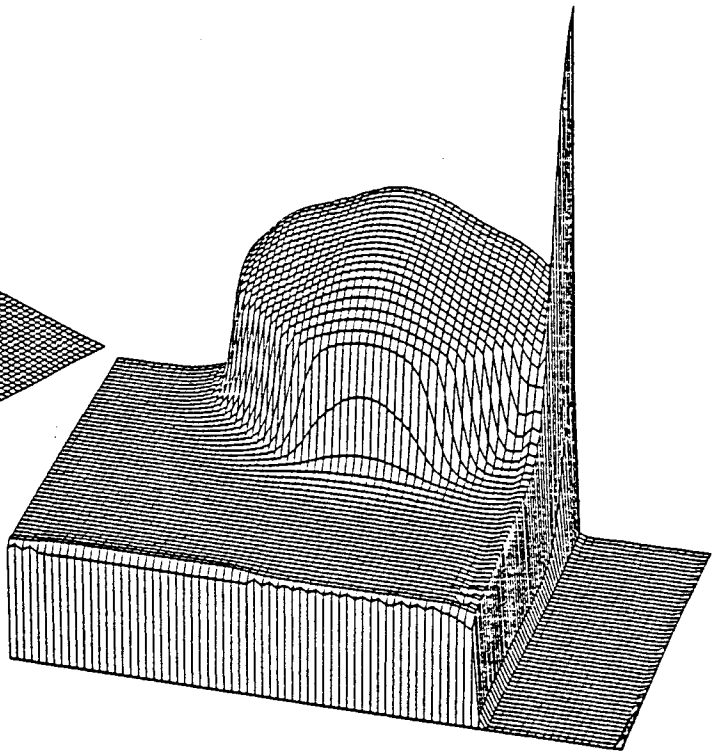

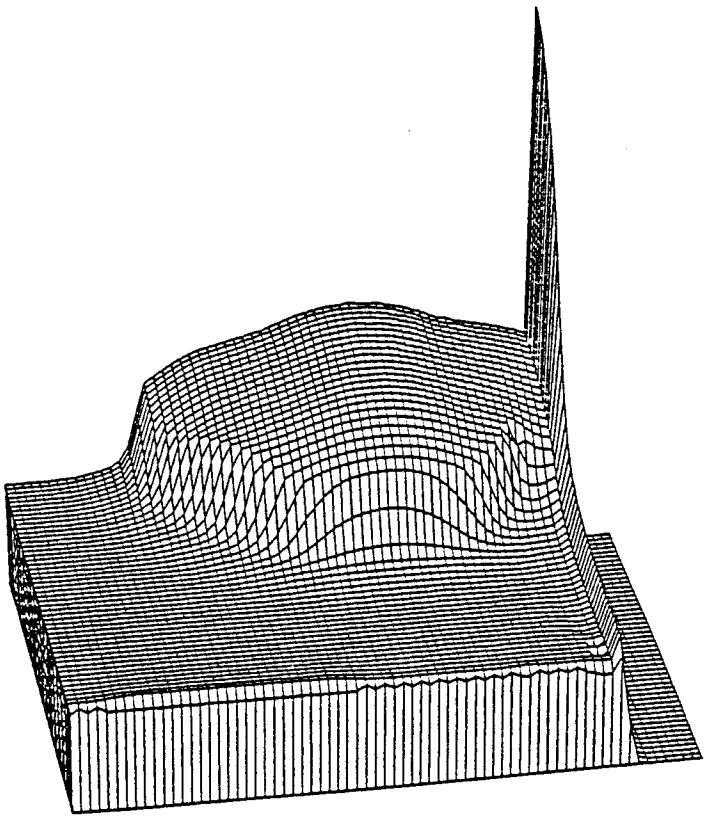

Fig. 5.5. Gas temperature for 100 cm case.

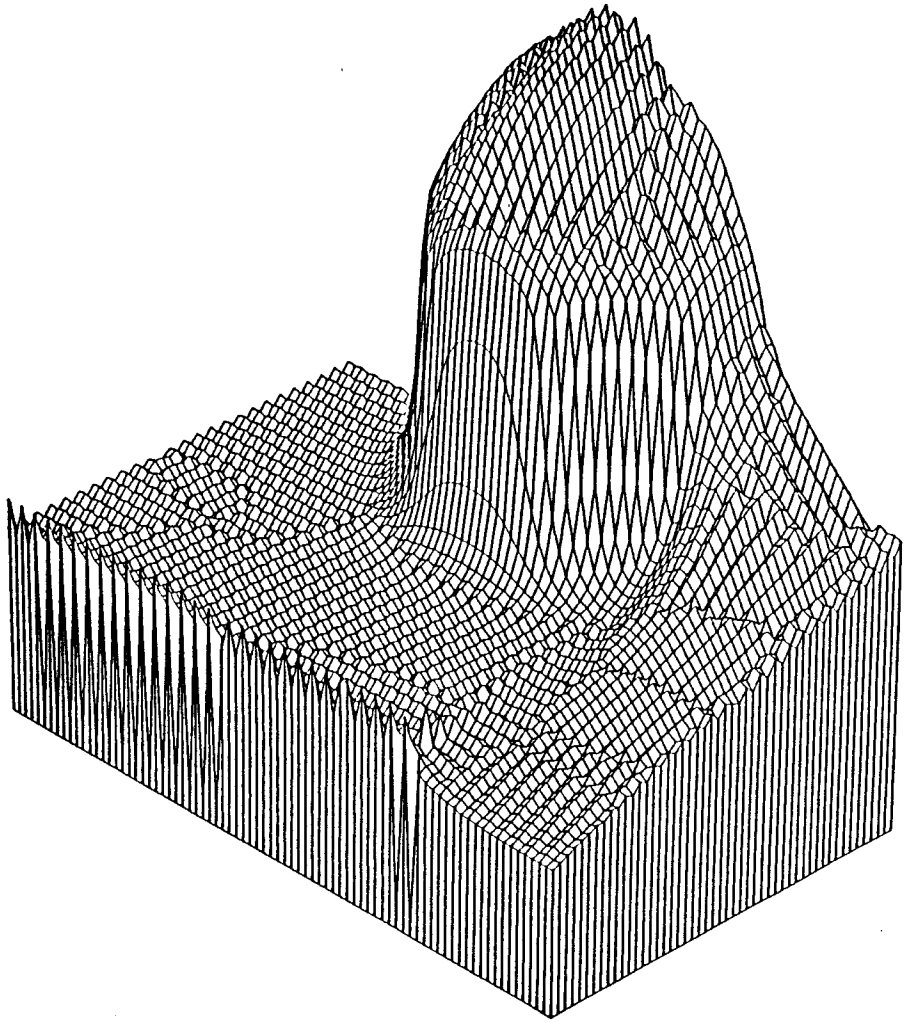

Radiation Temperature 2.16e-5 s

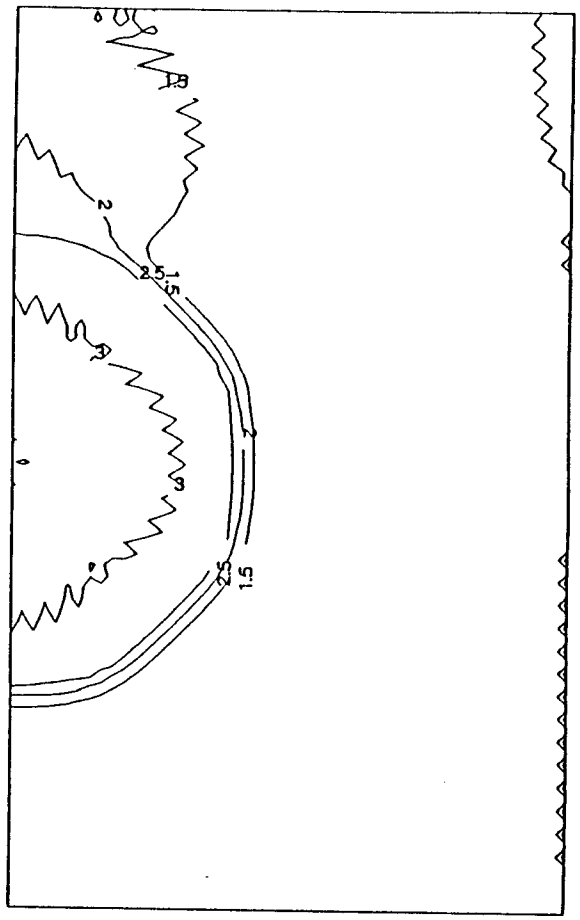

Radiation Temperature 2.16e-5 s

Fig. 5.6. Radiation temperature for 100 cm case.

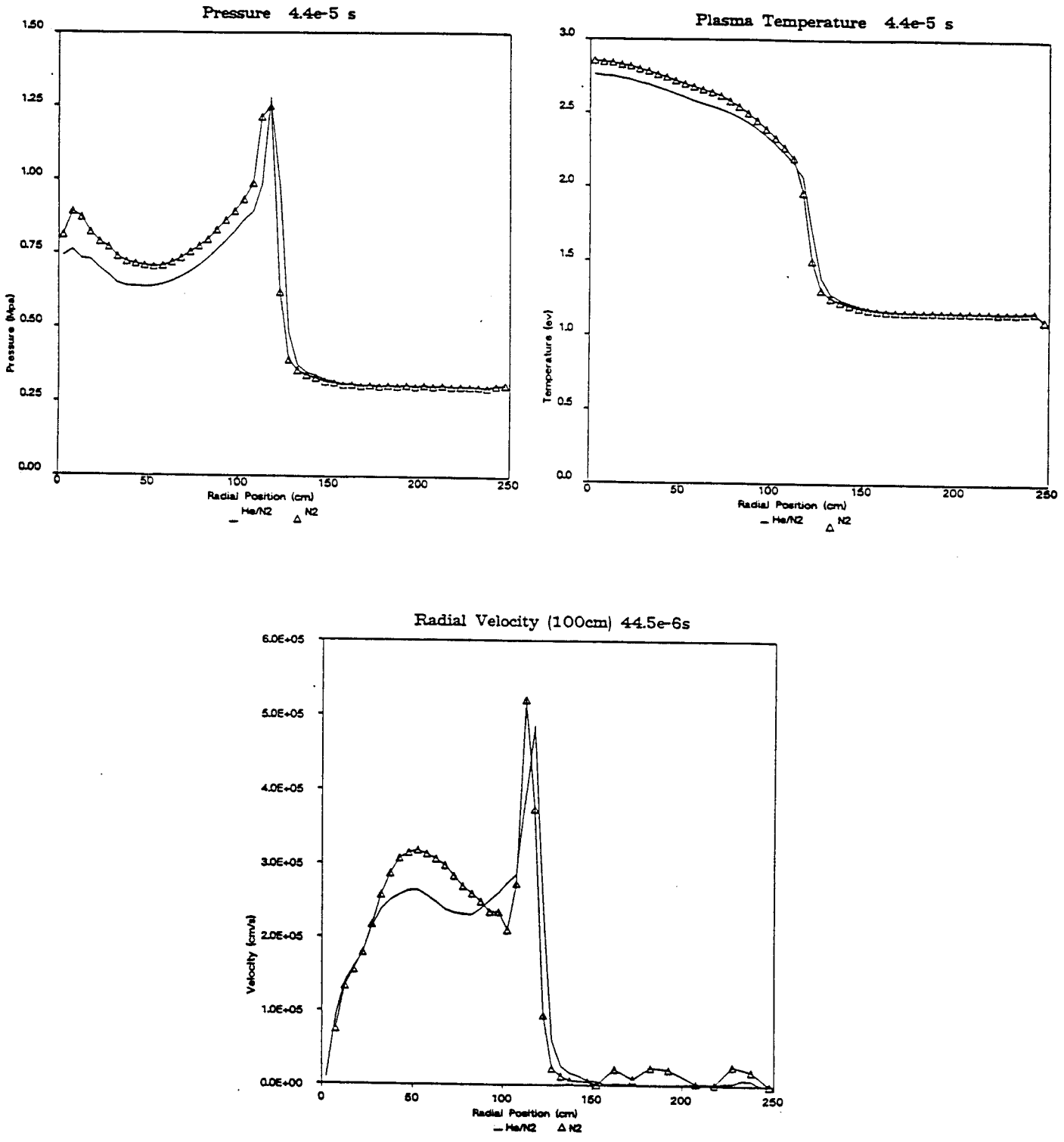

Fig. 5.7. Comparison of pressure, gas temperature and velocity between the vented 100 cm case and std. nitrogen calculation (radial direction from target).

cm to 40 cm. Figure 5.8 shows the plasma and radiation temperatures along the vertical axis for two early times. The target was at 200 cm and the interface located at 240 cm. Here we see that the interface radiation temperature is much higher than the 100 cm case when the fireball reaches the helium. A temperature of 16 eV results in approximately 1700 times the vented energy flux of the 100 cm case. The spatial behavior of the fireball was otherwise similar to the 100 cm case.

Figure 5.9 shows the comparison between the 40 cm vented case and the nitrogen case. One interesting point to be made is that the location of the fireball edge, using the location of the maximum velocity, is the same for both calculations. This will simplify the analysis in Section 5.2. One can easily see that the vented fireball contains less energy due to the reduced core plasma temperature and velocity. However, the peak velocities are similar because they are essentially determined from the pressure gradient at the edge of the fireball, which are about the same for both calculations. The pressure gradient, or equivalently the temperature gradient in the diffusion dominated region, is determined by the opacity variations of the cavity gas. Thus, one would expect the gradients to be similar irrespective of the venting process.

5.1.3 10 cm Distance Between Target and Gas Interface

The final calculation reduced the distance between the target and the He region to 10 cm. This was done to determine the maximum realistic effect of energy venting. Figure 5.10 shows the ion and radiation temperatures along the vertical axis during the initial stages of the fireball evolution. Here, one can easily see the interaction of the He region with the formation of the fireball. One interesting point is that the radiation temperature quickly

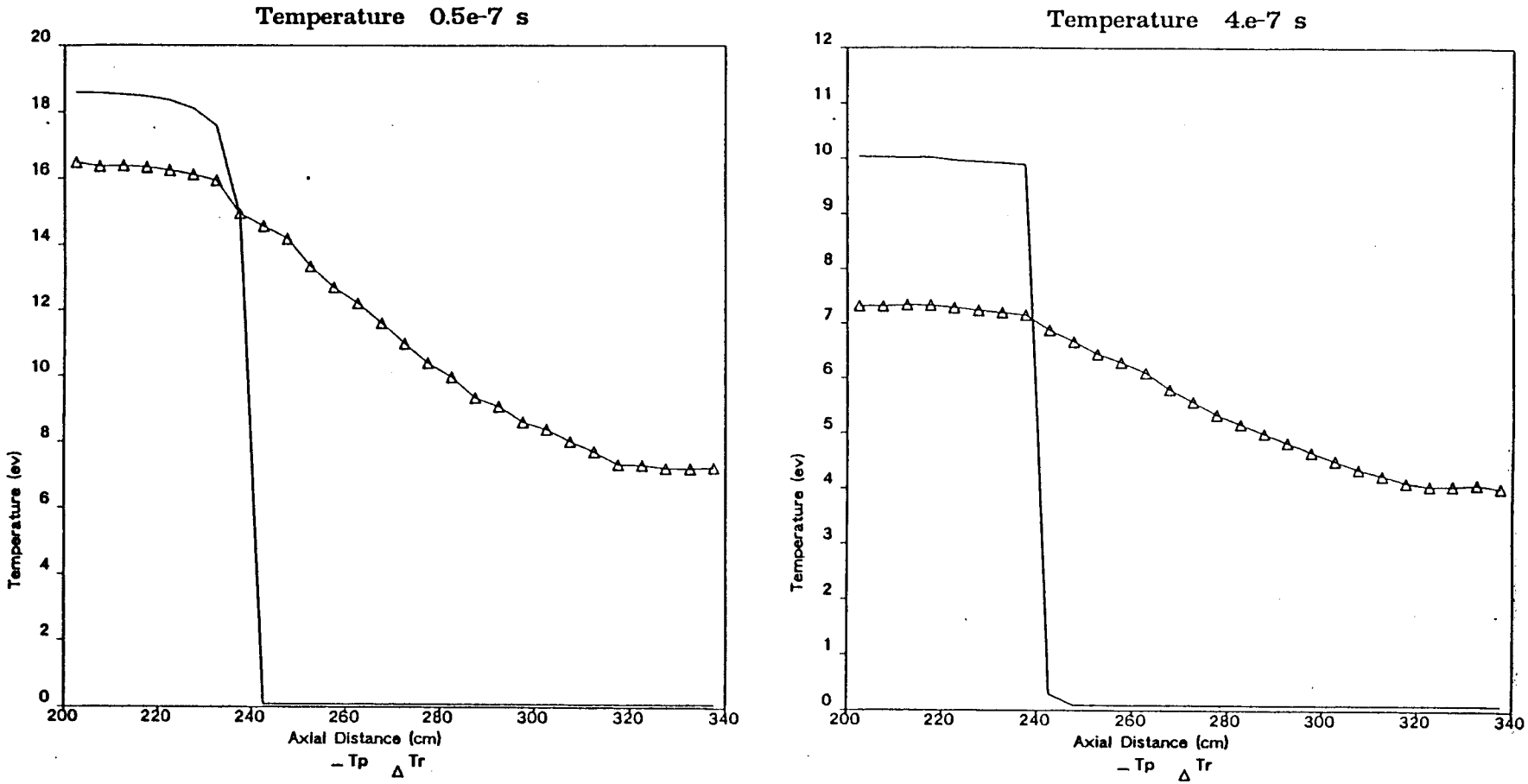

Fig. 5.8. Gas and radiation temperatures in axial direction (upward) for 40 cm case (target at 200 cm, interface at 240 cm).

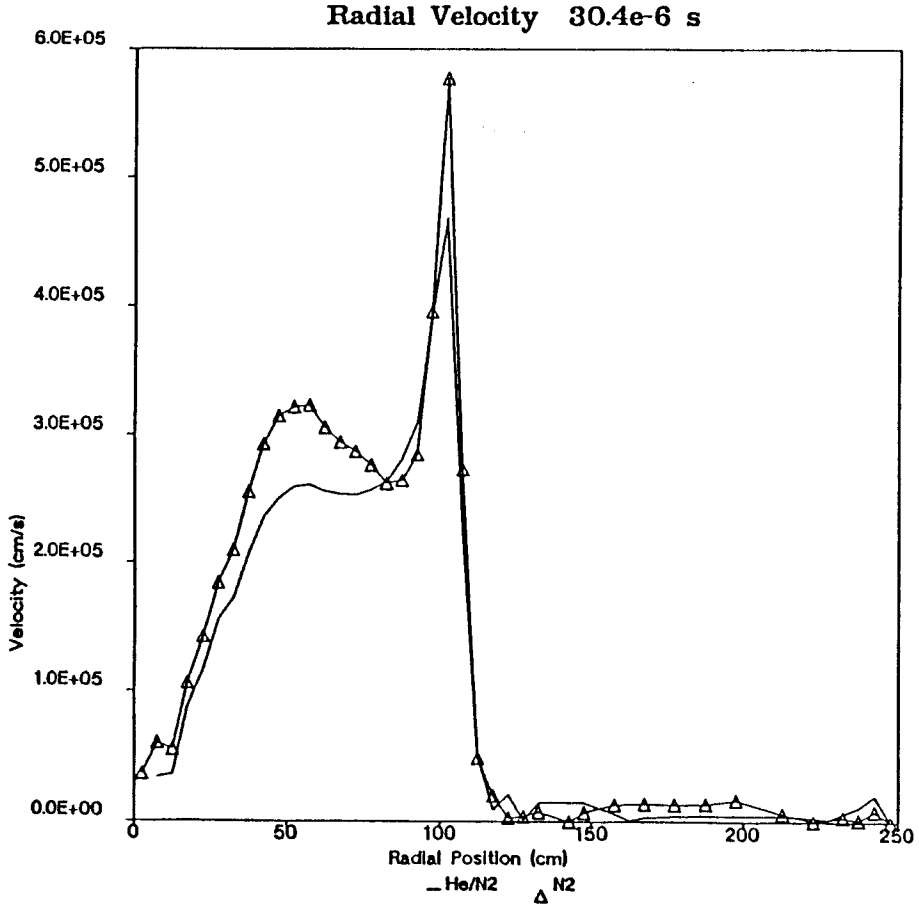

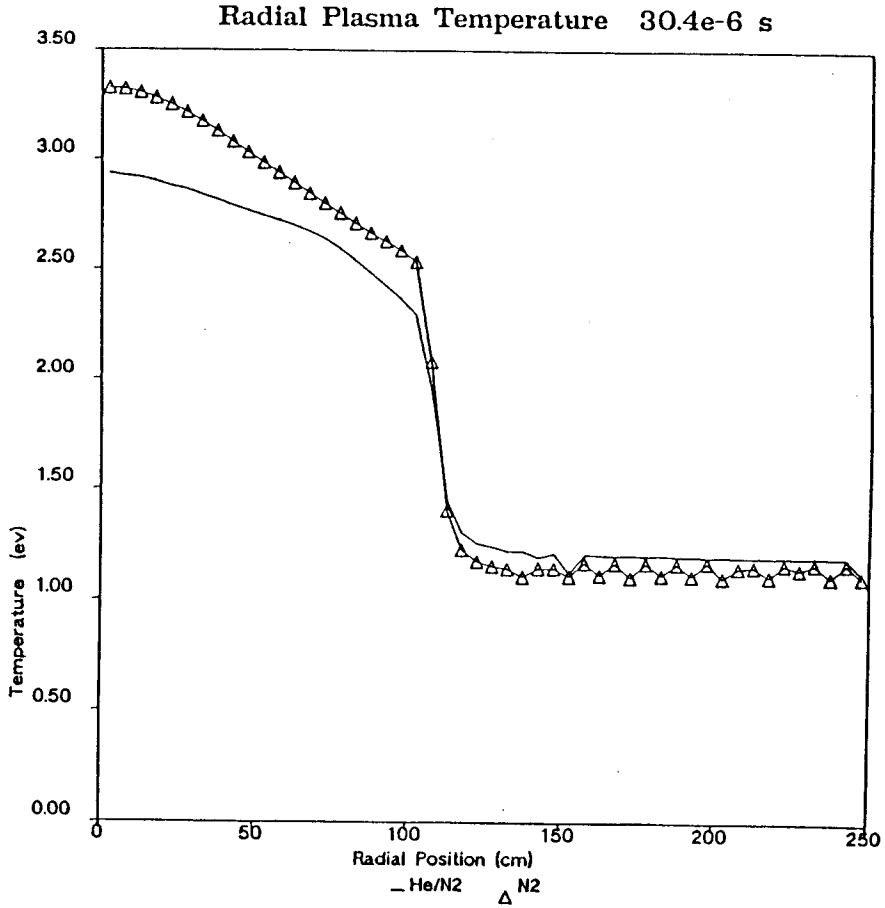

Fig. 5.9. Comparison of velocity and gas temperatures between vented 40 cm case and pure nitrogen (radial direction from target).

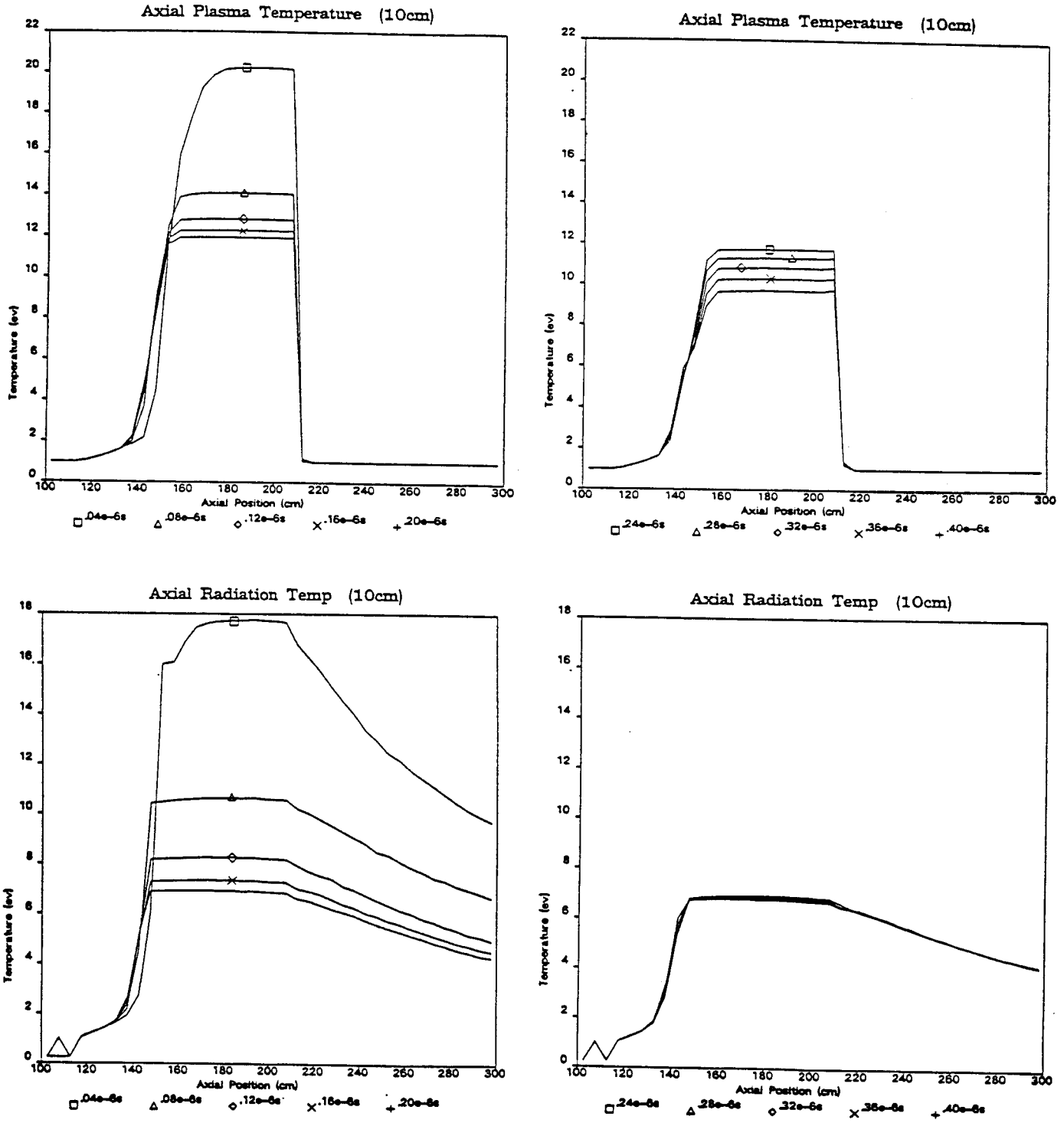

Fig. 5.10. Axial gas and radiation temperatures for 10 cm case (target located at 200 cm, interface at 210 cm).

reaches an equilibrium value of about 7 eV while the plasma temperature remains somewhat higher (12 eV); the energy loss by venting is balanced by the radiation emission from the plasma. These values are determined by the opacity differences in the parameter space of interest (temperatures and number densities). This equilibrium radiation temperature limits the vented energy loss. A different gas or fluid conditions might yield a more favorable equilibrium temperature.

As mentioned earlier, the diffusion approximation was used to model the radiation transport. This assumption is not valid in the He region, and in fact, "contaminates" the radial region at the target level. Figure 5.11 illustrates this effect. The contour plot shows the non-physical propagation of the radiation temperature in the He region. One would expect little radial diffusion as the radiation is transported upward from the "hole", the interface zone. However, the diffusion approximation with a scalar effective diffusivity causes the large radial propagation. The radiation then reenters the nitrogen region and interacts with the plasma, increasing its energy. This results in a diffuse region near the interface and is illustrated in the perspective plot of the plasma temperature. One can contrast the sharp gradient temperature along the downward axial direction to the gentle slope in the radial direction. This is entirely an artifact of the computational models used. For this reason, comparisons between the pure nitrogen calculation were done using the fluid values along the downward axial direction from the target, unaffected by this interface problem. Figure 5.12 shows this comparison. One can observe that although the peak stagnation pressure is essentially the same for both cases, the core values are noticeably reduced. The same trends are seen in the total energy density (internal + kinetic + pressure). How-

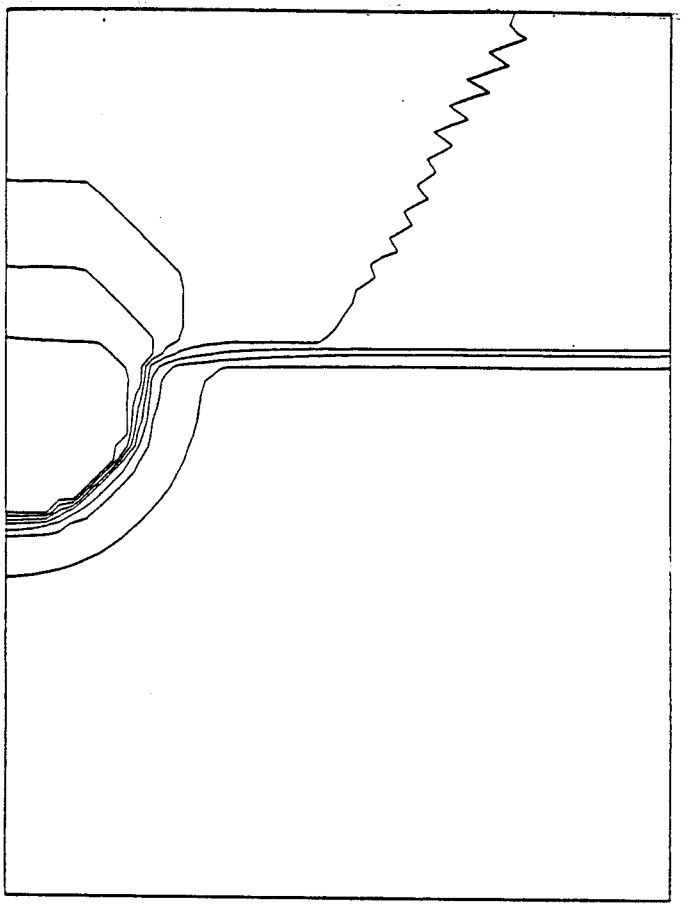

Radiation Temperature (10cm) 0.1e-6s

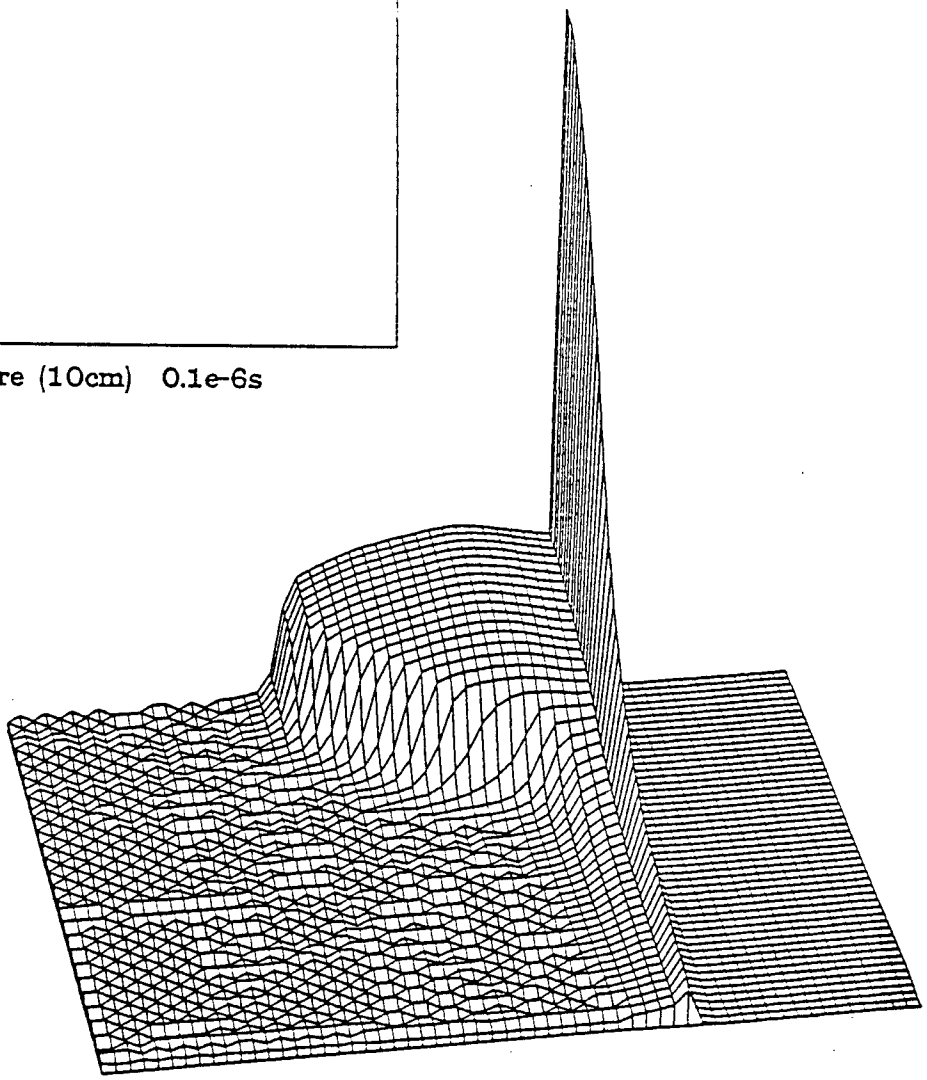

Plasma Temperature (10cm) 16.9e-5s

Fig. 5.11. Gas and radiation temperatures for 10 cm case.

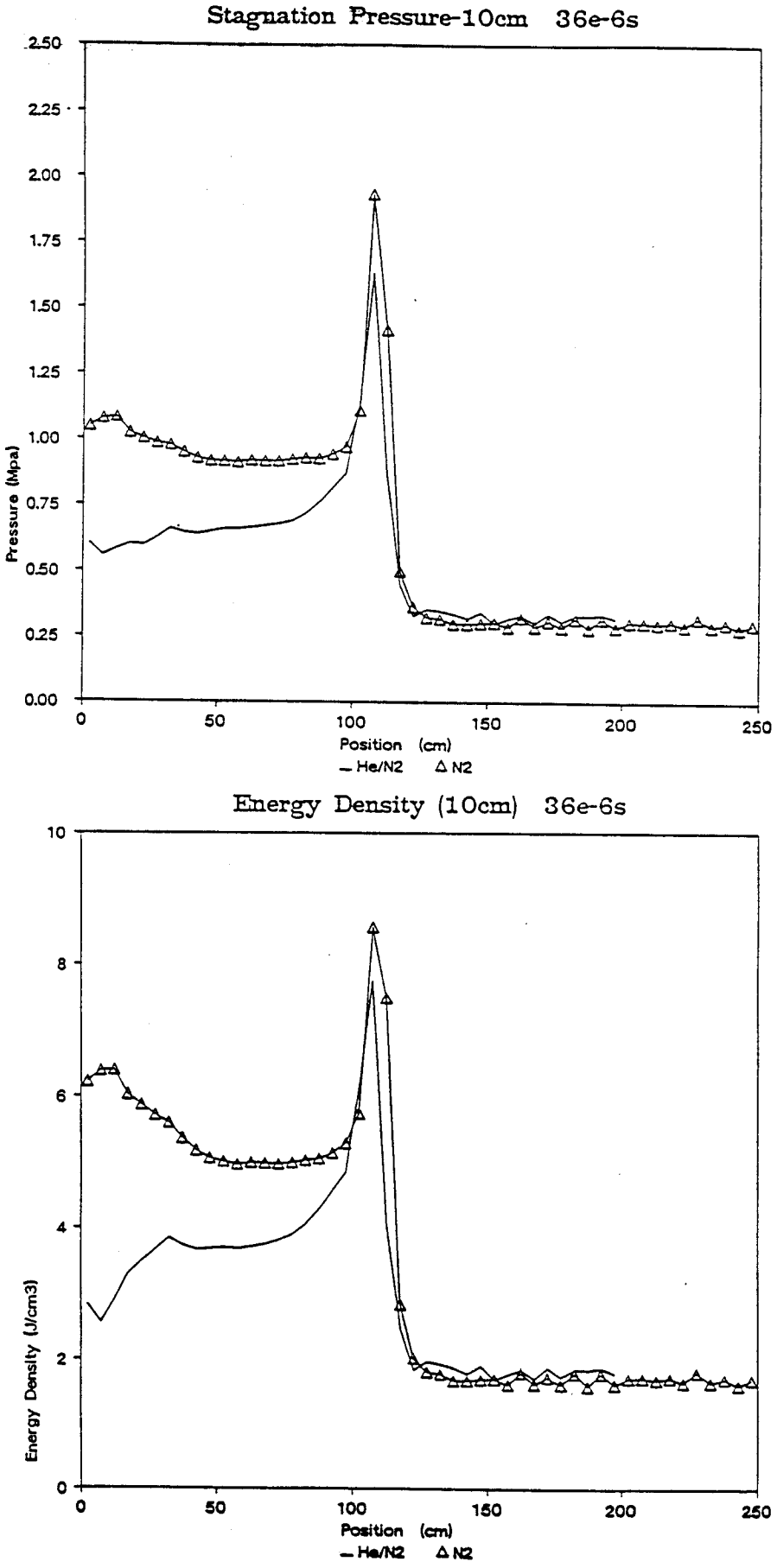

Fig. 5.12. Comparison between stagnation pressure and total energy density between the vented 10 cm case and pure nitrogen case (axial downward, target at 0 cm).

ever, the total fireball energy depends on the volume integral of this quantity and the majority of the volume of a sphere is near its outer radius. The differences are not as great as the plots would tend to indicate. This will be discussed in the following section.

5.2 Analysis

Figure 5.13 clearly shows the effects of the venting for the base conditions used. Here the energy in a pseudo-uniform fireball whose radial profile is the vented case (an equivalent target yield) is scaled to a single region expansion. One can see that the 100 cm separation distance resulted in only a minimal effect while the 10 cm case achieves a reduction of approximately 20%. Since the radial position of the fireball is similar for both the vented and non-vented cases, it is easy to determine the overpressure reduction one would expect. Strong shock theory[6] states that the pressure impulse is proportional to the total energy and inversely proportional to the radius cubed. However, for the same radius, the impulse ratio between the vented and non-vented cases simply reduces to the ratio of the fireball energies. Thus, Fig. 5.13 gives the impulse reduction directly.

Figure 5.14 shows the temporal interface radiation temperature behavior for the three cases; it is equivalently the vented energy flux. This figure helps to interpret the results of the preceding figure. We can see that the temperatures for the 10 and 40 cm cases are essentially the same. Thus the differences between the energy ratios is due to the increased vent area for the 10 cm case. The 100 cm interface was too far from the target and thus its vented energy density was too low to significantly affect the fireball.

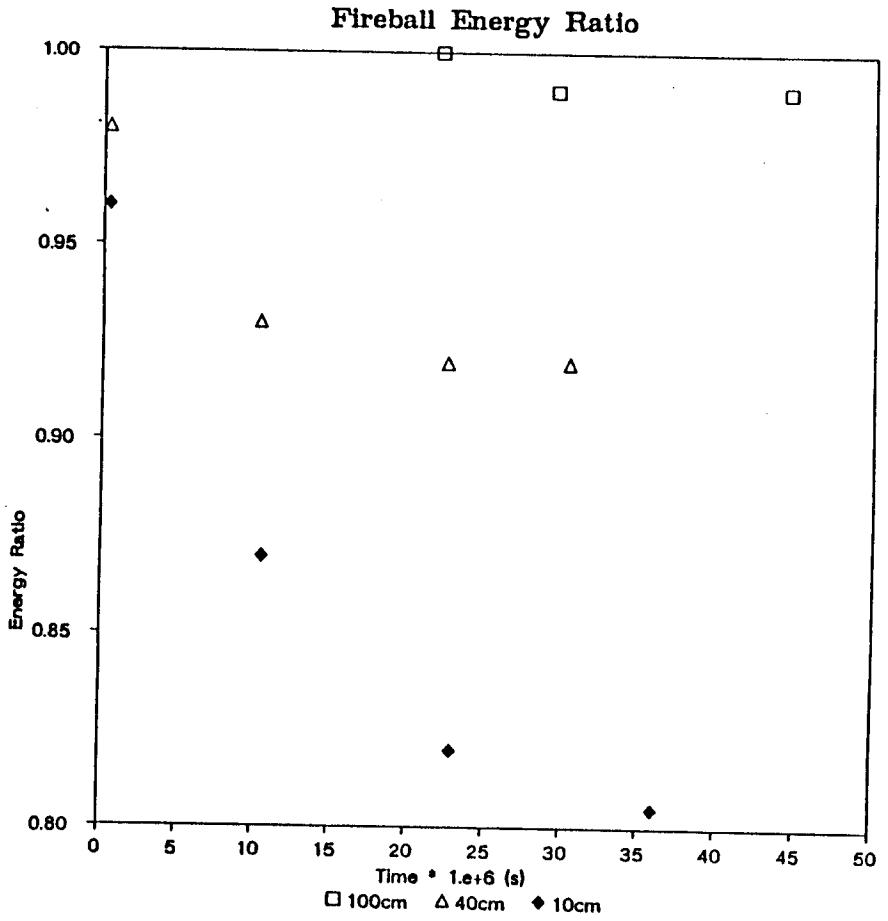

Fig. 5.13. Ratio of fireball total energy for vented case to pure nitrogen case.

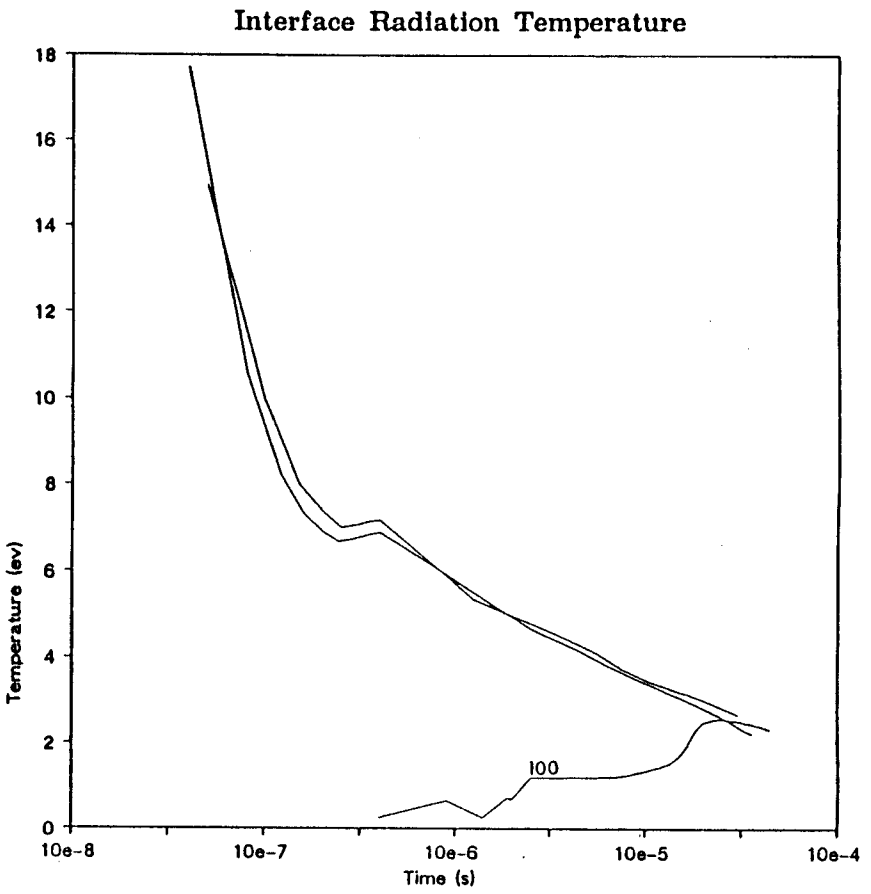

Fig. 5.14. Radiation temperature at the He-N_2 interface along z-axis for 10, 40, and 100 cm cases.

5.3 Conclusions and Recommendations

For the TDF base case of a 200 MJ shot and cavity gas pressure of 15 torr, only the 10 cm separation distance resulted in a practical pressure impulse reduction. Its effect was limited by the rapid decrease in the interface radiation temperature to an equilibrium value of about 7 eV. The timing of the fireball front remained about the same for both the vented and non-vented cases.

Two free parameters exist which might be varied to increase the venting effect: the shot energy and the cavity gas pressure. Changing the cavity gas pressure would be an attempt to increase the equilibrium radiation temperature and thus increase the vented energy. Increasing the shot energy would increase the duration which energy would be vented before the equilibrium value would be reached. In the present situation for TDF, this would imply performing calculations at a target yield of 800 MJ.

References for Chapter 5

1. G.A. Moses, R. Spencer, "Compact-Electron-Beam or Light-Ion-Beam Fusion Reactor Cavity Design Using Nonspherical Blast Waves," Nucl. Fusion 19, 1386-1388 (1979).

2. T.J. Bartel, R.R. Peterson, G.A. Moses, "Computer Simulation of a Light Ion Target Explosion in a Stratified Cavity Gas," to be published as a University of Wisconsin Fusion Technology Institute Report.

3. G.C. Pomraning, "Radiation Hydrodynamics," Los Alamos National Laboratory Report LA-UR-82-2625.

4. R.R. Peterson and G.A. Moses, "MIXERG - An Equation of State and Opacity Computer Code," Computer Physics Comm. 28, 405 (1983); also, University of Wisconsin Fusion Technology Institute Report UWFDM-464 (March 1982).

5. G.A. Moses, T.J. McCarville, R.R. Peterson, "Documentation for MF-FIRE, A Multifrequency Radiative Transfer Version of FIRE," Computer Phys. Comm. 36, 249 (1985); also, University of Wisconsin Fusion Technology Institute Report UWFDM-458 (March 1982).

6. H.A. Bethe et al., "Blast Wave," Los Alamos National Laboratory LA-2000 (August 1947).

6. Summary of Results

The TDF reaction chamber has been designed to match the fatigue lifetime for the 15,000 target shots at 200 MJ specified in the requirements for the facility. Up to 200 additional very high yield (800 MJ) shots can be accommodated if a steel chamber is used. These 800 MJ shots cannot be performed if an aluminum chamber is used. This analysis was performed using the conservative ASME Pressure Vessel Code guidelines.

The TDF reaction chamber suffers neutron activation to a degree that hands on maintenance is not possible shortly after shutdown, within one month, for either steel or aluminum chambers. The steel chamber gives a much higher radiation dose than aluminum. There appears to be a design solution to mitigate the activation problem in the aluminum chamber to tolerable levels. This involves placing a graphite moderating material inside the target chamber to soften the neutron spectrum. These calculations have not been done for a steel chamber but indications are that the reduced activation will still be too high for hands on maintenance.

Hence, there is a tradeoff between using a steel chamber for very high yield shots and using an aluminum chamber for low activation. This tradeoff will be determined by the degree of hands on maintenance that is necessary for successful operation of the facility.

Work will continue on the activation problem because this appears to be the major technical problem with the nuclear island response to the target explosion. The mechanical and thermal response of the target chamber is manageable through a number of different design options that have been investigated over the past two years.

Work on strain-based low cycle fatigue during the past year has parameterized the fatigue life as a function of the impulse experienced by the first wall, the thickness of the wall and the radius of the wall. These calculations allow us to investigate small chamber radii or larger yields. Earlier microfireball calculations showed that the impulse on the wall did not scale in a consistent manner with chamber radius and target yield. This warrants further investigation, since it could imply that a significantly smaller target chamber could be used. A smaller chamber implies less activation and possibly a frequent replacement scheme. It also implies shorter channels for ion propagation.

Calculations have shown that as much as 20% of the ion energy is lost while propagating in 4 meter long channels. Hence 30 MeV ions at the diode reach the target with average energies of 24 MeV. This has an effect on target design. Shorter channels have a lower inductance and can be formed more quickly than longer channels. This could affect the "design" of the optimum channel characteristics for efficient ion propagation. These studies are continuing.

Acknowledgment

Support for this work has been provided by the U.S. Department of Energy.